TWO-DIMENSIONAL CRYSTALLIZATION FROM MUTICOMPONENT SOLUTIONS

by

Seokhoon Ahn

A dissertation submitted in partial fulfillment
of the requirements for the degree of
Doctor of Philosophy
(Chemistry)
in The University of Michigan
2011

Doctoral Committee:

    Professor Adam J. Matzger, Chair
    Professor Mark M. Banaszak Holl
    Professor Zhan Chen
    Professor Rachel S. Goldman

ACKNOWLEDGMENTS

TABLE OF CONTENTS

LIST OF FIGURES

Figure

LIST OF TABLES

CHAPTER 1

Introduction

1.1 STM investigation of physisorbed monolayers

Understanding and controlling molecular assembly is the ultimate goal of chemists who working in the large, and growing, area of solid-state chemistry. From the drug delivery properties of pharmaceuticals to the performance of explosives and organic electronic materials, arrangements of molecules in the solid state profoundly influence properties leading to major scientific and practical impact. Despite the well understood importance of this problem, the community has all but given up the goal of widely applicable and robust structural prediction because the problem has too many degrees of freedom to be computationally tractable. An alternative to the tackling the problem of fully understanding self assembly in three dimensions has recently been offered: studying two-dimensional (2D) crystallization at the liquid/solid interface with the aid of scanning tunneling microscopy (STM), which can visualize atoms and molecules.[1]

The formation of physisorbed monolayers at the liquid/solid interface was discovered using calorimetry in 1969.[2] Since then, the structures of physisorbed monolayers of diverse compounds on graphite were visualized by STM and a number of molecules such as n-alkanes,[3,4] organic-metal complexes,[5,6] conjugated oligomers,[7-9] and polymers[10-12] have been intensively studied. Highly oriented pyrolytic graphite (HOPG) has been widely used most as a substrate even though gold, MoS_2, and other substrates have been also met with success.[4,13-18] The preference for graphite is that not only is it an atomically flat and electrically conductive material but also provides enthalpy reduction

through van der Waals interaction to overcome the entropic barrier to assembly.[19] Such physisorbed monolayers are well represented by n-alkanes as shown in Figure 1. In this case, the driving force of 2D crystallization is provided by van der Waals interactions among alkyl chains as well as between alkyl chains and HOPG. The molecules satisfy close packing which is a default behavior in 2D crystallization[20] and their orientation is well matched with the main symmetry axis of HOPG as shown in Figure 1.1.

The STM experiment to study a physisorbed monolayer formed at liquid/solid interfaces is depicted in Figure 1.2. The STM tip, which is an atomically sharp tip, protrudes into solution until the tip is located within tunneling distance. A bias is applied between the tip and the sample, and the tunneling current is monitored as the tip scans an area. During scanning of a physisorbed monolayer, slightly different tunneling currents are monitored depending on the type of functional groups or atoms due to different tunneling efficiency. Using these differences, the adsorbed molecules can be visualized even though the exact mechanism of tunneling through physisorbed molecules is still uncertain.[3,4,21-23]. For example, aromatic rings and carbon-carbon double and triple bonds are bright due to increased tunneling current in the STM images whereas carbonyls appear dark due to reduced tunneling current at a given height.[4] Another advantage of 2D crystallization using STM is that this approach offers submolecular resolution of not both periodic and nonperiodic packing as well as dynamic changes of adsorbed molecules where diffraction techniques are best suited to ordered and static systems. For example, the structural transition from a kinetically favored form to a thermodynamically favored form known as Ostwald's rule of stages in three-dimensional (3D) crystallization has been demonstrated in 2D crystallization by sequential STM images with atomic level detail.[24]

Physisorbed monolayers are often formed with periodic features. The structure of these 2D crystals is primarily determined by molecule-molecule, molecule-solvent, and molecule-substrate interactions.[25] Understanding theses interactions will lead to improved

design of molecular patterns on surface and may provide a means of modifying and functionalizing graphene surface.[26]

1.2 Two-dimensional crystal structural description

Physisorbed monolayers often show periodically ordered patterns which can be described as an infinitely repeating unit as shown in Figure 1.4. This unit cell can be described by two lengths (*a* and *b*) and an angle (*α*), and the number of molecules in the unit cell (*Z*). The unit cells possible in 2D crystallization reveal that the reduced dimensionality of assembly dramatically simplifies the system with only 17 plane groups possible in 2D crystallization (Figure 1.3) as compared to 230 space groups in 3D crystallization.[27] Each plane group can be characterized by symmetry elements such as translation, the two-, three-, four-, and six-fold rotations, mirror lines, and glide lines. After considering these symmetry elements in the unit cell, the asymmetric unit (*Z'*) can be determined from either sufficiently resolved STM images or computed models. For example, when amide amphiphiles are self-assembled with rhombic shaped voids, the unit cell is in the plane group of *p6* and twelve molecules exit in the unit cell (*Z*=12) as shown in Figure 1.4. The crystallographically inequivalent amide molecules in an asymmetry unit are three (*Z'*=3), indicated by a red oval in Figure 1.4. The frequency of occurance for various plane groups, the number of molecules in the asymmetric unit in 2D crystals formed at liquid/solid interfaces has been investigated by Matzger and coworkers.[20] Of the 876 physisorbed monolayers, a subset of 359 cases was carefully analyzed. The most common plane groups were *p2* (58%), *p1* (17%), *p2gg* (9.3%), and *pg* (4.4%). This investigation shows the strong agreement with the theory of close packing in two-dimensional crystals suggested by Kitaigorodskii fifty years ago.[28] The most common number of an asymmetric molecules was 1 (58.0%) and 1/2 (30.5%). However, the cases of *Z'* > 1 were not enough to study correlation with motifs in

3

noncovalent interactions employed in three dimensions. Therefore, the observation of cases of $Z' > 1$ provides valuable information to complete this relationship where it has been suggested in 2D and 3D crystallization that $Z' > 1$ is associated with strong noncovalent interactions.[29,30]

1.3 Crystallization from multicomponent solutions

Understanding phenomena of crystallization from muticomponent solutions is critical to control and design outcomes from such processes. These processes are conducted from the laboratory to industrial production due to the importance in purification and solid form engineering. Although general outcomes from such processes such as single component crystals, cocrystals, and solid solutions have been widely studied, kinetics and thermodynamics of crystallization from multicomponent solutions are still poorly understood. For example, the discovery of new metastable polymorphs in an attempted cocrystallization has been recently reported.[31-33] The mechanism of form production, however, is unclear making further developments difficult. Understanding this mechanism at the molecular level enables this phenomenon to be a new technique to isolate metastable polymorphs where different polymorphs exhibit different properties such as solubility, bioavailability, and stabilities. In addition, the limitation of characterization techniques such as X-ray diffraction makes studying nonperiodically ordered crystals difficult. An alternative to approach these issues can be studying 2D crystallization at the liquid/solid interface with the aid of STM, which can visualize the structure of both periodic and nonperiodic features in a time depedent fashion. For example, hexadecyl sulfide $((CH_3(CH_2)_{15})_2S)$ inserts randomly into the self-assembled monolayer of tritriacontane $(C_{33}H_{68})$ without disruption of the original monolayer structure.[34] This random mixing can be visualized due to different contrast of sulfur atom in STM images. Furthermore, because the reduced dimensionality dramatically simplifies

the system, the mechanistic insights of a new phenomenon in 3D crystallization can be provided at molecular level through studying the same phenomenon in 2D crystallization if possible.

1.4 General experimental procedures for imaging and computation

Scanning tunneling microscopy: A Nanoscope E STM (Digital Instruments) was used for all imaging. Highly oriented pyrolytic graphite (HOPG) (SPI-1 grade, Structure Probe Inc.) was used as a substrate for monolayer formation. A solution of the desired molecule was made and placed on freshly cleaved HOPG to obtain a self-assembled monolayer. The tips were made from Pt/Ir wire (20% Ir, 0.010 inch diameter, California Fine Wire) by mechanical cutting. STM imaging was performed using a quasi-constant height mode under ambient conditions and typical STM settings include 300 pA of current and 700-900 mV of bias voltage (sample positive). All images are unfiltered.

Computational modeling: The packing structures apparent from the metrics and symmetry of the STM images were modeled using Cerius^2 version 4.2 (Accelrys Inc.). Energy minimization was performed using a COMPASS forcefield. This method has been shown to yield reasonable energies for the relative stabilization of 3D polymorphic packing in molecular crystals.[35] Non-periodic assemblies from these models were overlaid on a fixed graphite slab and energy minimized to get the optimized packing structure on HOPG.

1.5 Two-dimensional crystallization from multicomponent solutions

This thesis details several investigations to understand behavior in 2D crystallization from an amide amphiphile solution and its mixture with other compounds.

In Chapter 2, the 2D crystal structures of amide amphiphiles bearing a long alkyl chain are examined. The strategy of using a low symmetry amphiphile to overcome symmetry limitations to construct a high symmetry pattern is discussed.

In Chapter 3, structural diversity in 2D crystals of an amide amphiphile has been demonstrated through controlling solvents and concentration. These results are interpreted in the context of kinetic and thermodynamic behavior.

In Chapter 4, additive-induced assemblies are investigated. The key factors affecting 2D crystallization from multicomponent solutions are discussed.

In Chapter 5, the formation process and characteristics of one-dimensional cocrystals as a new type of cocrystals are anatomized.

In Chapter 6, the conclusions and future directions of this research are discussed.

1.6 References

(1)   Binning, G.; Rohrer, H.; Gerber, C.; Weibel, E. *Phys. Rev. Lett.* **1982**, *49*, 57-61.

(2)   Everett, D. H.; Findenegg, G. H. *Nature* **1969**, *223*, 52-53.

(3)   Claypool, C. L.; Faglioni, F.; Goddard, W. A.; Gray, H. B.; Lewis, N. S.; Marcus, R. A. *J. Phys. Chem. B* **1997**, *101*, 5978-5995.

(4)   Giancarlo, L. C.; Flynn, G. W. *Annu. Rev. Phys. Chem.* **1998**, *49*, 297-336.

(5)   Schlickum, U.; Decker, R.; Klappenberger, F.; Zoppellaro, G.; Klyatskaya, S.; Ruben, M.; Silanes, I.; Arnau, A.; Kern, K.; Brune, H.; Barth, J. V. *Nano Lett.* **2007**, *7*, 3813-3817.

(6)   Ciesielski, A.; Lena, S.; Masiero, S.; Spada, G. P.; Samorí, P. *Angew. Chem., Int. Edit.* **2010**, *49*, 1963-1966.

(7)   Samorí, P.; Rabe, J. P. *J. Phys.: Condens. Matter* **2002**, *14*, 9955-9973.

(8)   Krömer, J.; Rios-Carreras, I.; Furhmann, G.; Musch, C.; Wunderlin, M.; Debaerdemacker, T.; Mena-Osteritz, E.; Bäuerle, P. *Angew. Chem., Int. Edit.* **2000**, *39*, 3481-3486.

(9)   Furukawa, S.; Uji-i, H.; Tahara, K.; Ichikawa, T.; Sonoda, M.; De Schryver, F. C.; Tobe, Y.; De Feyter, S. *J. Am. Chem. Soc.* **2006**, *128*, 3502-3503.

(10)   De Feyter, S.; Gesquière, A.; Abdel-Mottaleb, M. M.; Grim, P. C. M.; De Schryver, F. C.; Meiners, C.; Sieffert, M.; Valiyaveettil, S.; Müllen, K. *Acc. Chem. Res.* **2000**, *33*, 520-531.

(11)   Samorí, P.; Francke, V.; Müllen, K.; Rabe, J. P. *Chem.-Eur. J.* **1999**, *5*, 2312-2317.

(12)   Mena-Osteritz, E.; Meyer, A.; Langeveld-Voss, B. M. W.; Janssen, R. A. J.; Meijer, E. W.; Bäuerle, P. *Angew. Chem., Int. Edit.* **2000**, *39*, 2680-2684.

(13)   Kaneda, Y.; Stawasz, M. E.; Sampson, D. L.; Parkinson, B. A. *Langmuir* **2001**, *17*, 6185-6195.

(14)   Cincotti, S.; Rabe, J. P. *Appl. Phys. Lett.* **1993**, *62*, 3531-3533.

(15)   Uemura, S.; Samorí, P.; Kunitake, M.; Hirayama, C.; Rabe, J. P. *J. Mater. Chem.* **2002**, *12*, 3366-3367.

(16)   Yasuda, S.; Shigekawa, H. *Jpn. J. Appl. Phys., Part 1* **2003**, *42*, 4901-4904.

(17)   Xie, Z. X.; Xu, X.; Mao, B. W.; Tanaka, K. *Langmuir* **2002**, *18*, 3113-3116.

(18)   Perronet, K.; Charra, F. *Surf. Sci.* **2004**, *551*, 213-218.

(19)   Lei, S. B.; Tahara, K.; De Schryver, F. C.; Van der Auweraer, M.; Tobe, Y.; De Feyter, S. *Angew. Chem., Int. Ed.* **2008**, *47*, 2964-2968.

(20)   Plass, K. E.; Grzesiak, A. L.; Matzger, A. J. *Acc. Chem. Res.* **2007**, *40*, 287-293.

(21)   Marchenko, A.; Lukyanets, S.; Cousty, J. *Phys. Rev. B* **2002**, *65*, art. no.-045414.

(22)   Lee, H. S.; Iyengar, S.; Musselman, I. H. *Langmuir* **1998**, *14*, 7475-7483.

(23)   Faglioni, F.; Claypool, C. L.; Lewis, N. S.; Goddard, W. A. *J. Phys. Chem. B* **1997**, *101*, 5996-6020.

(24)   Kim, K.; Plass, K. E.; Matzger, A. J. *Langmuir* **2003**, *19*, 7149-7152.

(25)   Ahn, S.; Matzger, A. J. *J. Am. Chem. Soc.* **2010**, *132*, 11364-11371.

(26)   Wang, Q.; Hersam, M. C. *Nature Chem.* **2009**, *1*, 206-211.

(27)   Hahn, T., Ed. *International Tables for Crystallography: Volume A Space-Group Symmetry*; Fifth ed.; Kluwer Academic Publishers: Boston, 2002.

(28)   Kitaigorodskii, A. I. *Organic Chemical Crystallography*; Consultants Bureau: New York, **1959**

(29)   Plass, K. E.; Kim, K.; Matzger, A. J. *J. Am. Chem. Soc.* **2004**, *126*, 9042-9053.

(30)   Anderson, K. M.; Goeta, A. E.; Hancock, K. S. B.; Steed, J. W. *Chem. Commun.* **2006**, 2722-2722.

(31)   Rafilovich, M.; Bernstein, J. *J. Am. Chem. Soc.* **2006,** *128*, 12185-12191.

(32)   Lou, B. Y.; Bostroem, D.; Velaga, S. P. *Cryst. Growth Des.* **2009,** *9*, 1254-1257.

(33)   Day, G. M.; Trask, A. V.; Motherwell, W. D. S.; Jones, W. *Chem. Commun.* **2006**, 54-56.

(34)   Padowitz, D. F.; Messmore, B. W. *J. Phys. Chem. B* **2000**, *104*, 9943-9946.

(35)   Mitchell-Koch, K; Matzger, A. J. *J. Pharm. Sci.* **2008**, *97*, 2121-2129.
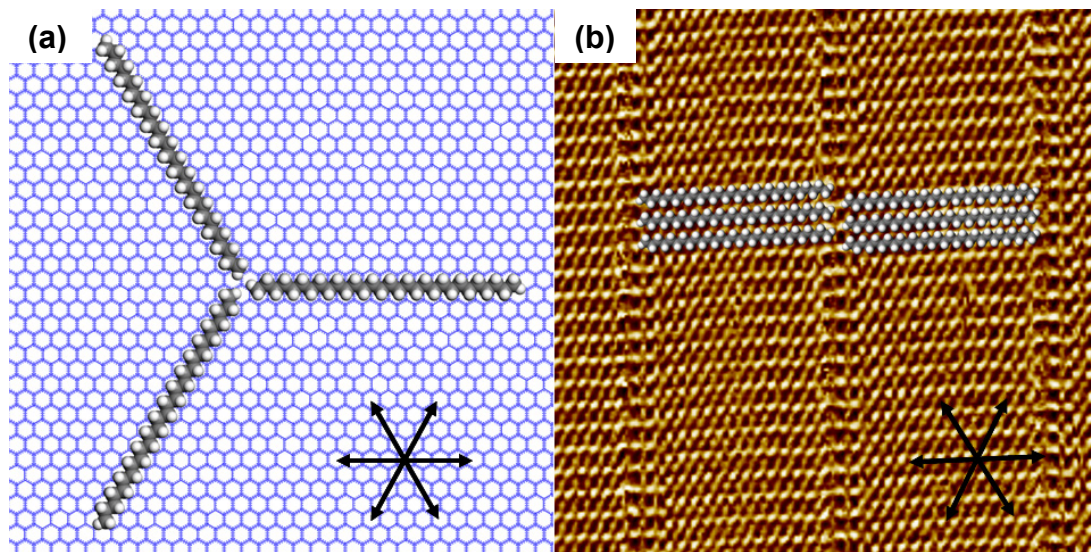
Figure 1.1. Two-dimensional crystal of triacontane at the 1-phenyloctane/graphite interface. (a) A schematic representation of the three symmetry-related orientations that the alkanes may adopt with respect to the main axes (black arrows) of graphite substrate. (b) STM image with small bright spots indicating the hydrogen atoms. The zigzag pattern of molecules in an all-trans conformation with the carbon backbone parallel to the surface is apparent. The alkyl chains are aligned along one of main axes of graphite under the monolayer.
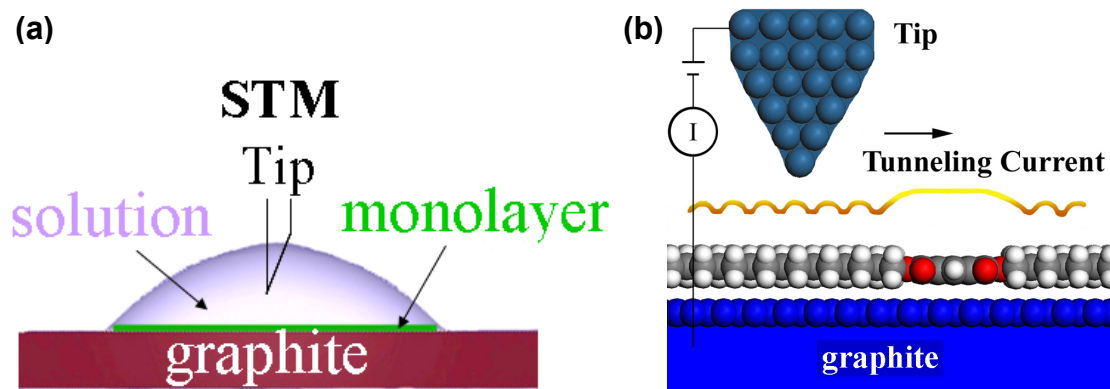
Figure 1.2. (a) Schematic illustration of the STM experiment and (b) illustration showing different contrast depending on atoms and functional groups when the atomically sharp tip rasters across the surface while the tunneling current is monitored.
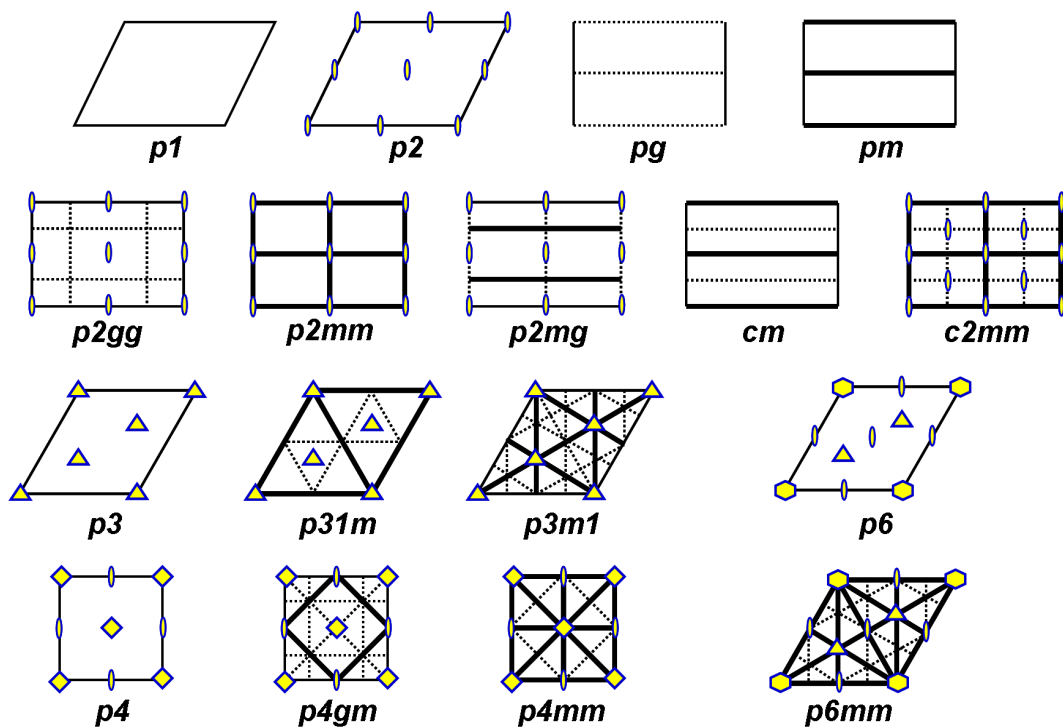
Figure 1.3. Schematic representations of the 17 plane groups. Yellow-colored diagrams are used to represent rotation symmetries and the bold and dot lines represent mirror and glide symmetry, respectively.
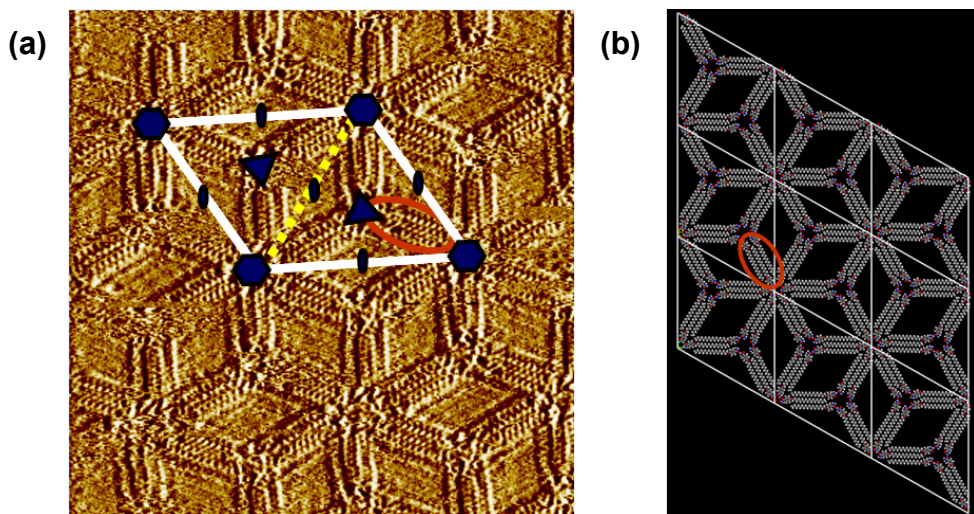
Figure 1.4. An example of the structural analysis carried out for 2D crystals. (a) An STM image of an amide amphiphile with a C_{18} alkyl chain. The unit cell is represented by white line and 2-, 3- and 6-fold rotations are represented by blue diagrams and mirror line is represented by yellow dots. The asymmetric unit (red oval) consists of three molecules. (b) A model of the packing with the unit cell (white outline) and asymmetry unit (red oval). The structure conforms to the plane group *p*6.

CHAPTER 2

Highly Symmetric 2D Rhombic Nanoporous Networks Arsing from Low Symmetry Amphiphiles

2.1 Introduction

Molecular self-assembly at the liquid/solid interface is now established to provide well-defined two dimensional (2D) crystals with nanostructured features in a size regime where traditional lithographic techniques fail.[1-3] These physisorbed molecular assemblies have been investigated with the aid of scanning tunneling microscopy (STM), offering structural and mechanistic insights.[4-7] Recently, an exotic class of 2D crystals has emerged with void spaces that constitute 2D porous networks.[8-11] Molecular inclusion of the sort long attainable in three-dimensions is now being realized on surfaces due to the ability of nanoporous monolayers to act as hosts for guest molecules.[12-14] Thus far, most 2D porous networks have been constructed by utilizing high molecular symmetry in concert with non-covalent intermolecular interactions such as hydrogen bonding and van der Waals (vdW) interactions.[9,15,16] For example, honeycomb networks are formed through extended hydrogen bonding of trimesic acid[15] or vdW interaction of a star-shaped stilbenoid compound.[16] The three-fold symmetric geometries of those molecules plays a critical role in forming the 3-fold rotation axes in the honeycomb network. In this chapter, an unusual example of the formation of a high symmetry nanoporous network from a low symmetry molecular building block. This symmetry generation in the 2D

crystal is accompanied by formation of molecular aggregates in the crystallographic asymmetric unit with three inequivalent molecules (Z'=3), in itself a rare occurrence.

During the course of investigations on the self assembly of aromatic primary amides bearing *para* substituents with long alkyl chains (Figure 2.1), the presence of more than one monolayer structure was observed. Although a close packed structure is the default behavior for physisorbed monolayers,[17] a 2D nanoporous network was unexpectedly observed. This structure is in the plane group *p*6 and contains rhombic voids. The presence of high symmetry and porosity in the monolayer is also a rare occurrence for a molecule with C_s symmetry.[18,19] The occurrence of multiple packing forms in 2D crystallization is seeing increased scrutiny.[20-22] The amide structures investigated here provide a particularly dramatic example (Figure 2.2). We hypothesized that the two packing structures of the amide amphiphiles differ most dramatically in the hydrogen bonding and vdW interactions; experiments varying the functional groups and alkyl chain lengths to examine the relative role of intermolecular interactions support this claim.

2.2 Results and Discussion

The amide compounds with alkyl chains with between 12 and 18 carbons were synthesized and their 2D crystal structures formed at the 1-phenyloctane/highly oriented pyrolytic graphite (HOPG) interface were investigated by STM. The monolayer formed by **18-amide,** the amide compound with the longest alkyl chain investigated, satisfies close packing (Figure 2.2a, phase I). The shorter alkyl chain compounds, **12-amide**, **14-amide,** and **16-amide,** formed a phase containing rhombic voids (Figure 2.2d, phase II). The co-existence of a close packing and a rhombic nanoporous structure was observed without phase transformation for **16-amide** and **14-amide** (Figure 2.2b,c). The area covered by the rhombic structure increased as the alkyl chain length decreased. The close

packing structure exists as the major phase for **16-amide**. For **14-amide**, the nanoporous structure is the major phase and the nanoporous structure is observed as the sole phase for **12-amide**. In other words, the close packing structure is preferred for long chains at a given concentration.[22] The direction of alkyl chains in the rhombic nanoporous network matches the symmetry of HOPG and this suggests that the substrate may affect the crystal structure; however, a structure-determining role for alkyl-chain substrate alignment can be ruled out because longer alkyl chains do not favor the nanoporous structure. These results are consistent with the notion that as the alkyl chain length decreases, the hydrogen bonding interactions play a relatively more important role. In order to examine the role of hydrogen bonding, carboxylic acid analogs were synthesized (Figure 2.1). However, in contrast to the amide case, only a close packed phase was observed for the carboxylic acid amphiphiles. Both **18-acid** and **12-acid** satisfy close packing (Figure 2.3), though in a manner differing from **18-amide** (Figure 2.4). The absence of a porous phase is discussed below in the context of hydrogen bonding in the amide phase.

To our knowledge, rhombic void space has not been observed previously in 2D networks formed at the liquid/solid interface. The void widths of 2.2 nm and 4.0 nm (Figure 2.5) are comparable to the cavity sizes observed in other systems (~1-5 nm).[20-22] The $p6$ symmetry of the monolayer is unexpected because the molecular symmetry of the amphiphilic molecules is C_s and therefore does not allow for 3- or 6-fold rotation axes coincident with the molecule. To put this result in context, the relationship between molecular symmetry and monolayer symmetry was scrutinized by searching the Two-Dimensional Structural Database (2DSD), a catalog of packing patterns for molecules adsorbed at the liquid/solid interface.[17] The frequency of the plane group $p6$ was only 2.2% among all unique entries in the 2DSD. Most $p6$ symmetry monolayers are generated from molecules with 3- or 6-fold rotation axes (82%). Hydrogen bonding[11,18,23,24] and other geometric effects[21] have also induced $p6$. Thus, the fact that the carboxylic acid compounds do not adopt $p6$ symmetry suggests that the structure of the

hydrogen bonding network of the amide groups differs from that of the acid. High resolution images of each rotation axis in the nanoporous structure reveal six benzene rings (Figure 2.6d). The computed models of these provide molecular structures in detail. These axes are constructed from hydrogen bonding between aggregates, where an aggregate consists of three crystallographically inequivalent amide molecules (Z'=3) in an asymmetric unit (indicated by a red oval in Figure 2.5). A search of the 2DSD reveals that Z'=3 is very uncommon, occurring in 0.6% of entries. If there were only one molecule in the asymmetric unit, this low-symmetry amide could not reasonably form the 3- and 6-fold symmetric hydrogen-bonding patterns seen here (Figure 2.7). Through aggregate formation, this symmetry generation is possible. In the 3-fold rotation axis, a typical arrangement can be invoked (Figure 2.6a). However, an unusual hydrogen bonding structure involving a ring of twelve donors and six acceptors exists at the 6-fold axis, one which has not been reported in 2D or 3D crystal structures (Figure 2.6f). This model is supported by two facts: 1) it is found in several cases of three dimensional crystal structures of amide compounds that two lone pairs on oxygen make hydrogen bonds with two hydrogen atoms in an amide[25] and 2) the arrangement of benzene rings apparent in the high resolution STM image (Figure 2.6a,d) matches well with the computed model. When computed models are superimposed on Figure 2.6a,d with symmetry elements of the monolayer, the slight difference between these two axes is more clarified (Figure 2.6b,e). This is well commensurate with the high Z' value (Z'=3) where it has been suggested that Z'>1 is associated with strong non-covalent interactions in both 2D and 3D crystallization.[26,27] The absence of a porous phase for an acid might be due to a geometrical difference of hydrogen bonding; the bifurcated hydrogen bonds in an amide are not possible between acid groups (Figure 2.8).

2.3 Conclusions

This investigation shows the formation of high symmetry nanoporous molecular networks containing rhombic voids uncorrelated with molecular symmetry. Remarkably, amide amphiphilic molecules overcome this barrier to symmetry generation through forming an aggregate of three desymmetrized molecules as an asymmetric unit. The role of high Z' values in symmetric pattern generation requires additional scrutiny to determine if this is a general two-dimensional crystal engineering strategy capable of generating nanometer voids using low symmetry molecules.

2.4 Experimental section

2.4.1 Concentration of solutions

A concentration effect on the transformation from closed packed structure to open structure as concentration decreases was observed for **18-amide** (the longest amide amphiphile). **18-Amide** forms a close packed structure as shown in Figure 1a at 0.10 mM. When the solution of **18-amide** was diluted step by step, the co-existence of the closed packing structure and the rhombic nanoporous structure was observed at 0.033 mM. Therefore, the mostly saturated solutions (0.10 mM) for all compounds were used to compare the effect of alkyl-chain length while holding the concentration effect constant except in the case of **12-acid** (the shortest acid amphiphile required a concentration of greater than this to observe a monolayer and so 1.0 mM was used).

2.4.2 Synthesis and characterization

Materials: Sodium hydroxide, potassium carbonate and all solvents were purchased from Fisher Scientific except ethyl alcohol (Decon Labs, Inc.). 4-Cyanophenol and 1-bromoalkanes were purchased from Acros Organics. All reagents were used as received.

General preparation of 4-alkyloxybenzonitriles: To a mixture of 4-cyanophenol (16.8 mmol) and 1-bromoalkane (16.8 mmol) in N,N-dimethylformamide (100 mL) was added K_2CO_3 (18.8 mmol). The mixture was heated at 60 °C for 18 hr. CH_2Cl_2 (100 mL) was added to the mixture and the organic layer was washed with brine three times. The organic layer was dried over anhydrous $MgSO_4$ and solvent was removed under vacuum. Pure product was obtained by column chromatography with 15% ethyl acetate in hexane.

Preparation of 4-octadecycloxybenzonitrile: Yield: 72%. mp: 65.5-66.5 °C. IR: 2915, 2848, 2217, 1608, 1573, 1508, 1473, 1400, 1301, 1259, 1170, 1035, 833, 719 cm^{-1}. ^{1}H NMR (400 MHz, CDCl$_3$, δ): 0.88 (t, J = 6.8 Hz, 3H), 1.26-1.57 (m, 30H), 1.80 (quint, J = 7.0 Hz, 2H), 3.99 (t, J = 6.5 Hz, 2H), 6.93 (AA' in an AA'XX' spin system, 2H), 7.57 (XX' in an AA'XX' spin system, 2H). ^{13}C NMR (100 MHz, CDCl$_3$, δ): 14.36, 22.93, 26.16, 29.22, 29.56, 29.77 (broad), 32.16, 68.66, 103.88, 115.41, 119.56, 134.18, 162.70. Anal. Calcd for C$_{25}$H$_{41}$NO: C 80.80 H 11.12, N 3.77; Found: C 80.96, H 11.04, N 3.65. MS (EI+): m/z 371.4 [M+].

Preparation of 4-hexadecyloxybenzonitrile: Yield: 77%. mp: 59.7-60.8 °C. IR: 2915, 2848, 2217, 1608, 1573, 1510, 1475, 1400, 1301, 1259, 1170, 1026, 833, 811, 547 cm^{-1}. ^{1}H NMR (400 MHz, CDCl$_3$, δ): 0.88 (t, J = 6.8 Hz, 3H), 1.27-1.49 (m, 26H), 1.80 (quint, J = 7.0 Hz, 2H), 4.00 (t, J = 6.5 Hz, 2H), 6.93 (AA' in an AA'XX' spin system, 2H), 7.56 (XX' in an AA'XX' spin system, 2H). ^{13}C NMR (100 MHz, CDCl$_3$, δ): 14.29, 22.92, 26.20, 29.28, 29.56, 29.77 (broad), 32.18, 68.78, 104.13, 115.53, 119.45, 134.19, 162.80. Anal. Calcd for C$_{23}$H$_{37}$NO: C 80.41 H 10.86, N 4.08; Found: C 80.68, H 11.07, N 4.09. MS (EI+): m/z 343.4 [M+].

Preparation of 4-tetradecyloxybenzonitrile: Yield: 60%. mp: 49.2-51.5 °C. IR: 2915, 2848, 2217, 1608, 1573, 1510, 1475, 1398, 1301, 1257, 1170, 833, 811, 547 cm^{-1}. ^{1}H NMR (400 MHz, CDCl$_3$, δ): 0.87 (t, J = 7.0 Hz, 3H), 1.25-1.44 (m, 22H), 1.79 (quint, J = 7.0 Hz, 2H), 3.98 (t, J = 6.5 Hz, 2H), 6.92 (AA' in an AA'XX' spin system, 2H), 7.56

(XX' in an AA'XX' spin system, 2H). ^{13}C NMR (100 MHz, CDCl$_3$, δ): 14.35, 22.92, 26.15, 29.20, 29.54, 29.77 (broad), 32.15, 68.64, 103.84, 115.38, 119.56, 134.17, 162.68. Anal. Calcd for C$_{21}$H$_{33}$NO: C 79.95, H 10.54, N 4.44; Found: C 79.68, H 10.65, N 4.38. MS (EI+): m/z 315.4 [M+].

Preparation of 4-dodecyloxybenzonitrile: Yield: 74%. mp: 43.8-45.1 °C. IR: 2915, 2848, 2217, 1608, 1573, 1508, 1475, 1398, 1301, 1255, 1170, 833, 545 cm^{-1}. ^{1}H NMR (400 MHz, CDCl$_3$, δ): 0.87 (t, J = 7.0 Hz, 3H), 1.25-1.46 (m, 18H), 1.78 (quint, J = 7.0 Hz, 2H), 3.98 (t, J = 6.5 Hz, 2H), 6.92 (AA' in an AA'XX' spin system, 2H), 7.55 (XX' in an AA'XX' spin system, 2H). ^{13}C NMR (100 MHz, CDCl$_3$, δ): 14.26, 22.84, 26.08, 29.13, 29.47, 29.77 (broad), 32.06, 68.57, 103.77, 115.32, 119.44, 134.06, 162.62. Anal. Calcd for C$_{19}$H$_{29}$NO: C 79.39, H 10.17, N 4.87; Found: C 79.46, H 10.31, N 4.91. MS (EI+): m/z 287.3[M+].

General preparation of 4-(alkyloxy)benzamides: To the solution of the 4-alkyloxybenzonitrile (0.27 mmol) in ethanol (40 mL) was added NaOH (8.0 mmol) in deionized water (40 mL). The reaction mixture was heated at 80 °C for 24 hr and neutralized with 1.0 N HCl. The precipitated product was collected by vacuum filtration. The product was dissolved in hot ethanol, recrystallized by cooling to 0 °C and collected by filtration. This recrystallization process was repeated three more times.

Preparation of 4-octadecyloxybenzamide **(18-amide)**: Yield: 52%. mp: 136.5-138.1 °C. IR: 3427, 3189, 2917, 2850, 1648, 1618, 1577, 1515, 1471, 1423, 1307, 1251, 1145, 1035, 846, 622 cm^{-1}. ^{1}H NMR (400 MHz, CDCl$_3$, δ): 0.86 (t, J= 6.8 Hz, 3H), 1.25-1.58 (m, 30H), 1.80 (quint, J = 7.0 Hz, 2H), 4.00 (t, J = 6.6 Hz, 2H), 6.93 (XX' in an AA'XX' spin system, 2H), 7.77 (AA' in an AA'XX' spin system, 2H).^{13}C NMR (100 MHz, CDCl$_3$, δ): 14.35, 22.92, 26.22, 29.35, 29.60, 29.80 (broad), 32.16, 68.47, 114.51, 125.46, 129.48, 162.48, 169.03. Anal. Calcd for C$_{25}$H$_{43}$NO$_2$: C 77.07, H 11.12, N 3.60; Found: C 77.15, H 11.09, N 3.52. MS (EI+): m/z 389.4 [M+].

Preparation of 4-(hexadecyloxy)benzamide (**16-amide**): Yield: 85%. mp: 137.0-137.5 °C. IR: 3378, 3180, 2919, 2850, 1645, 1608, 1571, 1517, 1469, 1421, 1311, 1257, 1176, 1016, 856, 622 cm^{-1}. ^{1}H NMR (400 MHz, CDCl$_3$, δ): 0.87 (t, J = 7.0 Hz, 3H), 1.25-1.47 (m, 26H), 1.80 (quint, J = 7.0 Hz, 2H), 3.99 (t, J = 6.5 Hz, 2H), 6.92 (AA' in an AA'XX' spin system, 2H), 7.56 (XX' in an AA'XX' spin system, 2H). ^{13}C NMR (100 MHz, CDCl$_3$, δ): 14.37, 22.93, 26.22, 29.34, 29.60, 29.80 (broad), 32.16, 68.52, 114.59, 124.78, 129.66, 162.75, 169.52. Anal. Calcd for C$_{23}$H$_{39}$NO$_2$: C 76.40, H 10.87, N 3.87; Found: C 76.53, H 11.04, N 3.89. MS (EI+): m/z 361.4 [M+].

Preparation of 4-(tetradecyloxy)benzamide (**14-amide**): Yield: 77%. mp: 138.4-139.1 °C. IR: 3378, 3180, 2919, 2850, 1645, 1608, 1571, 1517, 1469, 1421, 1311, 1257, 1176, 1016, 856, 622 cm^{-1}. ^{1}H NMR (400 MHz, CDCl$_3$, δ): 0.87 (t, J = 7.0 Hz, 3H), 1.26-1.47 (m, 22H), 1.80 (quint, J = 7.0 Hz, 2H), 3.99 (t, J = 6.5 Hz, 2H), 6.92 (AA' in an AA'XX' spin system, 2H), 7.56 (XX' in an AA'XX' spin system, 2H). ^{13}C NMR (100 MHz, CDCl$_3$, δ): 14.36, 22.93, 26.22, 29.34, 29.60, 29.80 (broad), 32.16, 68.50, 114.57, 124.94, 129.62, 162.67, 169.47. Anal. Calcd for C$_{21}$H$_{35}$NO$_2$: C 75.63, H 10.58, N 4.20; Found: C 75.23, H 10.61, N 4.19. MS (EI+): m/z 333.4 [M+]

Preparation of 4-(dodecyloxy)benzamide (**12-amide**): Yield: 60%. mp: 140.3-141.5 °C. IR: 3378, 3180, 2919, 2850, 1646, 1610, 1573, 1517, 1469, 1421, 1311, 1257, 1174, 1016, 856, 622cm^{-1}. ^{1}H NMR (400 MHz, CDCl$_3$, δ): 0.88 (t, J = 7.0 Hz, 3H), 1.26-1.49 (m, 18H), 1.80 (quint, J = 7.0 Hz, 2H), 4.00 (t, J = 6.5 Hz, 2H), 6.92 (AA' in an AA'XX' spin system, 2H), 7.56 (XX' in an AA'XX' spin system, 2H). ^{13}C NMR (100 MHz, CDCl$_3$, δ): 14.34, 22.90, 26.20, 29.32, 29.56, 29.58 (broad), 32.13, 68.47, 114.53, 124.98, 129.58, 162.62, 169.45. Anal. Calcd for C$_{19}$H$_{31}$NO$_2$: C74.71, H 10.23, N 4.59; Found: C 74.47, H 10.19, N 4.59. MS (EI+): m/z 305.3 [M+].

General Preparation of 4-alkyloxybenzoic acids: To the solution of the 4-alkyloxybenzonitrile (0.32 mmol) in ethylene glycol (5.0 mL) was added NaOH (3.25 mmol). The reaction mixture was heated at 170 °C for 30 hr and then cooling to room

temperature. The mixture was neutralized with 1.0 N HCl. The precipitated product was collected by vacuum filtration. The product was dissolved in hot ethanol, recrystallized by cooling to 0 °C and collected by filtration. This recrystallization process was repeated three more times.

Preparation of 4-octadecyloxybenzoic acid (**18-acid**): Yield: 39%. mp: 104.2-105.0 °C. IR: 3100 (br), 2915, 2848, 2663, 2561, 1687, 1672, 1606, 1579, 1513, 1469, 1432, 1307, 1257, 1170, 939, 846, 771, 648 cm^{-1}. ^{1}H NMR (400 MHz, CDCl$_3$, δ): 0.87 (t, J = 7.0 Hz, 3H), 1.25-1.49 (m, 30H), 1.80 (quint, J = 7.0 Hz, 2H), 4.02 (t, J = 6.5 Hz, 2H), 6.92 (AA' in an AA'XX' spin system, 2H), 8.03 (XX' in an AA'XX' spin system, 2H). ^{13}C NMR (100 MHz, CDCl$_3$, δ): 14.33, 22.93, 26.21, 29.33, 29.59, 29.78 (broad), 32.16, 68.55, 114.47, 121.41, 132.55, 163.90, 170.37. Anal. Calcd for C$_{25}$H$_{42}$O$_3$: C 76.87, H 10.84; Found: C 76.12, H 10.87. MS (EI+): m/z 390.4 [M+].

Preparation of 4-dodecyloxybenzoic acid (**18-acid**): Yield: 40%. mp: 93.5-94.6 °C. IR: 3050 (br), 2917, 2850, 2663, 2561, 1689, 1672, 1606, 1577, 1511, 1469, 1432, 1305, 1257, 1170, 941, 846, 771, 649 cm^{-1}. ^{1}H NMR (400 MHz, CDCl$_3$, δ): 0.88 (t, J = 7.0 Hz, 3H), 1.26-1.46 (m, 18H), 1.80 (quint, J = 7.0 Hz, 2H), 4.02 (t, J = 6.5 Hz, 2H), 6.93 (AA' in an AA'XX' spin system, 2H), 8.03 (XX' in an AA'XX' spin system, 2H). ^{13}C NMR (100 MHz, CDCl$_3$, δ): 14.11, 22.68, 25.97, 29.08, 29.34, 29.54 (broad), 31.91, 68.28, 114.18, 121.32, 132.31, 163.68, 171.73. Anal. Calcd for C$_{19}$H$_{30}$O$_3$: C 74.47, H 9.87; Found: C 74.26, H 9.90. MS (EI+): m/z 306.3 [M+].

2.5 References

(1)   Plass, K. E.; Engle, K. M.; Cychosz, K. A.; Matzger, A. J. *Nano Lett.* **2006**, *6*, 1178.

(2)   Kampschulte, L.; Werblowsky, T. L.; Kishore, R. S. K.; Schmittel, M.; Heckl, W. M.; Lackinger, M. *J. Am. Chem. Soc.* **2008**, *130*, 8502.

(3)   Wei, Y.; Tong, W.; Zimmt, M. B. *J. Am. Chem. Soc.* **2008**, *130*, 3399.

(4)   Li, S. -S.; Yan, H. -J.; Wan, L. -J.; Yang, H. -B.; Northrop, B. H.; Stang, P. J. *J. Am. Chem. Soc.* **2007**, *129*, 9268.

(5)   Lei, S.; Tahara, K.; Feng, X.; Furukawa, S.; De Schryver, F. C.; Müllen, K.; Tobe, Y.; De Feyter, S. *J. Am. Chem. Soc.* **2008**, *130*, 7119.

(6)   Scherer, L. J.; Merz, L.; Constable, E. C.; Housecroft, C. E.; Neuburger, M.; Hermann, B. A. *J. Am. Chem. Soc.* **2005**, *127*, 4033.

(7)   Fang, H.; Giancarlo, L. C.; Flynn, G. W. *J. Phys. Chem. B* **1999**, *103*, 5712.

(8)   Tao, F.; Bernasek, S. L. *J. Am. Chem. Soc.* **2005**, *127*, 12750.

(9)   Furukawa, S.; Uji-i, H.; Tahara, K.; Ichikawa, T.; Sonoda, M.; De Schryver, F. C.; Tobe, Y.; De Feyter, S. *J. Am. Chem. Soc.* **2006**, *128*, 3502.

(10)   Mu, Z.; Shu, L.; Fuchs, H.; Mayor, M.; Chi, L. *J. Am. Chem. Soc.* **2008**, *130*, 10840.

(11)   Zhou, H.; Dang, H.; Yi, J. H.; Nanci, A.; Rochefort, A.; Wuest, J. D. *J. Am. Chem. Soc.* **2007**, *129*, 13774.

(12)   Lu, J.; Lei, S.-b.; Zeng, Q.-d.; Kang, S.-z.; Wang, C.; Wan, L.-j.; Bai, C.-l. *J. Phys. Chem. B* **2004**, *108*, 5161.

(13)   Tahara, K.; Lei, S.; Mamdouh, W.; Yamaguchi, Y.; Ichikawa, T.; Uji-i, H.; Sonoda, M.; Hirose, K.; De Schryver, F. C.; De Feyter, S.; Tobe, Y. *J. Am. Chem. Soc.* **2008**, *130*, 6666.

(14)   Furukawa, S.; Tahara, K.; De Schryver, F. C.; Van der Auweraer, M.; Tobe, Y.; De Feyter, S. *Angew. Chem., Int. Ed.* **2007**, *46*, 2831.

(15)   Griessl, S. J. H.; Lackinger, M.; Jamitzky, F.; Markert, T., Hietschold, M.; Heckl, W. M. *Langmuir* **2004**, *20,* 9403.

(16)   Schull, G.; Douillard, L.; Fiorini-Debuisschert, C.; Charra, F.; Mathevet, F.; Kreher, D.; Attias, A.-J. *Nano Lett.* **2006**, *6*, 1360.

(17)   Plass, K. E.; Grzesiak, A. L.; Matzger, A. J. *Acc. Chem. Res.* **2007**, *40,* 287.

(18)   Mourran, A.; Ziener, U.; Möller, M.; Suarez, M.; Lehn, J.-M. *Langmuir* **2006**, *22,* 7579.

(19)   Merz, L.; Güntherodt, H.-J.; Scherer, L. J.; Constable, E. C.; Housecroft, C. E.; Neuburger, M. Hermann, B. A. *Chem. Eur. J.* **2005**, 11, 2307.

(20)   Lackinger, M.; Griessl, S.; Heckl, W. M.; Hietschold, M.; Flynn, G. W. *Langmuir* **2005**, *21*, 4984.

(21)   Tahara, K.; Furukawa, S.; Uji-i, H.; Uchino, T.; Ichikawa, T.; Zhang, J.; Mamdouh, W.; Sonoda, M.; De Schryver, F. C.; De Feyter, S.; Tobe, Y. *J. Am. Chem. Soc.* **2006**, *128*, 16613.

(22)   Lei, S.; Tahara, K.; De Schryver, F. C.; Van der Auweraer, M.; Tobe, Y.; De Feyter, S. *Angew. Chem., Int. Ed.* **2008**, *47*, 2964.

(23)   Jonkheijm, P.; Miura, A.; Zdanowska, M.; Hoeben, F. J. M.; De Feyter, S.; Schenning, A. P. H. J.; De Schryver, F. C.; Meijer, E. W. *Angew. Chem., Int. Ed.* **2004**, *43*, 74.

(24)   De Feyter, S.; Gesquiere, A.; Klapper, M.; Mullen, K.; De Schryver, F. C. *Nano Lett.* **2003**, *3*, 1485.

(25)   Valle, G.; Crisma, M.; Toniolo, C.; Yu, K. -L.; Johnson, R. L. *J. Chem. Soc., Perkin Trans.2* **1989**, 83.

(26)   Anderson, K. M.; Goeta, A. E.; Hancock, K. S. B.; Steed, J. W., *Chem. Commun.* **2006**, 2138.

(27)   Plass, K. E.; Kim, K.; Matzger, A. J., *J. Am. Chem. Soc.* **2004**, *126*, 9042.
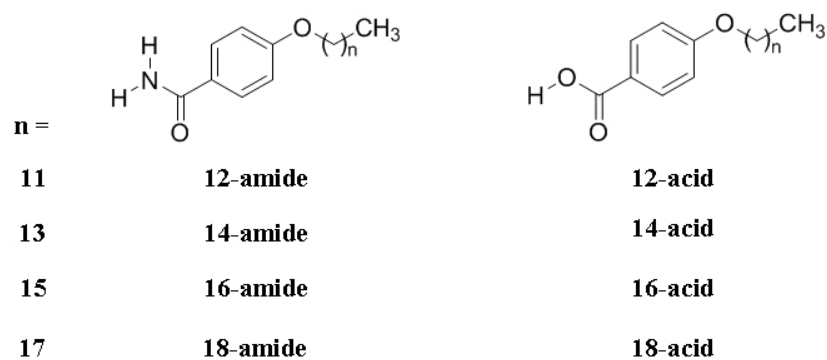
Figure 2.1. Structures of all molecules examined. The name given to each molecule represents a functional group and the number of carbon in an alkyl chain.
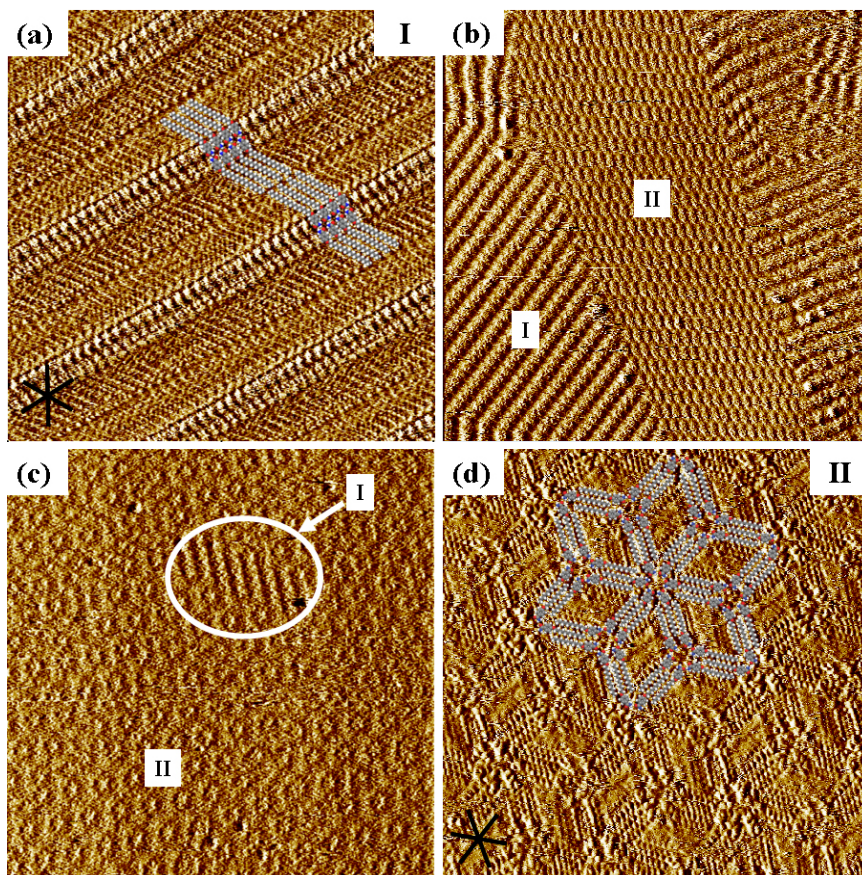
Figure 2.2. STM images of (a) **18-amide** (20×20 nm^2), (b) **16-amide** (100×100 nm^2), (c) **14-amide** (100×100 nm^2), and (d) **12-amide** (20×20 nm^2). All 2D crystals were formed at the phenyloctane/HOPG interface. The computed models of 2D crystals of **18-amide** and **12-amide** are superimposed on STM images to facilitate interpretation. The black axes indicate the symmetry of HOPG under the monolayer.
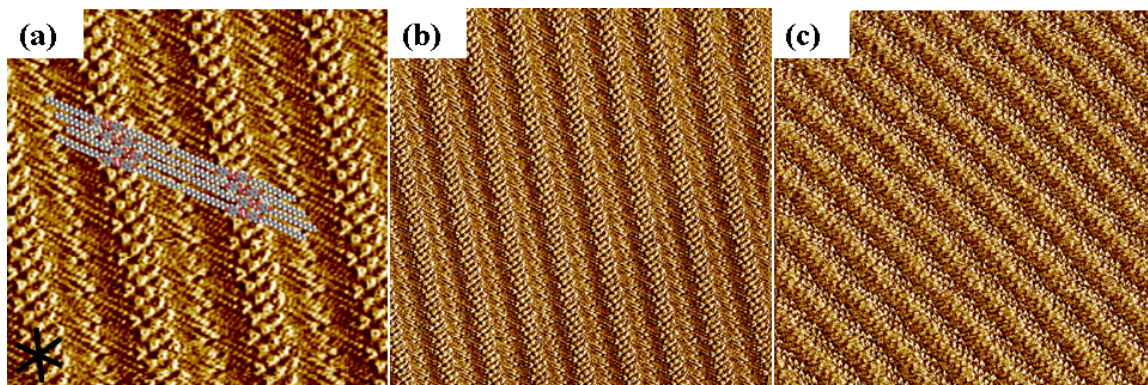
Figure 2.3. STM images of (a) **18-acid** (20×20 nm^2), (b) **18-acid** (50×50 nm^2) and (c) **12-acid** (50×50 nm^2). All 2D crystals were formed at the phenyloctane/HOPG interface. The computed model of 2D crystal of **18-acid** is superimposed on STM image to facilitate interpretation. The black axes indicate the symmetry of HOPG under the monolayer.
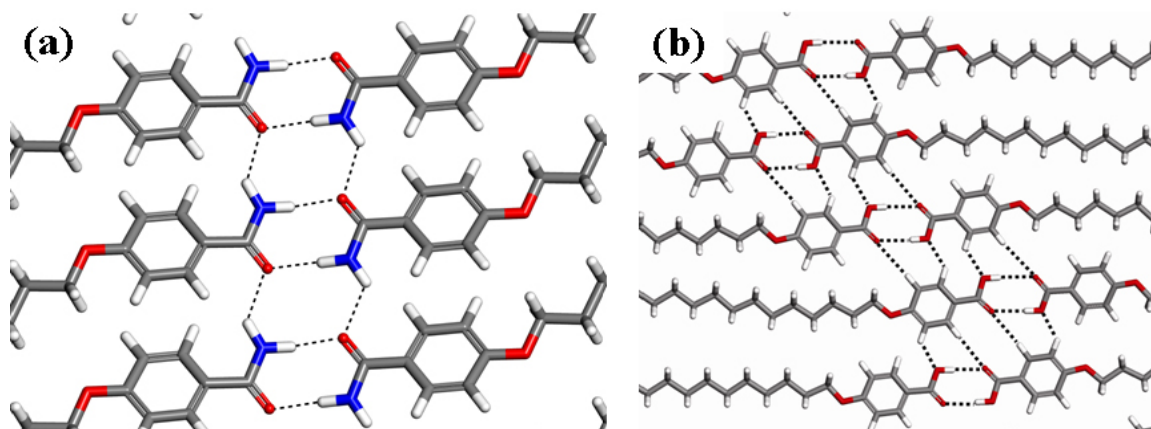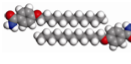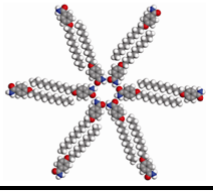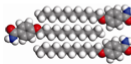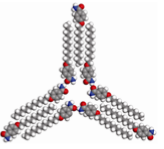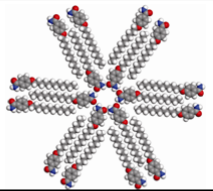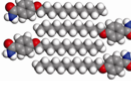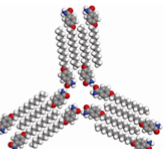
Figure 2.4. The computed models of 2D crystals of (a) **18-amide** and (b) **18-acid** show the hydrogen bonding structure in detail.
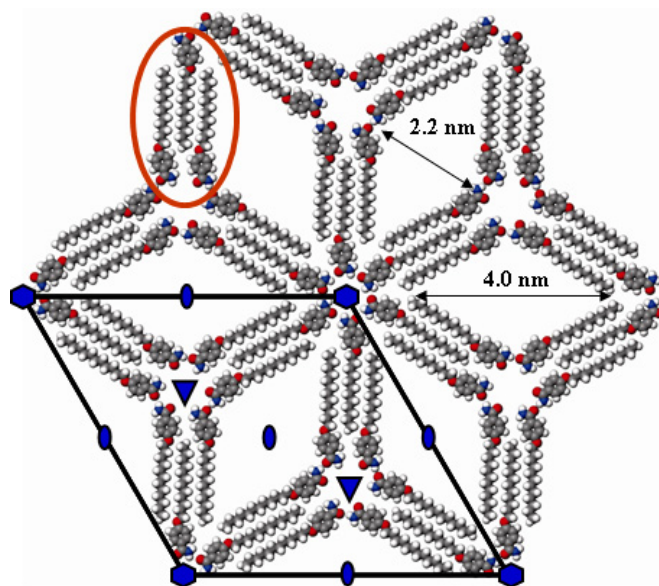
Figure 2.5. The computed model of the rhombic nanoporous network formed by 12-amide with a unit cell. The red oval indicates an asymmetric unit of the rhombic nanoprous network.
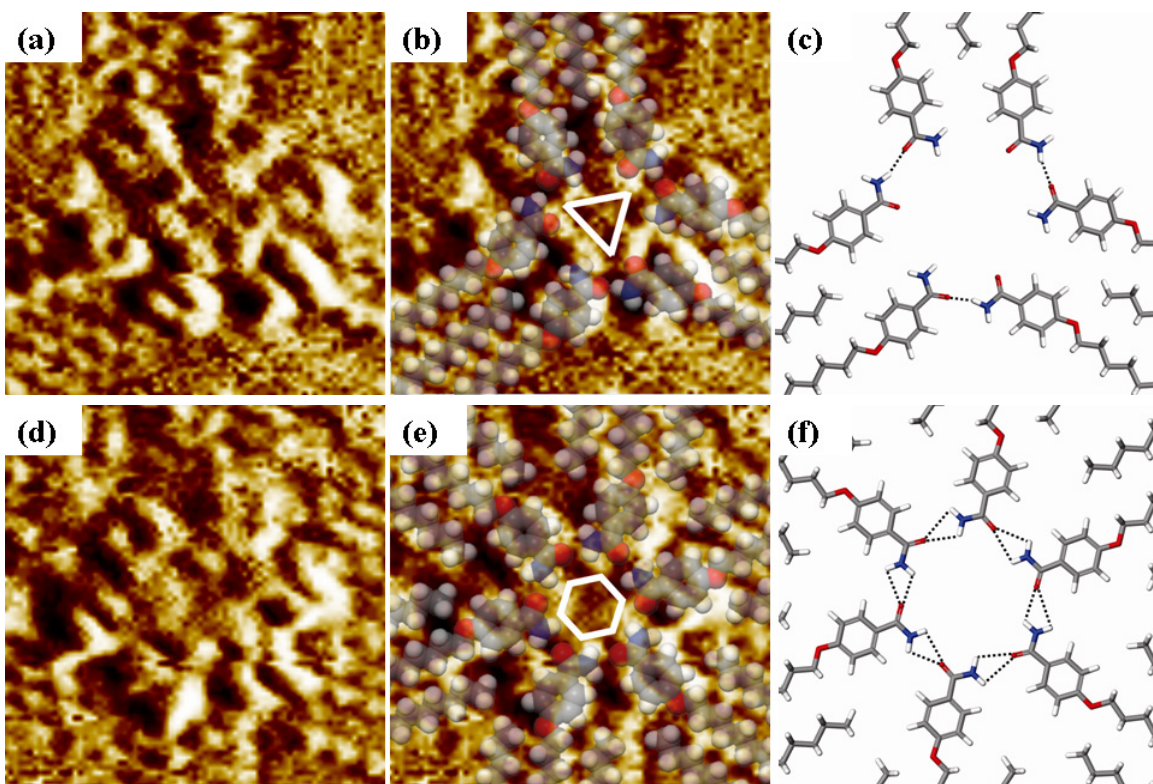
Figure 2.6. STM images (3×3 nm^2) of (a) 3-fold and (d) 6-fold rotation axes in the rhombic nanoporous network. (b),(e) The computed model is superimposed on STM images. (e), (f) The computed model shows the corresponding hydrogen bonding networks.

Aggregation	3-fold rotation	6-fold rotation
	—	
		—

Figure 2.7. The structures of three possible aggregations and their possible orientation to make a 3- and 6-fold rotation axes in the rhombic nanoporous network. The only aggregation of three molecules can simultaneously make a 3- and 6-fold rotation axes through a reasonable hydrogen bonding network.
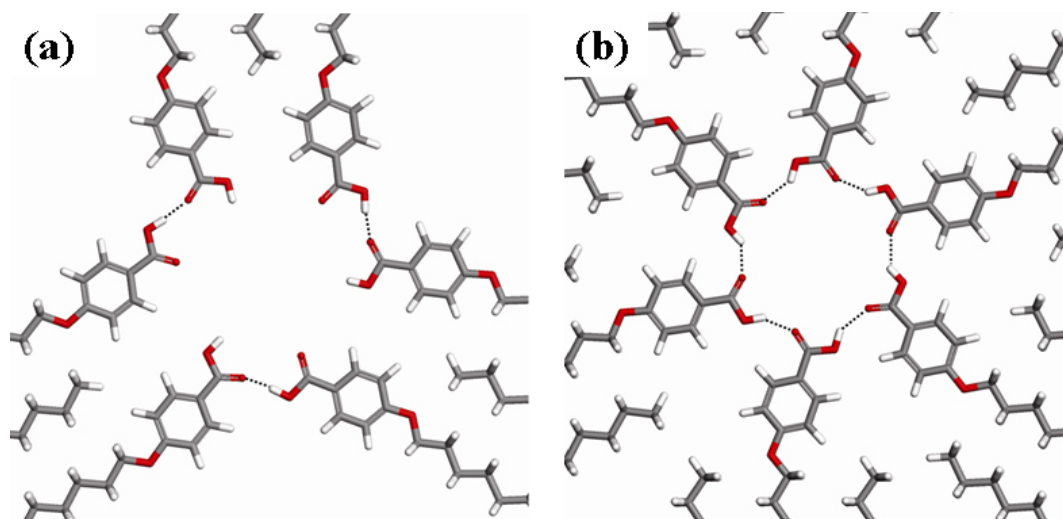
Figure 2.8. The hydrogen bonding networks of (a) 3-fold and (b) 6-fold rotation axes from the computed model of the hypothetical rhombic nanoporous form of **12-acid**. The geometrical difference between acid and amide molecule for this nanoporous structure is the hydrogen bonding in the 6-fold rotation axis.

25

Table 2.1. Experimental and Computed Unit Cell Parameters for All Molecules Examined in All Phases Observed.

molecule	computed			experimental			plane group
	a (Å)	b (Å)	α (deg)	a (Å)	b (Å)	α (deg)	
18-amide	63.1	5.1	68.9	67.8±1.1	5.1±0.1	63±1	$p2$
18-acid	64.1	19.5	58.0	70.2±2.0	18.0±1.0	57±2	$p2$
12-amide	66.2	65.6	60.2	65.6±1.3	64.9±1.4	59±2	$p6$
12-acid	47.5	19.4	57.8	48.5±2.1	19.4±0.9	58±2	$p2$

CHAPTER 3

Six Different Assemblies from One Building Block: Two-Dimensional Crystallization of an Amide Amphiphile

Published in J. Am. Chem. Soc. 2010, 132, 11364-11371

3.1 Introduction

Polymorphism is defined as the ability of a compound to exist in multiple crystalline phases each differing solely in arrangement or conformation of molecules within a solid. Predicting the occurrence of this phenomenon in three-dimensional (3D) crystallization represents one of the greatest scientific challenges in solid-state chemistry. Furthermore, because of its importance in determining technologically relevant properties of a wide range of materials, including pharmaceuticals,[1,2] explosives,[3,4] and nonlinear optical materials,[5,6] there is significant financial motivation to generate a more predictive understanding of crystal polymorphism. One of the methods to study this phenomenon is the use of models such as two-dimensional (2D) crystals spontaneously formed at the liquid/solid interface; the reduced dimensionality of assembly dramatically simplifies the system with only 17 plane groups possible in 2D crystallization compared to 230 space groups in 3D crystallization. Furthermore, the physisorbed molecular assemblies can be investigated with the aid of scanning tunneling microscopy (STM) offering submolecular resolution of both periodic and non-periodic packing in a time dependent fashion.[7-10] However, developing a compound showing the ability to exist in multiple phases in 2D crystallization is essential to study polymorphic phenomenon (e.g., the formation of a

metastable polymorph during attempted cocrystallization, see also Chapter 4.).[11-13] This chapter presents the ability of a simple amide amphiphile with *Cs* symmetry to form at least six phases differing considerably in aggregation mode;[14] this level of phase diversity compares favorably to highly polymorphic molecules found in the Cambridge Structural Database (CSD) where only one compound, 5-methyl-2-[(2-nitrophenyl)amino]-3-thiophenecarbonitrile (ROY), exceeds five crystal structures.[15,16] The observation of highly symmetric and complex assemblies from this simple molecule provides an unprecedented view of the range of structural diversity that can arise from even a simple molecular building block.

Various tools to generate polymorphs in 3D such as controlling solvent/temperature,[17] epitaxial crystal growth/pseudoseeding,[18-23] polymer-induced heteronucleation,[24] and tailor-made additives[25-27] have found wide application. In 2D crystallization, additional packing motifs are typically obtained by controlling solvent identity.[28-33] For example, trimesic acid (TMA) forms chickenwire and flower phases depending on the alkyl-chain length of alkanoic acid solvents.[31] Recently, the role of concentration has been exploited to generate 2D nanoporous networks. For example, triangle-shaped fused dehydrobenzo[12]annulenes (DBA) bearing alkyl chains with 14 or 16 carbons form two different nanoporous structures arising from the close packed structure by dilution, an effect demonstrated to be thermodynamically driven.[34] These examples reveal that, as in three dimensions,[35] the geometry of the building block plays a key role in determining arrangements in 2D crystallization; the molecular symmetry of TMA and triangle-shaped DBA derivatives facilitate the formation of high symmetry monolayers bearing 3-fold rotation axes, coinciding with molecular symmetry elements, through hydrogen bonding or van der Waals interactions. In contrast with these high symmetry molecules, it has been shown that low symmetry amide amphiphiles can overcome the geometric barrier to build highly symmetric monolayers by forming an aggregate consisting of three molecules.[36] Here we report several new phases of a low

symmetry amide amphiphile bearing an alkyl chain including the unprecedented finding of six different phases: three close-packed structures and three nanoporous structures. In these structures, various numbers of inequivalent molecules in the asymmetric unit (e.g.; $Z' = 2, 3$, and 6) were observed. These results are interpreted in the context of kinetic and thermodynamic concentration dependent-behavior under ambient conditions. These unique behaviors in 2D crystallization make it possible to distinguish the results from true polymorphism in 3D crystallization because concentration-dependent changes in stability can not occur in 3D.

3.2 Results and Discussion

The molecular structure investigated here and possible aggregation modes found in the present study are shown in Figure 3.1. **18-Amide** consists of hydrophobic and hydrophilic portions and this amphiphilic nature plays a significant role in determining 2D crystal structure. The key interactions are 1) van der Waals interactions, which occur mainly among alkyl chains and 2) hydrogen bonding between amide groups. These non-covalent interactions are satisfied to different extents in the various aggregates in Figure 3.1 and, if stable, each is expected to generate a different pattern at the liquid/highly oriented pyrolytic graphite (HOPG) interface. In order to investigate this possibility, solvents and the concentration of **18-amide** solutions were varied in the search for new phases much in the same manner as crystalline polymorph screening is carried out for three dimensional crystals. Two different solvents, heptanoic acid and phenyloctane, were selected to vary polarity and induce different ordering of adsorbates because, molecule-molecule, molecule-substrate, molecule-solvent and solvent-substrate interactions conspire to determine the packing motif.

All phases of **18-amide** formed at the liquid/HOPG interface are schematically shown in Figure 3.2. The number of molecules in the asymmetric unit (Z' value) is

indicated for all phases except phase III, which has a one-dimensional (1D) periodicity resulting in an unusual unit cell with one infinite axis.[37] The amide amphiphile formed six different phases; three close-packed structures, one porous network with less than 1 nm voids and two nanoporous networks with over 1 nm voids. Their unit cell parameters are shown in Table 3.1 and densities are calculated to discuss their stability below in the context of stabilities of phases. In order to describe each phase, aggregate modes observed from each phase are assigned to building blocks consisting of several **18-amide** molecules as shown in Figure 3.1.

Close-packed Structures. The close-packed structures of **18-amide** are shown in Figure 3.3. One structure arises in 1.0 mM heptanoic acid solution (phase I) and two structures (phase II and III) arise in 0.10 mM phenyloctane solution. In recent studies, the application of Fourier Transform Infrared-Attenuated Total Reflection (FTIR-ATR) revealed a direct relationship between aggregates in solution and hydrogen bonded motifs in the crystal forms.[38] For example, hydrogen bonded dimers were observed in chloroform solution of tetrolic acid and this solution nucleated the α-form whereas dimer formation was disturbed in ethanol solution, resulting in nucleating the β-form. The same considerations apply in the present case; in the phenyloctane solution of **18-amide**, hydrogen bonded dimers (**A1** mode) would be favored and nucleate to form phase II which has the hydrogen bonding network (phase II, Figure 3.10) without interdigitation of alkyl chains. On the other hand, in a heptanoic acid solution of **18-amide**, the **A2** mode forms instead, resulting in the interdigitation of alkyl chains. The stabilites of these two phases are discussed below in the context of thermodynamics. For these two phases, each of **18-amide** molecules (Z'=1.0) is related by a 2-fold rotation axis, resulting in *p2* symmetry.

In 0.10 mM phenyloctane solution, another motif (phase III, Figure 3.3c and 3.3d) was observed as a minor phase (Figure 3.4). In this phase, there are two key structural characteristics: (1) the one-dimensionally periodic ordering, creating an infinite unit cell

parameter along one axis (phase III, Figure 3.2) and (2) the coexistence of two different aggregation modes (**A1** and **A4**). Figure 3.3c and 3.3d clearly show the molecular ordering of this phase. Aggregates consisting of four molecules (**A4**, Figure 3.1) are ordered along one axis between two columns of the sort comprising phase II. Since it is not feasible to form appropriate hydrogen bonds between **A4** aggregates in this arrangement, additional molecules are required to stabilize this phase by hydrogen bonding. The proposed model is shown in Figure 3.3d. This model is supported by the vacancies of periodically ordered aromatic rings in the phase-II-type columns indicated by blue arrows (Figure 3.3c, Figure 3.5). Although the aromatic rings are absent, the missing alkyl chains are not observed, indicating the opposite orientation of **18-amide**. These molecules play a critical role in promoting compatibility between two different aggregation modes by hydrogen bonding with **A4** aggregates inserted between the columns resembling phase II. This phase demonstrates that if there is compatibility of geometry and functionality between the different aggregates, more complex nanoscale features can arise.

Porous Network (< 1 nm void). Recently, it has been reported that nanoporous networks with cavities are formed from dilute solution where the adsorption-desorption equilibrium determines the surface coverage of the close-packed vs. nanoporous structure.[39-41] When the concentrations of the heptanoic acid solution was reduced from 1000 to 20 μM, a porous network with less 1 nm voids was observed in the concentration range from 500 to 100 μM (phase VI, Figure 3.6). The high resolution STM images of this phase reveal that there are six molecules with coexistence of both **A2** and **A5** aggregation modes in the unit cell. The combination of these different modes causes a periodic porous network with wavy boundaries between columns as shown in Figure 3.7. In order to maintain a network of hydrogen bonds at the column interfaces, the amide groups must all point in the same direction. Furthermore, the lack of contrast between adjacent columns suggests that amide orientation does not flip between columns.[42,43]

Therefore the plane group of this phase is $p1$ and the crystallographic asymmetric unit contains six molecules (Z'=6.0); no examples of Z' equal to 6.0 are found in the 2DSD.[14]

Nanoporous Networks (> 1 nm void). When the concentration of the analyte in phenyloctane solution was varied from 100 to 5 μM, two different nanoporous networks were observed in the concentration range from 33 to 5 μM: the rhombic nanoporous network (Figure 3.8c) and the honeycomb network (Figure 3.8a). The characteristics of the rhombic network formed by **18-amide** analogues with shorter alkyl chains were previously reported.[36] From dilute solutions, **18-amide** preferably forms the rhombic nanoporous network instead of forming a close-packed structure (phase II) (Figure 3.9). **18-Amide** forms an aggregate of three molecules (**A3**, Figure 3.1) to generate 3- and 6-fold rotation axes in the monolayer symmetry of $p6$ (Figure 3.8d). This **A3** aggregate corresponds to the number of molecules in the asymmetric unit (Z'=3.0). A search of the 2DSD reveals that this high value is very uncommon, occurring in 0.6% of entries where most crystals (over 86 %) in 2D and 3D have Z'=1.0 or 0.5.[14,44] The Z'=3.0 indicates that three molecules are related to all others by 3- and 2-fold rotation axes, giving $p6$ symmetry. Because the **A3** mode is not kinetically preferable in phenyloctane, the formation of phase V is due to the influence of thermodynamic factors leading to forming less dense forms in dilute solutions. This claim is supported by the observation of the phase transformation from phase II to phase V in two different situations: (1) when 10 μM solution was placed on HOPG, phase II was initially observed as a kinetic form and subsequently transformed to phase V within one hour and (2) when the concentration of the solution on HOPG was decreased by adding solvent from 50 to 20 μM, the phase transformation from phase II to phase V was observed. The driving force for this transformation is discussed below in the context of thermodynamics. In addition, the present case demonstrates that the size of the rhombic shaped void is controllable by adjusting alkyl chain length because the void width of 2.6×5.3 nm^2 is enlarged from the 2.2×4.0 nm^2 formed by the amide amphiphile containing C$_{12}$ alkyl chain.[36]

During modeling of the rhombic network (phase V), the aggregation mode of **A4** was considered and it was revealed that **A4** can generate only 3-fold rotation axes potentially leading to a honeycomb network. This honeycomb network (phase IV) with a void diameter of 6.3 nm was observed in dilute phenyloctane solutions. This phase has not been observed as a major phase at all ranges of concentrations investigated and was observed as an intermediate form during the phase transformation from phase II to phase V. The formation of phase IV during this phase transformation is discussed below in the context of thermodynamics. In order to satisfy the monolayer symmetry of *p6* (Figure 3.8a), an aggregate must consist of four molecules (**A4**, Figure 3.1) to generate exclusively 3-fold rotation axes simultaneously by hydrogen bonding at two different positions in a unit cell (Figure 3.8b). In this case, the crystallographic asymmetric unit is two (*Z'*=2.0). Two molecules are related with 3-fold rotation axes and a 2-fold rotation axis, giving rise to *p6* symmetry. The appearance of *Z'* equal to 2.0 is also notable for its rarity (6.3 % in 2DSD).[14]

Hydrogen Bonding Motifs. The computed models for all phases provide the hydrogen bonding structures shown in Figure 3.10. Hydrogen bonding between amide groups plays a key role in creating complex features because all phases have different motifs. Phases I and II both contain amide dimers with local centers of symmetry; however in phase I these dimers are well separated due to the interdigitation of alkyl chains (phase I, Figure 3.10) whereas in phase II a continuous column of amides connected by additional hydrogen bonding is present (phase II, Figure 3.10). Although both phases could arise from **A1** aggregates, only phase I can form from **A2** aggregates due to solvation in heptanoic acid. (phase II, Figure 3.10). For phase III, two **18-amide** molecules act as connectors between aggregates consisting of 4 molecules (phase III, Figure 3.10). For the rhombic nanoporous network (phase V), there are 3- and 6-fold rotation axes formed by the hydrogen bonding network whereas for the honeycomb network (phase IV), an aggregate of 4 molecules generates exclusively 3-fold rotation

33

axes. For phase VI, the two different **A2** and **A5** modes are stabilized by forming hydrogen bonds as shown in Figure 3.10. The combination of these two modes causes a wave-like pattern of voids.

The observation of one-dimensional ordering (phase III) and high Z' values for three porous networks investigated here reveals that the simple amide amphiphile with C_s symmetry, which upon adsorption is unable to be coincident with any symmetry elements, has the ability to generate highly symmetric patterns by forming various aggregates using non-covalent interactions. The fact that all six phases have different hydrogen bonding motifs reveals that hydrogen bonding plays a critical role in not only forming aggregates but also in their stabilization. This is the key to form high symmetry or complex nanoscale features with high Z' using a low symmetry amide amphiphile. This finding has an analogy with trends in three-dimensional crystals, where $Z' > 1$ has been associated with strong non-covalent interactions.[42,45] In the present case, dilution also greatly contributes to stabilizing less dense forms through a thermodynamic mechanism.[34]

Thermodynamics. Molecular mechanics is a complementary tool to STM that provides not only structural information at the atomic level, sometimes obscured in the experimental images, but also thermodynamic information providing the relative stabilities of phases.[46] In the two most dense phases, the hydrogen bonding in phase II more significantly contributes to stabilizing the phase than in phase I based on evaluation of the electrostatic term (Table 3.2) and contributes to the overall greater predicted stability of phase II. However, a transformation from phase II to I was observed when adding heptanoic acid solution to the phenyloctane solution. In contrast, no phase transformation from phase I to II was observed by adding phenyloctane solution to the heptanoic acid solution. This result indicates that phase I is more stable than phase II. However, phase transformation from phase II to I in the homogeneous phenyloctane solution has not been observed within several hours. The plausible explanation for this is

34

that the formation of a non-hydrogen bonded aggregate before adsorption in phenyloctane requires overcoming a large energy barrier to transform to phase I. This experiment reveals that the substrate and solvent, which can affect adsorption energy of solutes and the solute-surface interaction,[28] also play a key role in stabilization of phases where the effects of the graphite substrate and solvent molecules are difficult to incorporate in the modeling.[47]

Consistent with the low densities of phases IV and V, the lattice energies are much more positive than the close-packed structures. Phase VI is less stable than the close-packed structures and much more stable than the other nanoporous structures. For phase VI, the density is smaller about 9 Da/nm^2 than that of phase I (229.5 Da/nm^2), and much higher than that of phase IV (86.0 Da/nm^2) and V (134.8 Da/nm^2) due primarily to smaller void size.[48] The computed model of phase VI indicates that the stabilization from electrostatic term of phase VI is smaller by 1.5 kcal/mol than that of phase I due to relatively low extent of hydrogen bonding.   For the other nanoporous networks, phase V is more stable than phase IV about 0.2 kcal/mol. Phase V is more stabilized by hydrogen bonding due to a relatively favorable arrangement around the 6-fold rotation axis (phase V, Figure 3.10) whereas such hydrogen bonding networks are not present in phase IV. Phase IV is more stabilized by van der Waals interaction due to the formation of an aggregate consisting of four molecules compared to the three molecules in phase V; in both cases close packing is only satisfied within the aggregate and therefore a smaller aggregate has a greater percentage of alkyl chains lacking full van der Waals contact. For these competing reasons, phase IV and V have similar lattice energies. However, the stabilization energy per unit area basis is a more appropriate measure of the relative stability of monolayers because only a fixed amount of surface area is available for monolayer formation.[49] The lattice energies are -4.3 kcal/nm^2 for phase V and -2.7 kcal/nm^2 for phase IV, indicating a greater stabilization for phase V due to higher density of non-covalent interactions. This molecular mechanics calculation supports that phase V

is a more thermodynamically stable form than phase IV, and indeed this is observed (vide infra). It must be noted that in cases where the concentration of adsorbate molecules is very low, a regime can be entered where insufficient molecules are available to cover the substrate completely. In such a case molar adsorption energy rather than energy on a per unit area basis may determine structure.

Comparison of close-packed and nanoporous structures provides additional insight regarding phase selection in 2D crystallization. For example, transformation from phase II to phase V is observed as the concentration decreases. Phase II has twice the density and is more stable by 10.7 kcal/mol than phase V based on computation. This large stability difference may be overcome by three factors proposed by De Feyter, Tobe, and co-workers: 1) substrate effects such as epitaxial stabilization by HOPG, 2) solvent coadsorption in periodically ordered voids providing additional weak interactions with adsorbed molecules, and 3) equilibrium of adsorption-desorption in solution.[34,41] The symmetry of phase IV and V are well matched with the symmetry of HOPG and furthermore mobile solvent molecules may exist in void space within 2D crystals thereby dramatically reducing the energy difference between phase II and V. In addition, the newly formed equilibrium of adsorption-desorption introduced by dilution can cause the phase transformation from the close-packed structure (phase II) to a less dense form (phase V). In order to experimentally verify whether or not phase V is a thermodynamic form, dilution of phenyloctane solution on HOPG was conducted. When 2.0 μL of the 50 μM solution was put on HOPG, the solution covered the entire HOPG surface (9 × 9 mm^2) and phase II was observed as a major phase. The sample solution was diluted by adding 1.0 μL phenyloctane aliquots to achieve a concentration of 20 μM while imaging the monolayer at each dilution step. At 33 μM, the phase transformation from phase II to phase V was observed and phase IV was observed as an intermediate during this transformation (Figure 3.11). In Figure 3.11a, the coexistence of phases II, IV and V is shown. After 100s, phase II transformed to phase IV and some of phase IV transformed

to phase V (blue oval in Figure 3.11b). After 250s, phase II and IV had completely transformed to phase V (Figure 3.11c). This result indicates that phase IV is an intermediate during the transformation to the thermodynamically stable form V under the newly formed equilibrium. Figure 3.11d shows a schematic illustration of symmetry change during the phase transformation observed in the blue oval. After desorption of phase II, the honeycomb network (phase IV) is formed because it is more kinetically favored than phase V and then one hexagonal pore is divided to three rhombic pores by reorganization, resulting in forming the rhombic network (phase V). Because phase V exists as a thermodynamically stable form in dilute solutions, phase IV, which has 36.2 % lower density than phase V, may be stabilized upon further dilution. Attempt to experimentally verify this possibility were not successful. Applying more dilute solutions led to formation of phase V accompanied by disordered regions suggesting that phase IV is only a kinetic form. (Figure 3.12).

The reverse transformation from phase V to phase II confirming the thermodynamic effect in phase selection as a function of concentration was also observed. After confirming the formation of phase V using 0.2 μL 10 μM, the concentration increased to 85 μM by adding 1 μL of 100 μM solution and phase II was observed as a major phase. (Figure 3.13)

Contrast to 3D Polymorphism. The observed behaviors regarding the phase transformation from phase II to phase V are similar to the phenomena of monotropy and enantiotropy in 3D polymorphism, where monotropy occurs when one polymorph is thermodynamically more stable than other polymorphs at all temperatures below melting and enantiotropy indicates that the relative thermodynamic stability of two forms reverses at some temperature. The present case shows analogous behavior of phase stability versus concentration rather than temperature (Figure 3.14) and can be described as a pycnotropism. Phase II and V show the enantiopycnotropic behavior because phase II transforms to phase V as the concentration decreases where coexistence with the mostly

same surface coverage was observed at 33 µM (Figure 3.15). Phase IV and phase V are monopycnotropic as shown in Figure 3.14b because phase V has been observed as an intermediate during the phase transformation and has not been observed as a thermodynamically stable form in all concentration ranges where 2D crystallization occurs. The Gibbs phase rule states that analogous thermodynamically driven phase transformations versus concentration can not be observed in 3D polymorphism whereas the phase transformation versus concentration is now being recognized as a general feature in 2D crystallization.   This discrepancy can be understood by recognizing that 2D crystals have additional contributions to phase selection due to the existence of HOPG and solvent and the relative influence of these changes with concentration. This observation is actually more similar to concentration-dependent formation of solvates in 3D crystallization and explains why alternative packing arrangements in two-dimensional crystallization should be termed pseudopolymorphs.

3.3 Conclusions

Studying the similarity and differences between two- and three-dimensional crystallization is essential to construct a bridge between them. This investigation demonstrates the ability of a simple amide amphiphile to exist in various ordered phases, even in the reduced dimensionality offered by adsorption to a surface, through adopting various aggregation modes. The combination of dilution and multiple hydrogen bonding motifs appears to favor the formation of $Z' > 1$ and there is analogy here to the suggestion that the absolute strength of non-covalent interactions can lead to forming $Z' > 1$ structures in three-dimensional crystallization. Furthermore, monopycnotropy and enantiopycnotropy are illuminated as thermodynamic descriptors for the emergent phenomenon of concentration-dependent changes in thermodynamic phase stability: a

phenomenon lacking analogy in polymorphic crystals. The particular system described presents for challenges for theory to explain the energetic relationships among forms and how kinetic factors can given rise to phase selection within the context of such a simple molecule assembled on a surface. From an experimental standpoint, such rich phase diversity has not previously been achieved and the design of molecules capable of adopting several energetically viable aggregation modes may be a model for future discovery efforts.

3.4 Experimental section

General experimental procedures for imaging and computation are described in Chapter 1.4.

3.5 References

(1)   López-Mejías, V.; Kampf, J. W.; Matzger, A. J. *J. Am. Chem. Soc.* **2009**, *131*, 4554-4555.

(2)   Vishweshwar, P.; McMahon, J. A.; Oliveira, M.; Peterson, M. L.; Zaworotko, M. J. *J. Am. Chem. Soc.* **2005**, *127*, 16802-16803.

(3)   Vrcelj, R. M.; Sherwood, J. N.; Kennedy, A. R.; Gallagher, H. G.; Gelbrich, T. *Cryst. Growth Des.* **2003**, *3*, 1027-1032.

(4)   van der Heijden, A.; Bouma, R. H. B. *Cryst. Growth Des.* **2004**, *4*, 999-1007.

(5)   Nalwa, H. S.; Saito, T.; Kakuta, A.; Iwayanagi, T. *J. Phys. Chem.* **1993**, *97*, 10515-10517.

(6)   Kwon, O. P.; Jazbinsek, M.; Yun, H.; Seo, J. I.; Kim, E. M.; Lee, Y. S.; Gunter, P. *Cryst. Growth Des.* **2008**, *8*, 4021-4025.

(7)   Li, S. S.; Yan, H. J.; Wan, L. J.; Yang, H. B.; Northrop, B. H.; Stang, P. J. *J. Am. Chem. Soc.* **2007**, *129*, 9268-9269.

(8)   Zhou, H.; Dang, H.; Yi, J. H.; Nanci, A.; Rochefort, A.; Wuest, J. D. *J. Am. Chem. Soc.* **2007**, *129*, 13774-13775.

(9)   Scherer, L. J.; Merz, L.; Constable, E. C.; Housecroft, C. E.; Neuburger, M.; Hermann, B. A. *J. Am. Chem. Soc.* **2005**, *127*, 4033-4041.

(10)   Fang, H. B.; Giancarlo, L. C.; Flynn, G. W. *J. Phys. Chem. B* **1999**, *103*, 5712-5715.

(11)   Day, G. M.; Trask, A. V.; Motherwell, W. D. S.; Jones, W. *Chem. Commun.* **2006**, 54-56.

(12)   Rafilovich, M.; Bernstein, J. *J. Am. Chem. Soc.* **2006**, *128*, 12185-12191.

(13)   Lou, B. Y.; Bostroem, D.; Velaga, S. P. *Cryst. Growth Des.* **2009**, *9*, 1254-1257.

(14)   The Two-Dimensional Structural Database (2DSD), a catalog of two-dimensional crystals formed at liquid/solid interfaces, reveals there is no compound showing ability to exist in over five different phases: Plass, K. E.; Grzesiak, A. L.; Matzger, A. J. *Acc. Chem. Res.* **2007**, *40*, 287-293.

(15)   Chen, S.; Guzei, I. A.; Yu, L. *J. Am. Chem. Soc.* **2005**, *127*, 9881-9885.

(16)   Nangia, A. *Models, Mysteries, and Magic of Molecules* (Ed.: Boeyens, J. C. A.; Ogilvie, J. F.), Springer, Dordrecht, **2008**, pp. 63-86.

(17)   Rodríguez-Spong, B.; Price, C. P.; Jayasankar, A.; Matzger, A. J.; Rodríguez-Hornedo, N. *Adv. Drug Delivery Rev.* **2004**, *56*, 241-274.

(18)   Mitchell, C. A.; Yu, L.; Ward, M. D. *J. Am. Chem. Soc.* **2001**, *123*, 10830-10839.

(19)   Hiremath, R.; Basile, J. A.; Varney, S. W.; Swift, J. A. *J. Am. Chem. Soc.* **2005**, *127*, 18321-18327.

(20)   Hiremath, R.; Varney, S. W.; Swift, J. A. *Chem. Commun.* **2004**, 2676-2677.

(21)   Friščić, T.; MacGillivray, L. R. *Chem. Commun.* **2009**, 773-775.

(22)   Braga, D.; Cojazzi, G.; Paolucci, D..; Grepioni, F. *CrystEngComm* **2001**, *38*, 1-3.

(23)   Miura, H.; Ushio, T.; Nagai, K.; Fujimoto, D.; Lepp, Z.; Takahashi, H.; Tamura, R. *Cryst. Growth Des.* **2003**, *3*, 959-965.

(24)   Price, C. P.; Grzesiak, A. L.; Matzger, A. J. *J. Am. Chem. Soc.* **2005**, *127*, 5512-5517.

(25)   Weissbuch, I.; Addadi, L.; Lahav, M.; Leiserowitz, L. *Science* **1991**, *253*, 637-645.

(26)   Thallapally, P. K.; Jetti, R. K. R.; Katz, A. K.; Carrell, H. L.; Singh, K.; Lahiri, K.; Kotha, S.; Boese, R.; Desiraju, G. R. *Angew. Chem., Int. Ed.* **2004**, *43*, 1149-1155.

(27)   He, X. R.; Stowell, J. G.; Morris, K. R.; Pfeiffer, R. R.; Li, H.; Stahly, G. P.; Byrn, S. R. *Cryst. Growth Des.* **2001**, *1*, 305-312.

(28)   Venkataraman, B.; Breen, J. J.; Flynn, G. W. *J. Phys. Chem.* **1995**, *99*, 6608-6619.

(29)   Tahara, K.; Furukawa, S.; Uji-I, H.; Uchino, T.; Ichikawa, T.; Zhang, J.; Mamdouh, W.; Sonoda, M.; De Schryver, F. C.; De Feyter, S.; Tobe, Y. *J. Am. Chem. Soc.* **2006**, *128*, 16613-16625.

(30)   Gutzler, R.; Lappe, S.; Mahata, K.; Schmittel, M.; Heckl, W. M.; Lackinger, M. *Chem. Commun.* **2009**, 680-682.

(31)   Lackinger, M.; Griessl, S.; Heckl, W. A.; Hietschold, M.; Flynn, G. W. *Langmuir* **2005**, *21*, 4984-4988.

(32)   Mamdouh, W.; Uji-i, H.; Ladislaw, J. S.; Dulcey, A. E.; Percec, V.; De Schryver, F. C.; De Feyter, S. *J. Am. Chem. Soc.* **2006**, *128*, 317-325.

(33)   Li, Y. B.; Ma, Z.; Qi, G. C.; Yang, Y. L.; Zeng, Q. D.; Fan, X. L.; Wang, C.; Huang, W. *J. Phys. Chem. C* **2008**, *112*, 8649-8653.

(34)   Lei, S. B.; Tahara, K.; De Schryver, F. C.; Van der Auweraer, M.; Tobe, Y.; De Feyter, S. *Angew. Chem., Int. Ed.* **2008**, *47*, 2964-2968.

(35)   Brock, C. P.; Dunitz, J. D. *Chem. Mater.* **1994**, *6*, 1118-1127.

(36)   Ahn, S.; Morrison, C. N.; Matzger, A. J. *J. Am. Chem. Soc.* **2009**, *131*, 7946-7947.

(37)   Ahn, S.; Matzger, A. J. *J. Am. Chem. Soc.* **2009**, *131*, 13826-13832.

(38)   Parveen, S.; Davey, R. J.; Dent, G.; Pritchard, R. G. *Chem. Commun.* **2005**, 1531-1533.

(39)   Tahara, K.; Lei, S.; Mossinger, D.; Kozuma, H.; Inukai, K.; Van der Auweraer, M.; De Schryver, F. C.; Hoger, S.; Tobe, Y.; De Feyter, S. *Chem. Commun.* **2008**, 3897-3899.

(40)   Kampschulte, L.; Werblowsky, T. L.; Kishore, R. S. K.; Schmittel, M.; Heckl, W. M.; Lackinger, M. *J. Am. Chem. Soc.* **2008**, *130*, 8502-8507.

(41)   Tahara, K.; Okuhata, S.; Adisoejoso, J.; Lei, S.; Fujita, T.; De Feyter, S.; Tobe, Y. *J. Am. Chem. Soc.* **2009**, *131*, 17583-17590.

(42)   Plass, K. E.; Kim, K.; Matzger, A. J. *J. Am. Chem. Soc.* **2004**, *126*, 9042-9053.

(43)   De Feyter, S.; Grim, P. C. M.; van Esch, J.; Kellogg, R. M.; Feringa, B. L.; De Schryver, F. C. *J. Phys. Chem. B* **1998**, *102*, 8981-8987.

(44)   Steiner, T. *Acta Crystallogr., Sect. B*, **2000**, *56*, 673-676.

(45)   Anderson, K. M.; Goeta, A. E.; Hancock, K. S. B.; Steed, J. W. *Chem. Commun.* **2006**, 2138-2140.

(46)   The phase III was not considered to compare stabilities of phases due to the one-dimensional ordering which makes construction of a unique model impossible.

(47)   The doubly periodic and noncommensurate relationship between the substrate and overlayer prohibits constructing the periodic model with substrate. In addition, solvent-molecule interactions with fully periodic 2D crystals are not feasible using experimental data because the solvent molecules are too fleeting to allow STM imaging.

(48)   The densities were obtained by multiplication of the molecular weight (Da) by the number of molecules in the unit cell, followed by division by the surface area in square nanometers (nm^2).

(49)   Kim, K.; Plass, K. E.; Matzger, A. J. *J. Am. Chem. Soc.* **2005**, *127*, 4879-4887.

18-amide

A 1   **A 2**

A 3   **A 4**   **A 5**
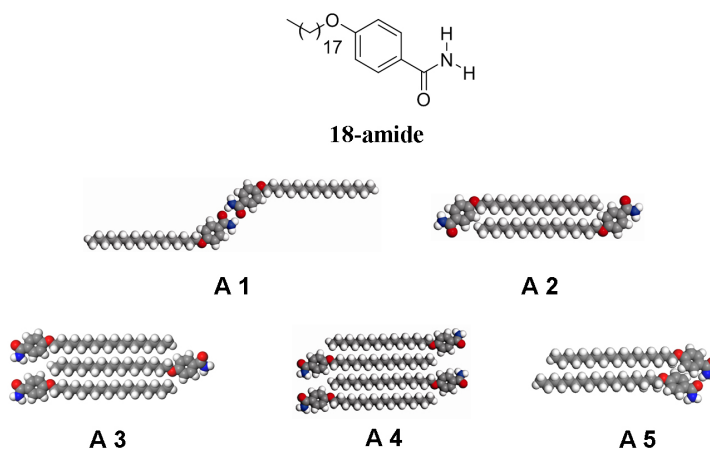
Figure 3.1. Molecular structures investigated and possible aggregation modes of **18-amide**.

phase		plane group	Z′
I		*p2*	1.0
II		*p2*	1.0
III		-	-
IV		*p6*	2.0
V		*p6*	3.0
VI		*p1*	6.0

Figure 3.2. Schematic representation of all phases observed in 2D crystals of **18-amide** with unit cells. The numbers of molecules in the asymmetric unit (*Z′* values) are indicated.

Table 3.1. Experimental and Computed Unit Cell Parameters for All Two-Dimensionally Ordered Phases Observed of **18-amide**.

phase	computed			experimental			density (Da/nm^2)
	a (Å)	b (Å)	α (deg)	a (Å)	b (Å)	α (deg)	
I	37.8	9.15	101	38.3±0.3	9.8±0.3	102±2	229.5
II	63.1	5.1	111	67.8±1.1	5.1±0.1	117±1	259.4
IV	78.5	78.3	120	77.2±1.9	77.0±2.0	120±1	86.0
V	77.5	77.5	120	80.1±0.4	80.0±0.4	120±1	134.8
VI	34.8	37.6	126	37.4±2.0	40.0±2.0	128±2	220.8
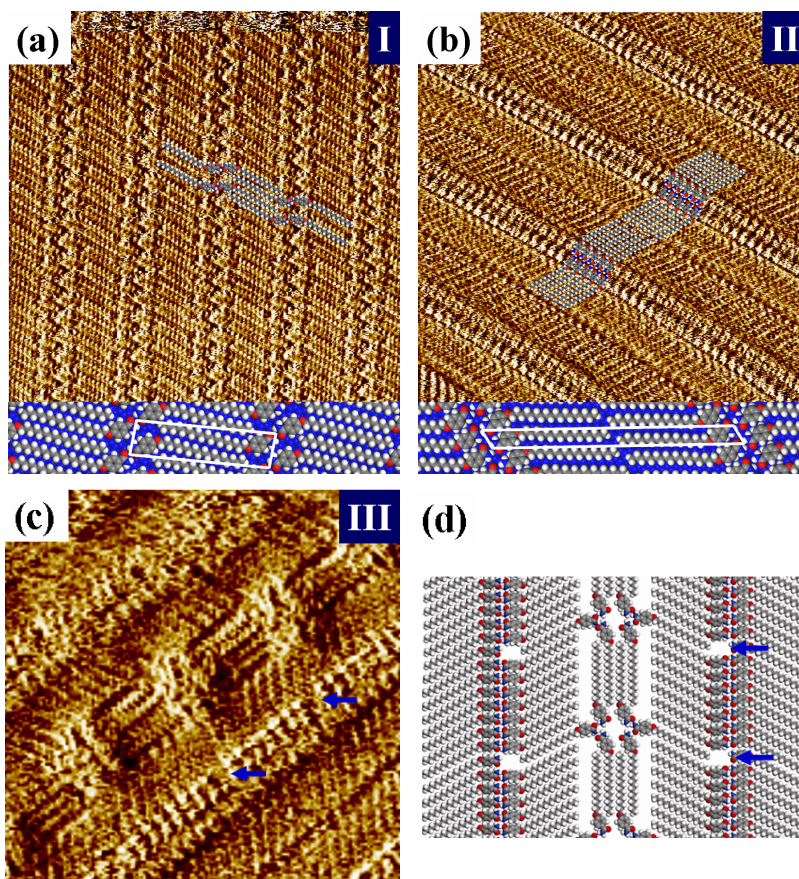
Figure 3.3. Three different close packed structures of **18-amide** formed at the liquid/HOPG interface. (a) STM image (20 × 20 nm^2) and the computed model of the monolayer in 1.0 mM heptanoic acid solution. (b) STM images (20 × 20 nm^2) and the computed model of the major phase in 100 μM phenyloctane solution. (c) STM images (15 × 15 nm^2) and (d) the computed model of a minor phase in 100 μM phenyloctane solution. The computed models are superimposed on STM images. Blue arrows indicate vacancies in the columnar packing.
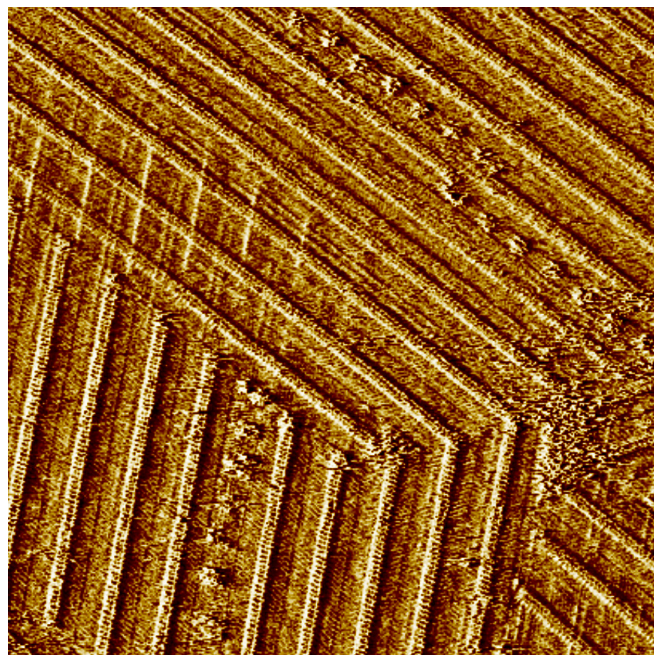
Figure 3.4. STM image (80×80 nm^2) of phase III as a minor phase.
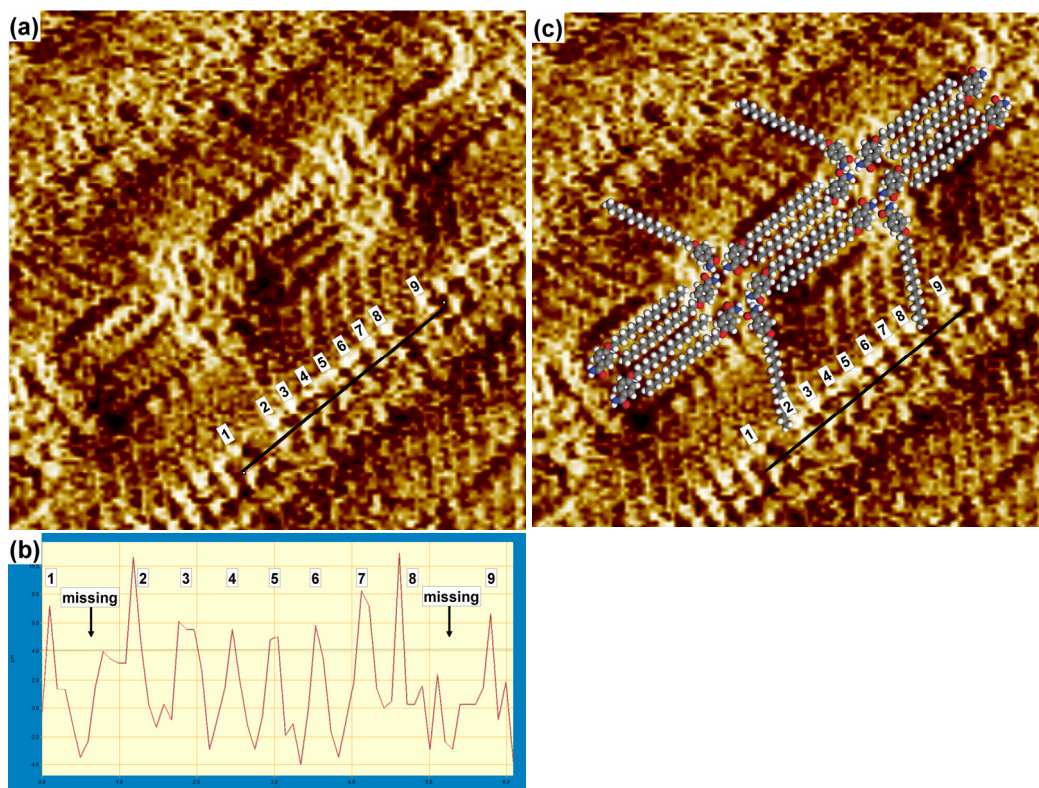
Figure 3.5. (a) STM image (12×12 nm^2) of phase III, (b) the height profile showing the vacancies of aromatic rings in the phase-II-type column and (c) STM image overlaid with the computed model of phase III.
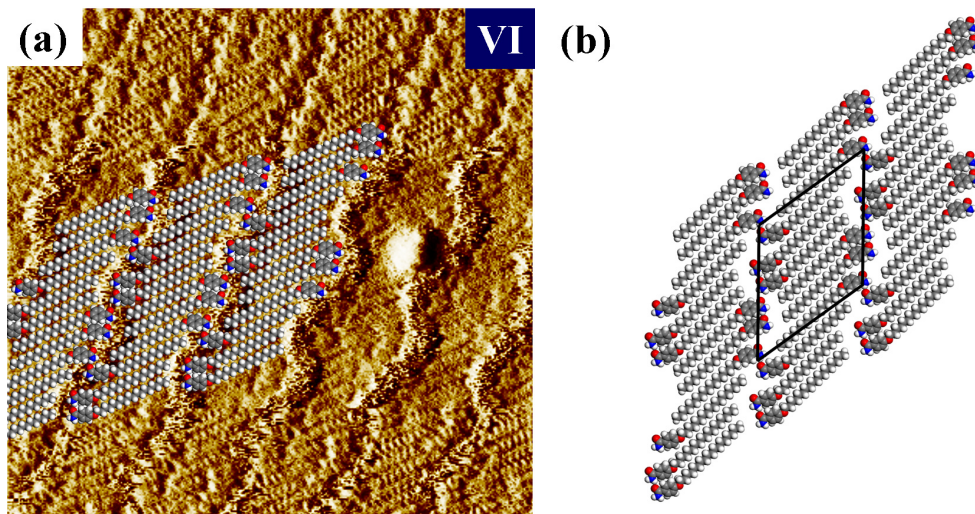
Figure 3.6. The porous structure from dilute heptanoic acid solutions. (a)   STM image (20×20 nm^2) obtained from 500 µM solution and (b) the computed model of phase VI. The wavy boundaries between columns in the STM image originate from the void space of phase VI.
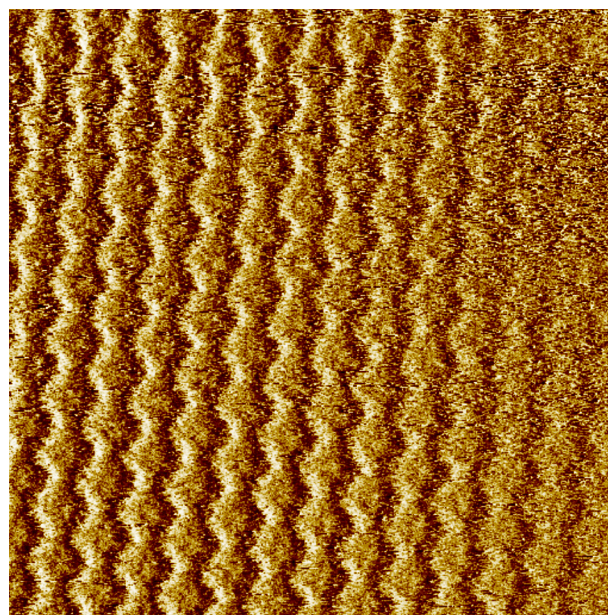
Figure 3.7. STM image (50×50 nm^2) of phase VI showing a wave-like pattern of voids.
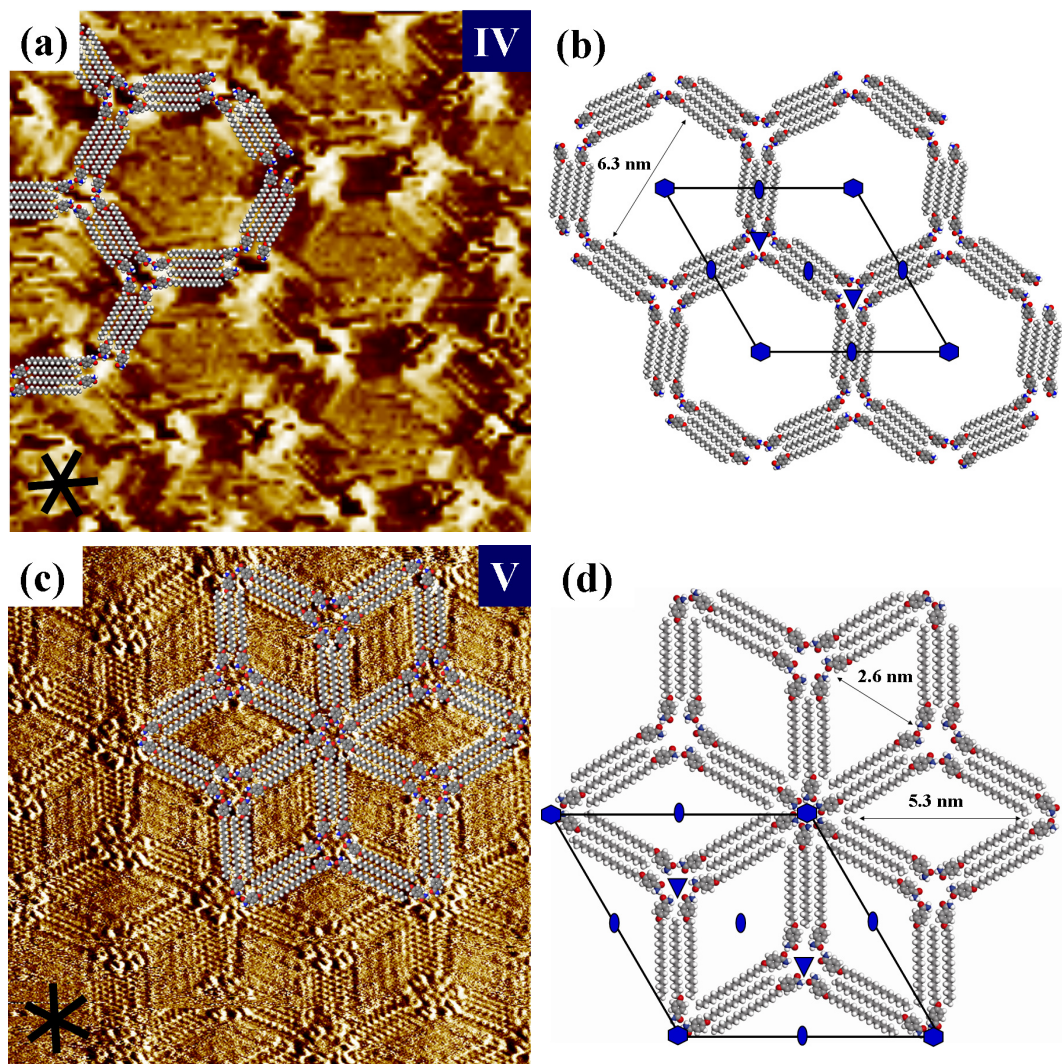
Figure 3.8. Two different nanoporous structures from dilute phenyloctane solutions. (a) STM image (20×20 nm^2) and (b) the computed model of the honeycomb network from 33 μM phenyloctane solution. (c) STM image (20×20 nm^2) and (d) the computed model of the rhombic nanoporous network from 25 μM phenyloctane solution. The black axes indicate the main symmetry of HOPG under the monolayer. The computed models are superimposed on STM images.
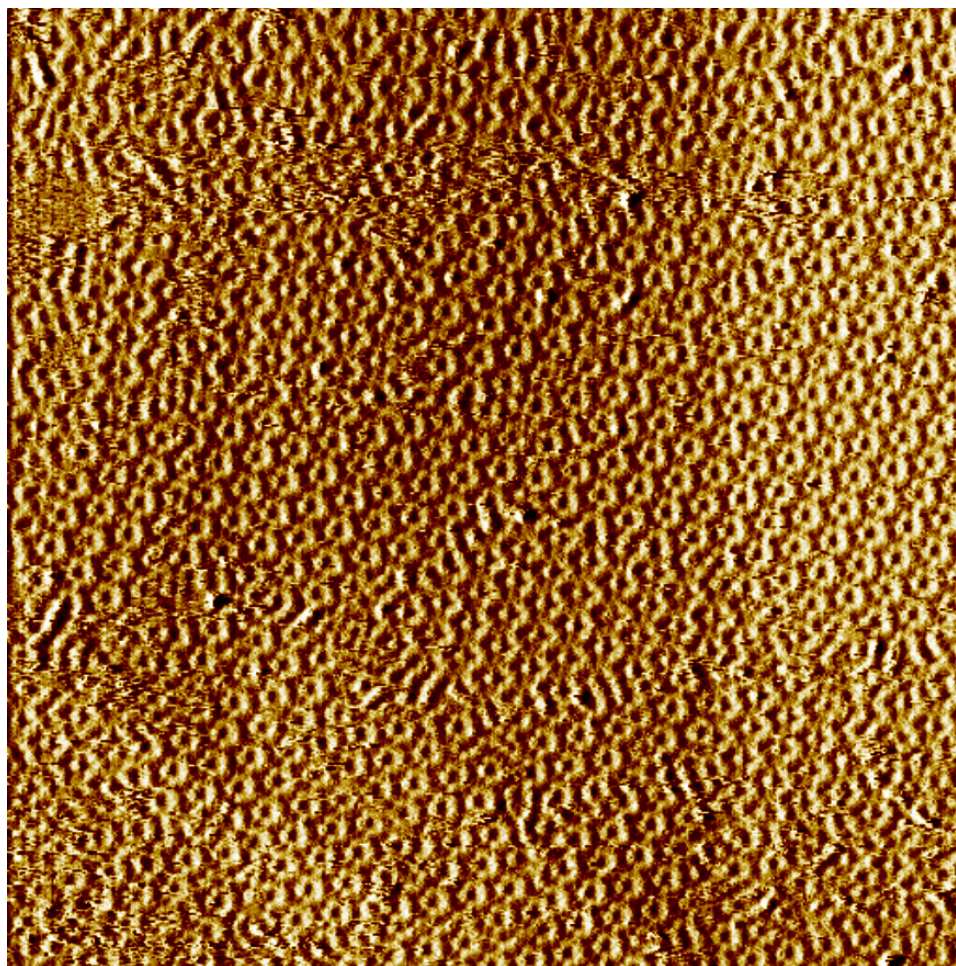
Figure 3.9. STM image (200 × 200 nm^2) of phase V at 10 μM.
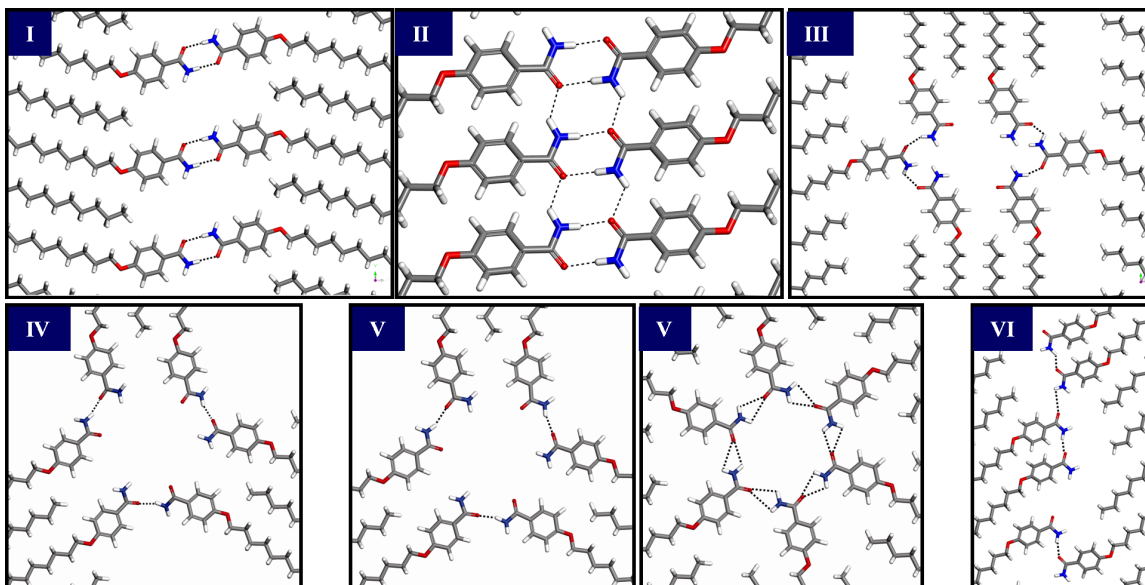
Figure 3.10. The hydrogen bonding networks observed in six phases. Hydrogen bonds are indicated by a dotted line. Phase V has two different networks to generate 3- and 6-fold rotation axes.

Table 3.2. Lattice Energies of All Two-Dimensionally Ordered Phases of **18-amide** Computed by the COMPASS Force Field (kcal/mol)[a].

phase	I	II	IV	V	VI
lattice energy	-17.5	-23.0	-12.1	-12.3	-15.8
van der Waals term	-12.3	-13.6	-9.4	-9.0	-12.1
electrostatic term	-5.2	-9.4	-2.7	-3.3	-3.7

[a] These values represent the energy obtained by the formation of the 2D crystals from isolated **18-amide** molecules.
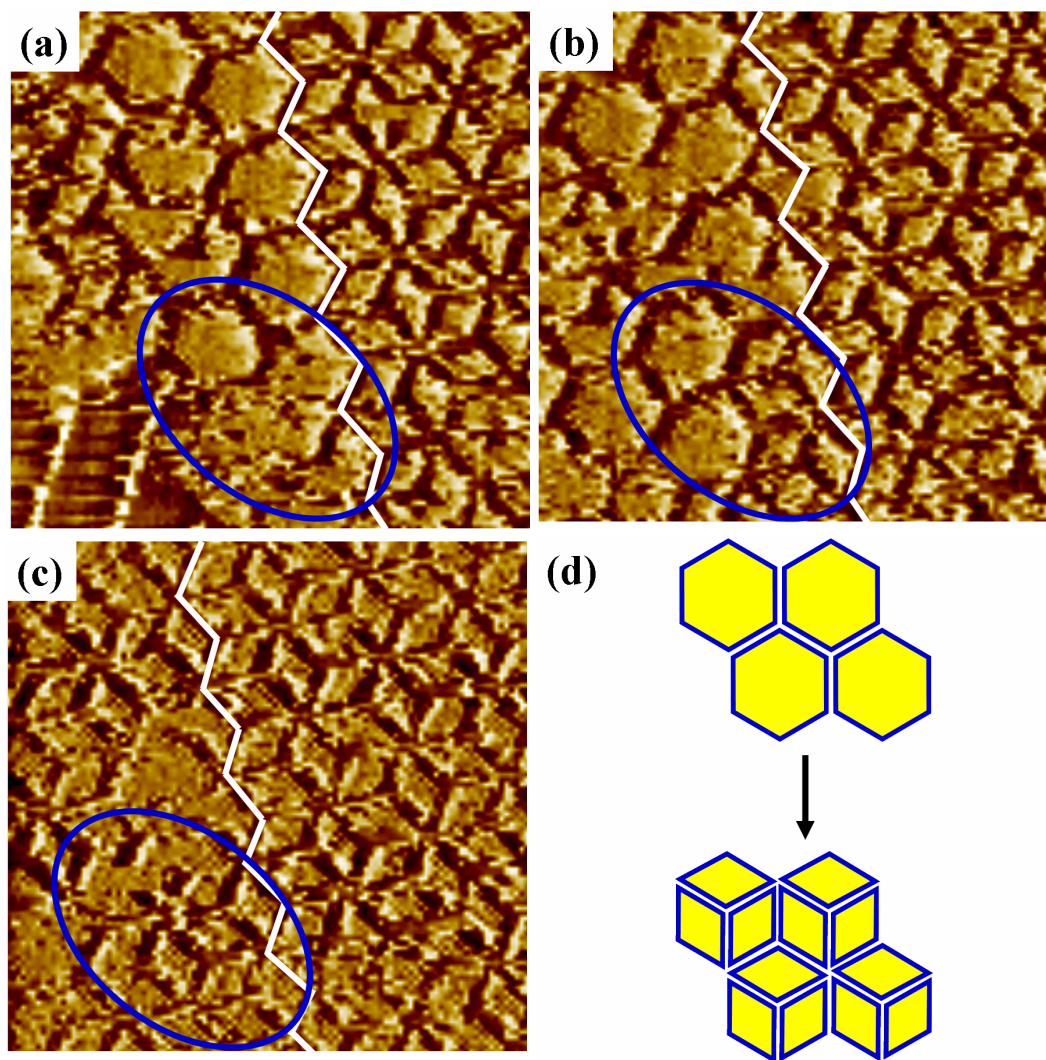
Figure 3.11. Sequential STM images (40×40 nm^2) obtained from a 33 μM **18-amide** in phenyloctane solution on HOPG. These images clearly show the phase transformation from phase II to phase V where phase IV was observed as an intermediate. (a) Coexistence of phase II, IV, and V was observed (t = 0) and a white zigzag line is designated to distinguish phase IV and V. (b) After 100 s, phase II transforms to phase IV and some of the hexagonal pores transform to the rhombic pore (blue oval). (c) After 250 s, phase IV transforms to phase V. (d) Schematic illustration of the transformation from the hexagonal pore to the rhombic pore observed in the blue oval.
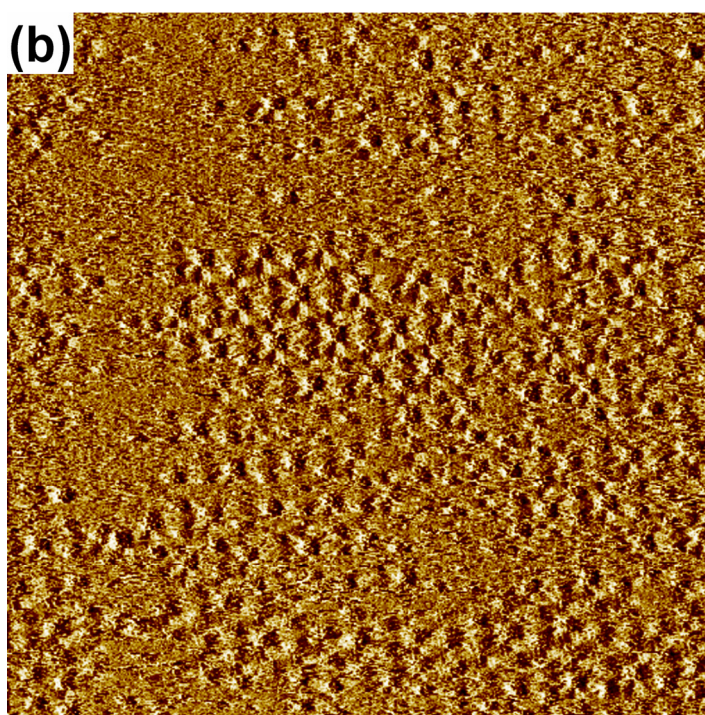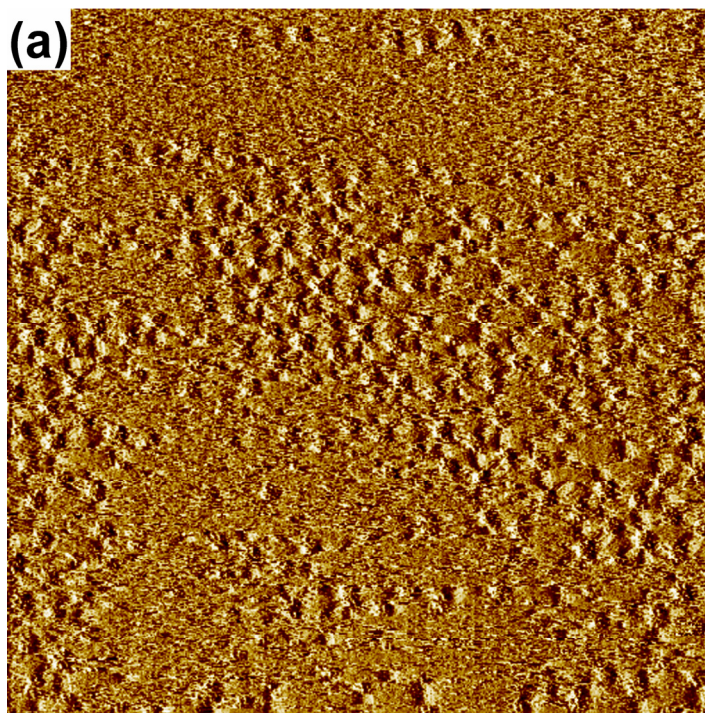
Figure 3.12. STM images (100×100 nm^2) of 5 μM of (a) 0 sec and (b) 50 sec.
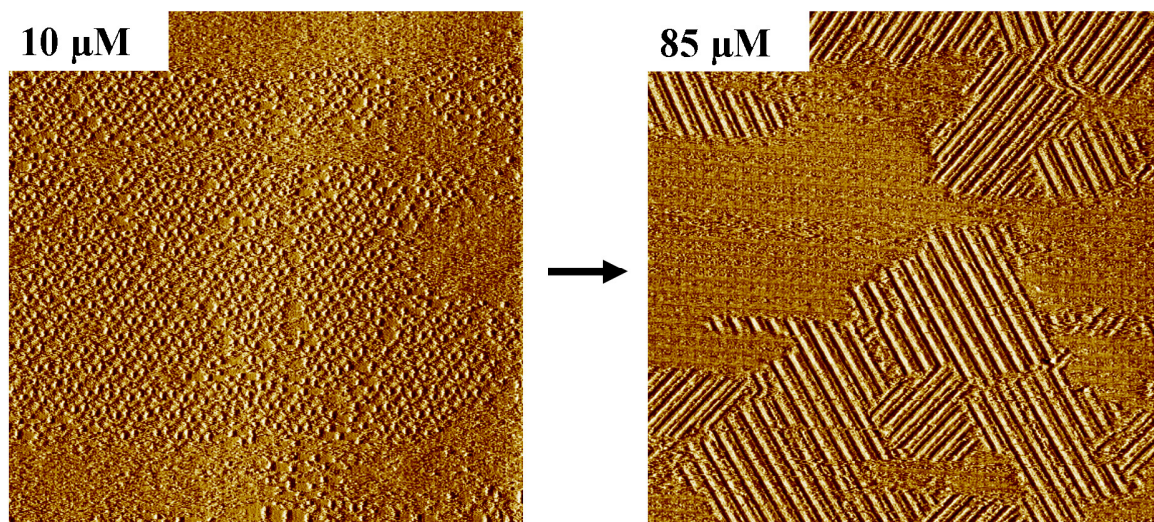
Figure 3.13. STM images (200 × 200 nm^2) showing the phase transformation from phase V to phase II by increasing the concentration from 10 µM to 85 µM.
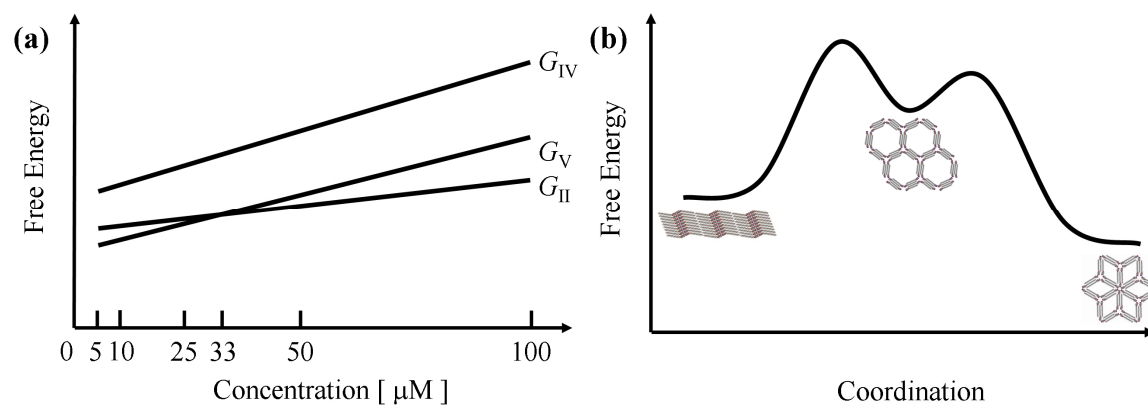
Figure 3.14. Schematic diagram of free energy versus concentration of phase II, IV, and V at a given temperature during two-dimensional crystallization: (a) schematic illustration of monopycnotropy and enantiopycnotropy for phase II, IV and V of **18-amide** and (b) Reaction coordination diagram describing the phase transformation from phase II to phase V below 33 µM where phase IV is observed as an intermediate.
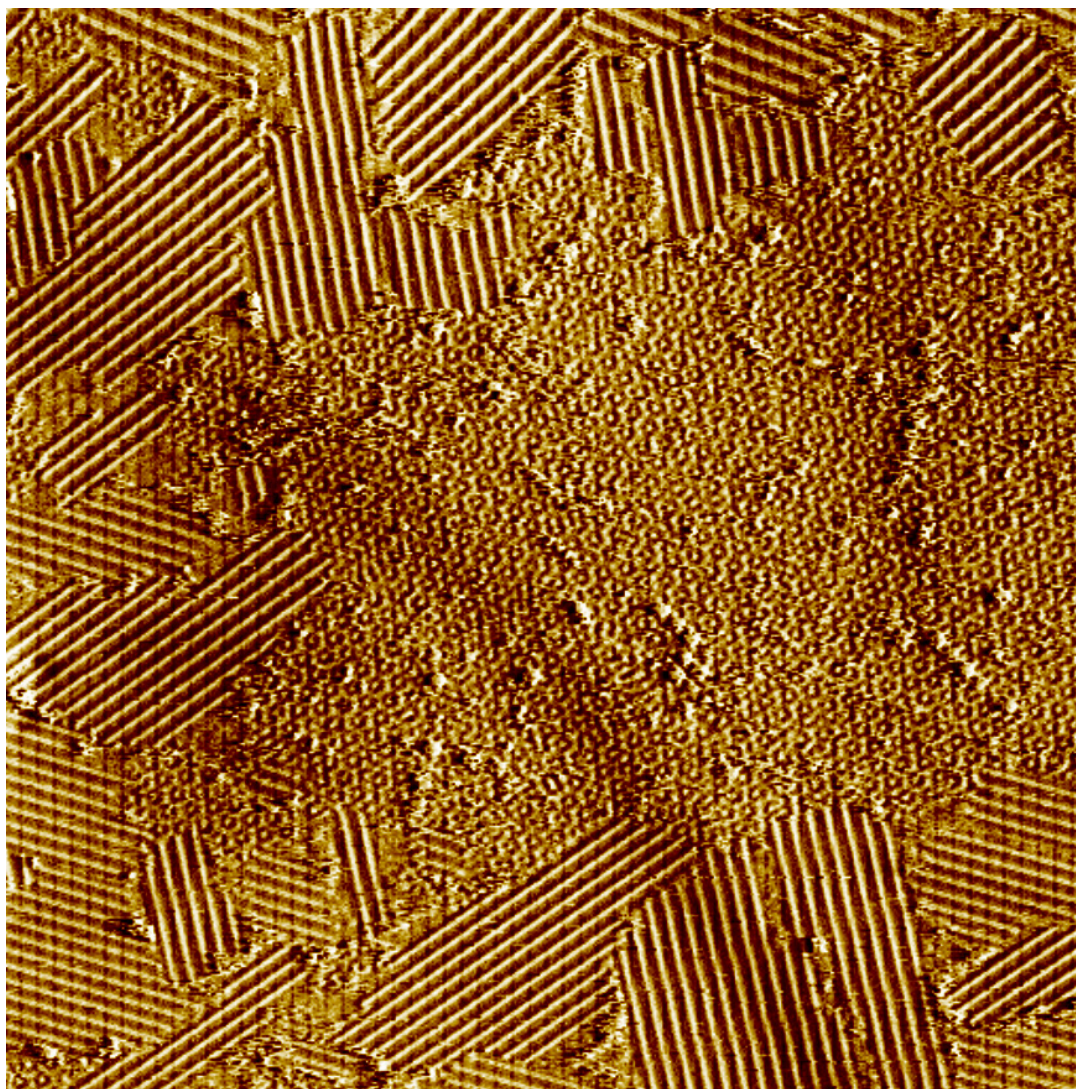
Figure 3.15. STM image (400 × 400 nm^2) of 33 μM solution showing coexistence of phase II and V.

CHAPTER 4

Additive Control over Molecular Assembly in Two-Dimensional Crystals

4.1 Introduction

Crystal polymorphism, because of its importance across a wide range of fields in solid-state chemistry such as pharmaceuticals,[1,2] explosives, [3,4] and nonlinear optical materials, [5,6] is of considerable economic interest; furthermore because of the unresolved challenges associated with predicting the occurrence of this phenomenon and reducing to practice experimentally, it is one of the greatest scientific challenges. In general, polymorphs are discovered through crystallization by screening methods varying solvent/temperature[7] although more modern discovery methods such as tailor-made additives,[8-10] epitaxial crystal growth,[11-13] and polymer-induced heteronucleation[14] are entering the toolbox of the solid-state researcher. Recently, the discovery of new metastable polymorphs during attempts to grow cocrystals has been reported and this phenomenon may be distinguished from previous methods of polymorph discovery. [15-18] For example, an impressive four polymorphs of benzidine were obtained in an attempted cocrystallization with benzophenone or diphenyl sulfoxide.[16] The generation of metastable polymorphs during cocrystallization trials may prove to be a useful crystal form discovery technique contributing to the important goal of accessing all energetically viable polymorphs of a given compound; however at the present time the mechanism of form production is unclear making the path toward further developments uncertain. Because reduced dimensionality dramatically simplifies the system, studying phase selection in two-dimensional (2D) crystallization at solution/solid interfaces can provide

mechanistic insights at the molecular level. In this chapter, it is demonstrated that the phase selection occurs through the competition study with an additive in 2D crystallization in an attempted co-adsorption of a simple amide amphiphile capable of forming multiple phases and an additive. The mechanistic insights are drawn at the molecular level using scanning tunneling microscope (STM), offering submolecular resolution of both periodic and non-periodic packing in a time dependent fashion[19-28] and interpreted in the context of kinetics and thermodynamics.

4.2 Results and Discussion

To explore the effect of additives on phase selection in 2D crystals, an amide amphiphile with 18 carbons in the alkyl chain (**18-amide**) was selected for study because it has been characterized to form at least six phases.[29] The chemical structures of **18-amide** and the additive molecules investigated are shown in Figure 4.1. A concentration of 100 µM total adsorbate was used for each binary mixture with the molar ratio varied as specified. All STM imaging was performed at the phenyloctane/highly oriented pyrolytic graphite (HOPG) interface. During this investigation, new crystallization behaviors, distinguished with those from the homogeneous solutions of **18-amide**, were observed and in some cases the results are kinetic in nature whereas for others the presence of an additive exerts a thermodynamic influence. The implications of these results for understanding additive effects on three-dimensional (3D) polymorph selection are discussed in this context.

18-amide vs. 17-*m*-diester. As a baseline for understanding additive effects, the case of **18-amide** with **17-*m*-diester** is discussed. At high concentrations of the amide, a pure close packed phase (Figure 4.2, Phase I) is observed. The rhombic nanoporous network of **18-amide** (Figure 4.2, phase II) was observed from 1:3 to 1:11 (**18-amide**:**17-*m*-diester**) whereas the coadsorption occurred from 1:11 to 1:20 to form 1D-cocrystals.[28]

These molecular assemblies showed a marked dependence on the relative mole fraction of two components in solution. The structural characteristics of these phases have been discussed previously.[28-30] In particular, coexistence of phase II of **18-amide** and the 1D-cocrystal without phase transformation was observed at 1:11 (Figure 4.2b) indicating that competitive adsorption occurs near this molar ratio so that the formation of phase II of **18-amide** may be influenced by molecular interaction with **17-*m*-diester**. However, the above data are consistent with the a simple dilution effect, which has been shown to stabilize phase II in a homogeneous **18-amide** solution.[29] To test this hypothesis, the concentration of **18-amide** in the mixture was varied while keeping the molar ratio to the additive constant. Using 53 μM **18-amide** and 460 μM **17-*m*-diester**, the concentration of **18-amide** is above the stability crossing point between phase I and II observed in homogeneous solution (33 μM).[29] Under these conditions, phase II was not observed and some disorder, which may be kinetically induced by competition, was observed (Figure 4.2c). However, at 10 μM **18-amide** and 90 μM **17-*m*-diester**, phase II was observed as the thermodynamically stable form (Figure 4.2d). This competition study with **17-*m*-diester** does not illuminate new thermodynamic behavior based on the presence of an additive although molecular competition exerts some influence on kinetics.

18-amide vs. 17-triester. A highly disordered assembly of **18-amide** domanins was observed from 2:1 (**18-amide**:**17-triester**) without discernible co-adsorption with **17-triester** (Figure 4.3a) whereas coadsorption with phase segregation between the disordered assembly of **18-amide** and **17-triester** phase was observed at the 1:1 ratio (Figure 4.3b). Because this disordered structure has not been observed in other conditions such as dilute solutions of **18-amide**,[29] amide amphiphile analogues with shorter alkyl chains,[30] and the mixture with other additives in the present study, the disordered assembly is induced from molecular interaction between **18-amide** and **17-triester** and furthermore is a kinetic product. This latter claim is supported by the observation of the transformation from disordered structures to ordered structures by sequential STM

images (Figure 4.4). The disordered structure observed at a 1:1 ratio reorganizes to form more ordered structures indicated by white arrows in Figure 4.4a: a type of Ostwald ripening.[31] With further increase of the **17-triester** fraction, the disordered structures of **18-amide** were transformed to **17-triester** phase (Figure 4.4b). In this case, the dilution is unlikely to significantly affect crystallization because the concentration of **18-amide** in the present case is greater than 33 μM, the stability crossover point between phase I and II in homogeneous solution. In the previous study, it has been demonstrated that **18-amide** has ability forming and stabilizing various aggregates through noncovalent interactions and when two different aggregates are incorporated in a unit cell, highly complex features such as one-dimensional order and wave-like patterns of voids are formed.[29] The same phenomenon manifests in the present case because the existence of various aggregates in the disordered assembly is observed while maintaining reasonably close packing due to compatibility of aggregates. In other words this compatibility between various aggregates makes disorder possible to observe because the thermodynamic penalty is not great.

18-amide vs. 12-amide. During 2D crystal growth of **18-amide** in the presence of **12-amide**, the formation of the honeycomb network (phase III) and the rhombic nanoporous networks (phase II) of **18-amide** were observed at ratios from 1:3 to 1:7 (**18-amide**:**12-amide**) (Figure 4.5) whereas the rhombic nanoporous networks of **12-amide** was observed at a ratio of 1:9. The present case differs from 2D crystallization from **18-amide** homogeneous solutions in two ways: (1) The phase III of **18-amide** obtained in the presence of additive was observed as a major phase with over 95% surface coverage whereas the surface coverage by phase III in homogeneous solutions was less than 10%,[29] and (2) the phase transformation rate from phase III to II dramatically decreased in the two component system compared with that observed in homogeneous solutions. The phase transformation rate was obtained by counting the number of molecules (N) associated with each phase in successive STM images. To eliminate the concentration

effect on the rate, the concentration of **18-amide** for both the mixture and the homogeneous solution were fixed at 25 µM. Because the phase transformation occurred most rapidly in the scanned area, the scanning parameters such as current, bias, and scanning rate were fixed and the average of the rates obtained by STM imaging with different tips was used to minimize tip artifacts. The obtained values of ln(N)/sec were -0.031±0.007 for the diluted homogenenous solution and -0.0034±0.0012 for the mixture (Figure 4.5c). This 10-fold difference is consistent with an increase in activation energy required to transform from phase III to II in the presence of additive. Using the Arrhenius equation, the change of the energy barrier (ΔE_a) associated with this transformation can be estimated as 1.33±0.36 kcal/mol.[32,33] This increase of energy barrier (E_a) can be achieved by either destabilization of the transition state between phase III and II (kinetic mechanism) or stabilization of phase III (thermodynamic mechanism). Although kinetic factors often explain the formation of a metastable form during crystallization with additives in 3D crystallization, the thermodynamic stabilization of a metastable form is generally not possible because in a pure phase additive can only interact with the surface of the crystals and this exerts a negligible effect on stability. The differentiation between these possibilities in 2D could be achieved by comparing STM images obtained during the phase transformation in homogeneous solution and the mixture (Figure 4.6). In the homogeneous solution of 25 µM **18-amide**, because phase III is kinetically formed after desorption of a part of phase I and rapidly transformed to phase II, phase I and II exist as major phases at as shown in Figure 4.6a. In contrast, phase I was not observed in the mixture of **18-amide** and **12-amide** as shown in Figure 4.6c whereas phase III exists as a major phase. This observation can not be explained by the kinetic pathway. In that case phase I should be observed as one of the major phases because phase I remains more stable than phase III. However, the observed phenomenon suggests that phase III is more stable than phase I. To verify this thermodynamic stabilization pathway, 0.5 µL of 100 µM of **18-amide** was placed on HOPG. After confirming the formation of phase I by

STM, 1.5 µL of 100 µM of **12-amide** was added to the sample solution on HOPG to make a 1:3 mixture that is 25 µM in **18-amide**. The phase transformation from phase I to III occurred as shown in Figure 4.7. This result indicates that phase III is more stable than phase I under these conditions, a result of combining dilution effects and a thermodynamic stabilization of phase III by **12-amide** molecules. Thermodynamic stabilization of a nanoporous network in 2D crystallization can occur by three general pathways: (1) epitaxial stabilization by due to substrate, (2) equilibrium of adsorption-desorption (dilution), and (3) solvent coadsorption.[34,35] The constancy of the substrate and concentration employed points to the role of **12-amide** molecules as stabilizers of phase III through a coadsorption mechanism; such interaction with the pores must be more favorable than interaction of adsorbed **18-amide** molecules with solvent. The failure to image coadsorbed **12-amide** molecules must be related to their high mobility. Therefore, the high surface coverage of phase III and the transformation rate decrease from phase III to II in the mixture can only be rationalized by the thermodynamic stabilization of phase III by **12-amide** molecules.

Implications. The above three cases clearly show that an additive can kinetically and thermodynamically affect the 2D crystallization of **18-amide** (Figure 4.8). From these competition studies, three major factors in the 2D phase selection in from multicomponent solutions were observed. First, the mole fraction of components plays a critical role, in concert with the free energy of monolayer formation, in determining which phase adsorbs at equilibrium (Figure 4.9). Thus, when an additive has much more negative free energy than the other compound, even small amount of an additive can affect the crystallization of the other compound. Second, as shown in the competition with **17-*m*-diester**, the dilution effect in the multicomponent solution serves as a key thermodynamic factor in 2D crystallization. Third, the additive structure plays a critical role in determining the 2D crystal structure through a kinetic or thermodynamic

contribution. This fact indicates that not only assembly structure but also stabilization of a metastable form can be controlled through modification of additive structure.

The above 2D phenomena involving competitive molecular adsorption offers a mechanism for changes the course of phase selection from multicomponent solutions in 3D crystallization. Heterogeneous nucleation is a ubiquitous phenomenon in 3D crystallization and therefore the structure of adlayers such as physisorbed monolayers may kinetically drive the outcome of crystallization. The above examples illustrate that monolayer structure can be altered both through kinetic and thermodynamic pathways; inasmuch as such structures can exert kinetic influence over phase selection in 3D crystallization through a heteronucleation mechanism this offers one pathway for additive-induced polymorph formation in 3D crystallization.

4.3 Conclusions

It has been demonstrated that an analogous phenomenon of additive-induced phase selection reported in 3D crystallization does occur in 2D crystallization. The reduced dimensionality and ability to probe the 2D system by STM allowed mechanistic insights into this phenomenon at the molecular level. The molecular interaction between two components plays a critical role in determining assembly structures through kinetic and thermodynamic mechanisms and each plays a role that is dependent on the details of monolayer structure. Because these observations in 2D crystallization can be applied to heteronucleation occurring during attempted cocrystallization, the influence of an additive on adlayer formation can be one of the opperative pathways to kinetically produce a metastable polymorph. In other words, although thermodynamic stabilization of a metastable form by an additive is without analogy 3D crystallization of polymorphs, the thermodynamic selection of 2D crystal forms does offer a potential explanation for kinetic control of polymorphism in cases where heteronucleation prevails.

4.4 Experimental section

4.4.1 Synthesis and characterization of molecules investigated

4-dodecyloxybenzamide (**12-amide**), 4-octadecyloxybenzamide (**18-amide**) and diheptadecyl isophthalate (**17-*m*-diester**) were synthesized as previously reported.[30,36]

Materials: 1,3,5-benzenetricarbonyltrichloride was purchased from Aldrich. 1-heptadecanol and pyridine were purchased from Acros Organics and all solvents were purchased from Fisher Scientific. All reagents were used as received.

Synthesis of triheptadecyl benezene-1,3,5-tricarboxlate (17-triester): To a mixture of 1-heptadecanol (2.90 g, 11.30 mmol) and pyridine (15.1 mmol) in CH_2Cl_2 (50 mL) was added 1,3,5-benzenetricarbonyl trichloride (0.50 g, 1.88 mmol). The mixture was heated to reflux for 5 days. The organic layer was washed with H_2O and brine and dried over anhydrous $MgSO_4$. The solvent was removed under reduced pressure. Pure product was obtained by column chromatography on silica gel with 15% ethyl acetate in hexanes as eluent.

Yield: 1.10 g, 63.2%. mp: 69.0-70.0 °C. ^{1}H NMR (300 MHz, $CDCl_3$, δ): 0.88 (t, J = 6.6 Hz, 9H), 1.20-1.57 (m, 84H), 1.81 (quint, J = 7.0 Hz, 6H), 4.38 (t, J = 6.6 Hz, 6H), 8.85 (s, 3H). ^{13}C NMR (100 MHz, $CDCl_3$, δ): 14.32, 22.90, 26.20, 28.88, 29.58, 29.77 (broad), 32.14, 66.06, 131.71, 134.62, 165.33. Anal. Calcd for $C_{60}H_{108}O_6$: C 77.87, H 11.76; Found: C 78.02, H 11.77. HRMS (EI) calcd. for $C_{60}H_{108}O_6$ (*m/z*): 924.8146, found: 924.8120.

4.4.2 General preparation of solutions

The mixtures with additives were prepared using 100 µM of **18-amide** and 100 µM of an additive. The molar ratio was controlled by using different volume of each

solution. For example, 0.1 µL of 100 µM of **18-amide** and 0.9 µL of 100 µM of an additive were used to make a mixture with 1:9 molar ratio.

4.4.3 Determination of the difference of the activation energy (ΔE_a)

The adsorbate molecular-transfer rate (dN/dt) was described by (dN/dt)$= -\nu N$ exp($-E_a/RT$) at temperature T, where E_a is the activation energy, R is gas constant, and ν is a preexponential factor. Thus, the difference of the activation energy (ΔE_a) can be obtained by $\Delta E_a = E_{a2} - E_{a1} = -RT (\ln^{(d(\ln N)/dt)_2} - \ln^{(d(\ln N)/dt)_1})$ where $d(\ln^N)/dt$ can be obtained by counting the number of molecules associated with the phase transformation. The average values of $d(\ln^N)/dt$ were -0.031 ± 0.007 sec^{-1} for the homogeneous solution of 25 µM of **18-amide** and -0.0034 ± 0.0012 sec^{-1}. Therefore, the ΔE_a was obtained as 1.33 ± 0.36 kcal/mol.

4.5 References

(1) López-Mejías, V.; Kampf, J. W.; Matzger, A. J. *J. Am. Chem. Soc.* **2009**, *131*, 4554-4555.

(2) Vishweshwar, P.; McMahon, J. A.; Oliveira, M.; Peterson, M. L.; Zaworotko, M. J. *J. Am. Chem. Soc.* **2005**, *127*, 16802-16803.

(3) Vrcelj, R. M.; Sherwood, J. N.; Kennedy, A. R.; Gallagher, H. G.; Gelbrich, T. *Cryst. Growth Des.* **2003**, *3*, 1027-1032.

(4) van der Heijden, A.; Bouma, R. H. B. *Cryst. Growth Des.* **2004**, *4*, 999-1007.

(5) Nalwa, H. S.; Saito, T.; Kakuta, A.; Iwayanagi, T. *J. Phys. Chem.* **1993**, *97*, 10515-10517.

(6) Kwon, O. P.; Jazbinsek, M.; Yun, H.; Seo, J. I.; Kim, E. M.; Lee, Y. S.; Gunter, P. *Cryst. Growth Des.* **2008**, *8*, 4021-4025.

(7) Rodríguez-Spong, B.; Price, C. P.; Jayasankar, A.; Matzger, A. J.; Rodríguez-Hornedo, N. *Adv. Drug Delivery Rev.* **2004**, *56*, 241-274.

(8) Weissbuch, I.; Addadi, L.; Lahav, M.; Leiserowitz, L. *Science* **1991**, *253*, 637-645.

(9) Thallapally, P. K.; Jetti, R. K. R.; Katz, A. K.; Carrell, H. L.; Singh, K.; Lahiri, K.; Kotha, S.; Boese, R.; Desiraju, G. R. *Angew. Chem., Int. Ed.* **2004**, *43*, 1149-1155.

(10) He, X. R.; Stowell, J. G.; Morris, K. R.; Pfeiffer, R. R.; Li, H.; Stahly, G. P.; Byrn, S. R. *Cryst. Growth Des.* **2001**, *1*, 305-312.

(11) Mitchell, C. A.; Yu, L.; Ward, M. D. *J. Am. Chem. Soc.* **2001**, *123*, 10830-10839.

(12) Hiremath, R.; Basile, J. A.; Varney, S. W.; Swift, J. A. *J. Am. Chem. Soc.* **2005**, *127*, 18321-18327.

(13) Hiremath, R.; Varney, S. W.; Swift, J. A. *Chem. Commun.* **2004**, 2676-2677.

(14) Price, C. P.; Grzesiak, A. L.; Matzger, A. J. *J. Am. Chem. Soc.* **2005**, *127*, 5512-5517.

(15) Day, G. M.; Trask, A. V.; Motherwell, W. D. S.; Jones, W. *Chem. Commun.* **2006**, 54-56.

(16) Rafilovich, M.; Bernstein, J. *J. Am. Chem. Soc.* **2006**, *128*, 12185-12191.

(17) Lou, B. Y.; Bostroem, D.; Velaga, S. P. *Cryst. Growth Des.* **2009**, *9*, 1254-1257.

(18)   Lancaster, R. W.; Karamertzanis, P. G.; Hulme, A. T.; Tocher, D. A.; Lewis, T. C.; Price, S. L. *J. Pharm. Science* **2007**, *96*, 3419-3431.

(19)   Lei, S.; Tahara, K.; Adisoejoso, J.; Balandina, T.; Tobe, Y.; De feyter, S. *CrystEngComm* **2010**, *12*, 3369-3381.

(20)   Zhou, H.; Dang, H.; Yi, J. H.; Nanci, A.; Rochefort, A.; Wuest, J. D. *J. Am. Chem. Soc.* **2007**, *129*, 13774-13775.

(21)   Scherer, L. J.; Merz, L.; Constable, E. C.; Housecroft, C. E.; Neuburger, M.; Hermann, B. A. *J. Am. Chem. Soc.* **2005**, *127*, 4033-4041.

(22)   Fang, H. B.; Giancarlo, L. C.; Flynn, G. W. *J. Phys. Chem. B* **1999**, *103*, 5712-5715.

(23)   He, Y.; Ye, T.; Borguet E., *J. Phys. Chem. B* **2002**, *106*, 11264-11271.

(24)   Kampschulte, L.; Werblowsky, T. L.; Kishore, R. S. K.; Schmittel, M.; Heckl, W. M.; Lackinger, M., *J. Am. Chem. Soc.* **2008**, *130*, 8502-8507.

(25)   Wei, Y. H.; Kannappan, K.; Flynn, G. W.; Zimmt, M. B., *J. Am. Chem. Soc.* **2004**, *126*, 5318-5322.

(26)   Tao, F.; Bernasek, S. L., *J. Phys. Chem. B* **2005**, *109*, 6233-6238.

(27)   Lackinger, M.; Heckl, W. M., *Langmuir* **2009**, *25*, 11307-11321.

(28)   Ahn, S.; Matzger, A. J. *J. Am. Chem. Soc.* **2009**, *131*, 13826-13832.

(29)   Ahn, S.; Matzger, A. J. *J. Am. Chem. Soc.* **2010**, *132*, 11364-11371.

(30)   Ahn, S.; Morrison, C. N.; Matzger, A. J. *J. Am. Chem. Soc.* **2009**, *131*, 7946-7947.

(31)   Florio, G. M.; Klare, J. E.; Pasamba, M. O.; Werblowsky, T. L.; Hyers, M.; Berne, B. J.; Hybertsen, M. S.; Nuckolls, C.; Flynn, G. W. *Langmuir* **2006**, *22*, 10003-10008.

(32)   Brown, D. E.; Moffatt, D. J.; Wolkow, R. A. *Science* **1998**, *279*, 542-544.

(33)   Lu, X.; Polanyi, J. C.; Yang, J. *Nano Lett.* **2006**, *6*, 809-814.

(34)   Lei, S. B.; Tahara, K.; De Schryver, F. C.; Van der Auweraer, M.; Tobe, Y.; De Feyter, S. *Angew. Chem., Int. Ed.* **2008**, *47*, 2964-2968.

(35)   Tahara, K.; Okuhata, S.; Adisoejoso, J.; Lei, S.; Fujita, T.; De Feyter, S.; Tobe, Y. *J. Am. Chem. Soc.* **2009**, *131*, 17583-17590.

(36)   Plass, K. E.; Kim, K.; Matzger, A. J. *J. Am. Chem. Soc.* **2004**, *126*, 9042-9053.

18-amide **17-*m*-diester** **17-triester** **12-amide**
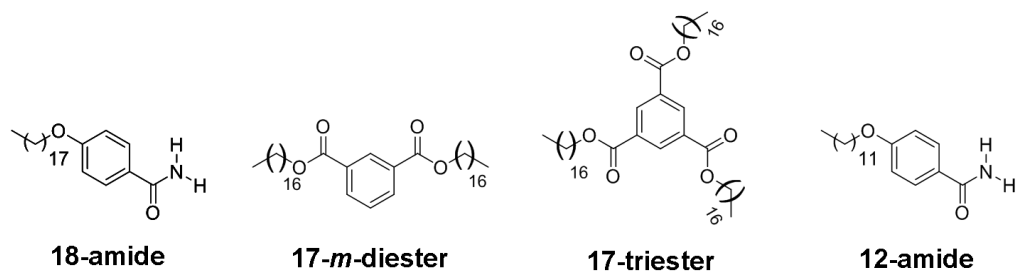
Figure 4.1. Chemical structures investigated.
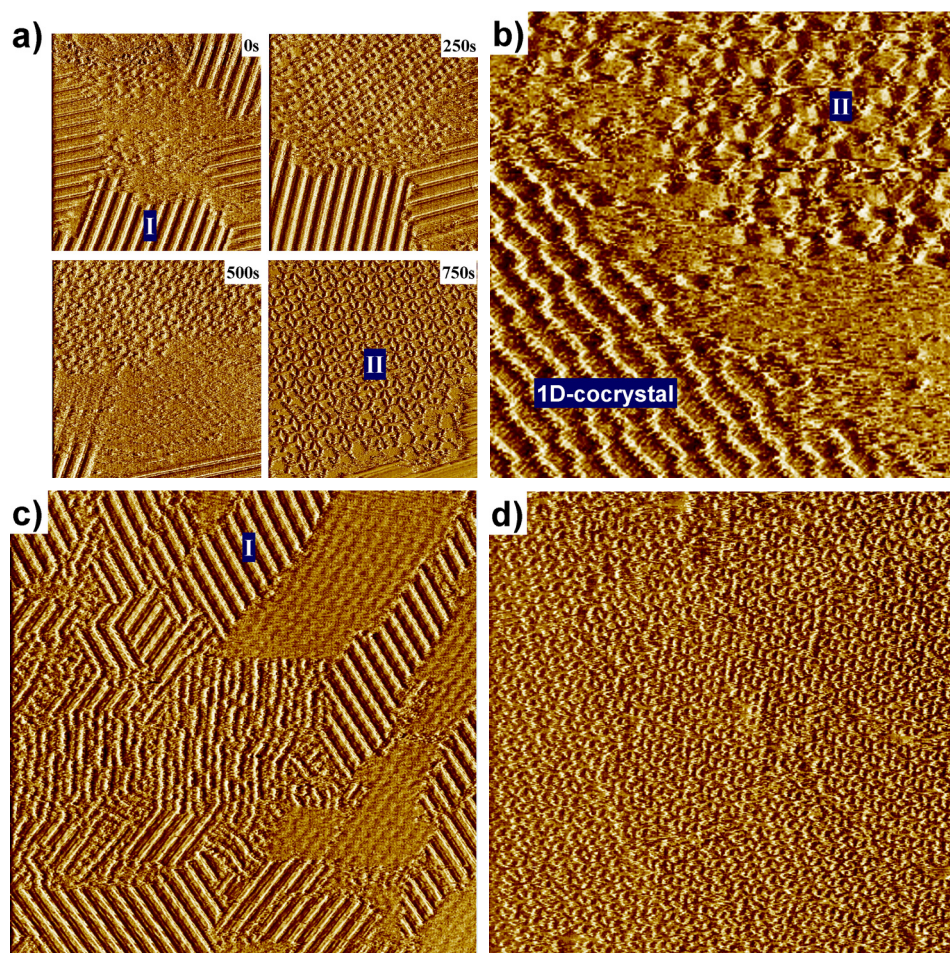
Figure 4.2. Assemblies obtained from the competition study of **18-amide** and **17-*m*-diester**. (a) STM images (100×100 nm^2) showing phase transformation from the close packed phase (phase I) to the rhombic nanoporous network (phase II) observed at 1:6 (**18-amide**:**17-*m*-diester**). (b) STM image (50×50 nm^2) showing coadsorption of phase II of **18-amide** and 1D-cocrystal at 1:11 ratio. (c) STM image (200×200 nm^2) obtained from 1:9 ratio with 52 µM of **18-amide**. (d) STM image (200×200 nm^2) obtained from 1:9 ratio with 10 µM of **18-amide**.
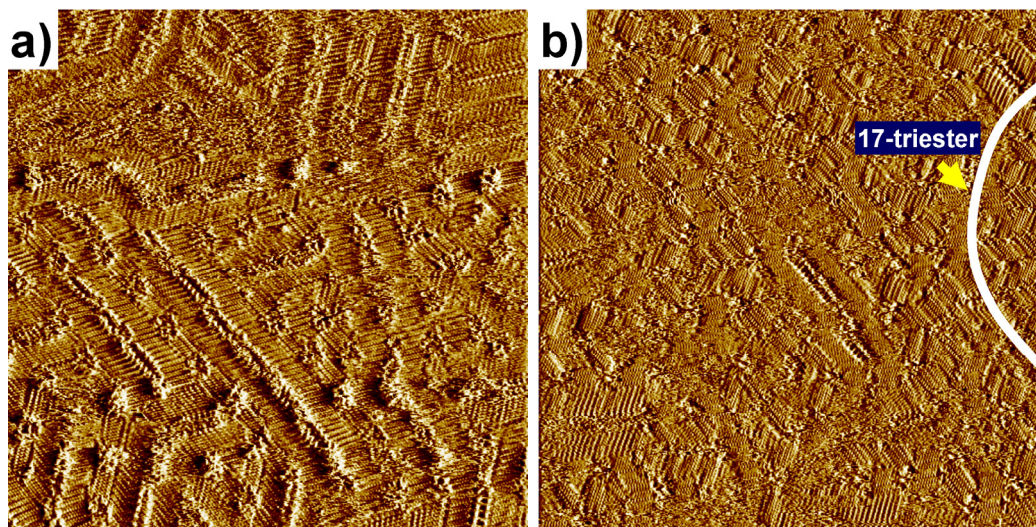
Figure 4.3. Assemblies obtained from the competition study of **18-amide** and **17-triester**. (a) STM image (50×50 nm^2) of the disordered structure of **18-amide** observed at 2:1 (**18-amide**:**17-triester**). (b) STM image (50×50 nm^2) showing coadsorption of **18-amide** and **17-triester** at 1:1 ratio.
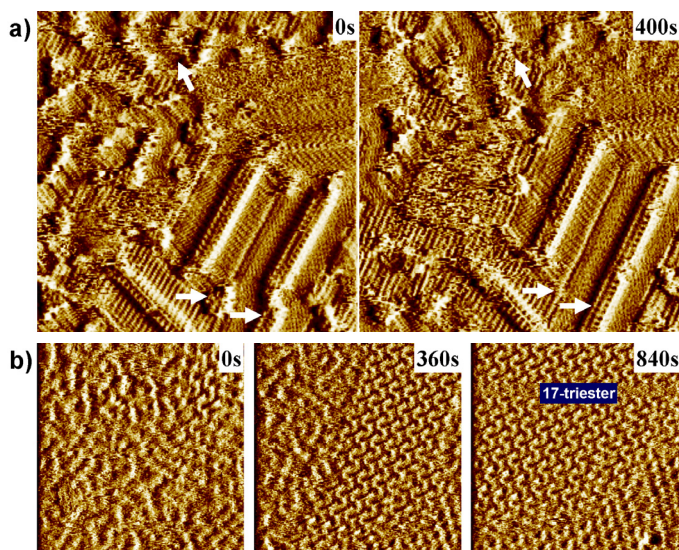
Figure 4.4. Dynamics of assemblies indicating the disorder phase of **18-amide** is a kinetic product induced by the competition with **18-amide** and **17-triester**. (a) STM images (25×25 nm^2) obtained at 2:1 (**18-amide**:**17-triester**) showing dynamics to the more ordered structure. (b) STM images (50×50 nm^2) showing the transformation from disorder of **18-amide** to the ordered **17-triester** phase at 1:1 ratio.
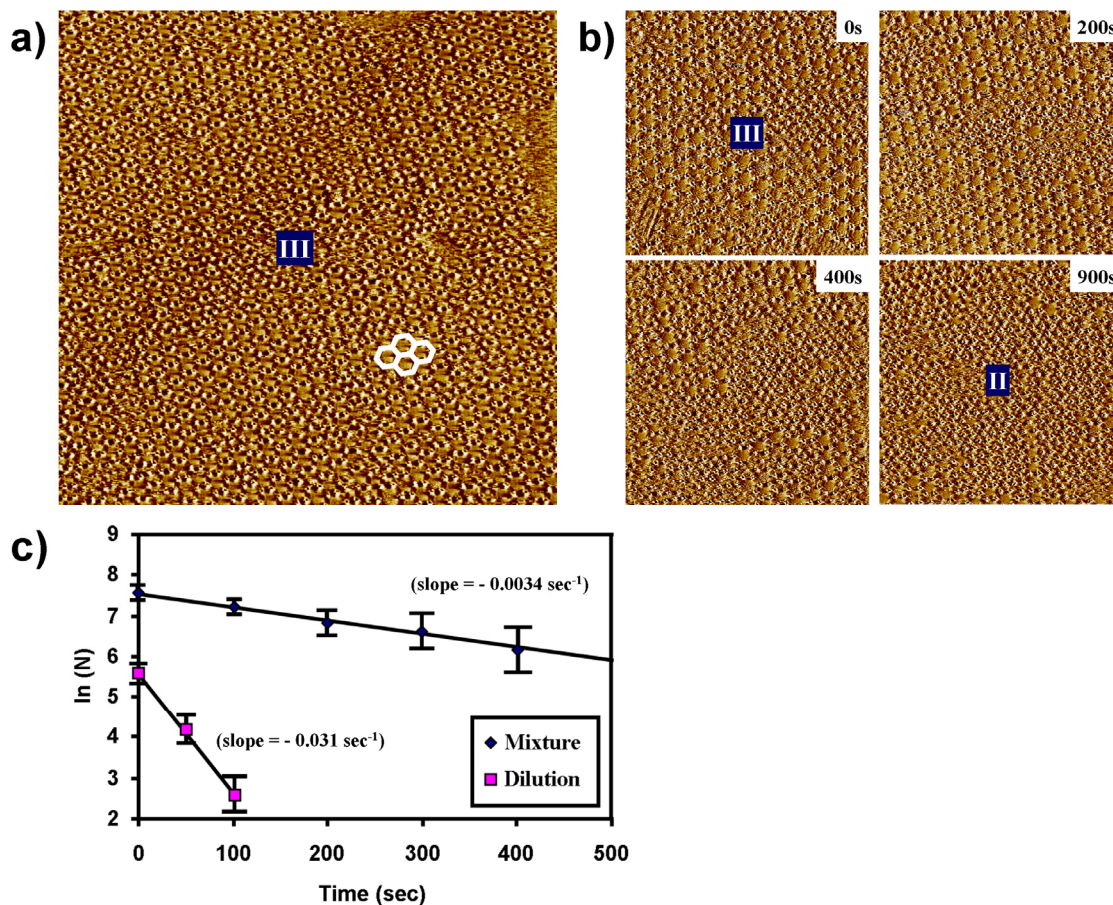
Figure 4.5. Assemblies obtained from the competition study of **18-amide** and **12-amide**. (a) STM image (200×200 nm^2) of the honeycomb nanoporous networks (phase III) with 95% surface coverage at 1:3 (**18-amide**:**12-amide**). (b) STM images (100×100 nm^2) showing phase transformation from phase III to II observed at 1:3. (c) Plot regarding phase transformation from phase III to II observed at the mixture and the diluted homogeneous solution of 25 μM of **18-amide** at room temperature. N is the number of molecules counted.
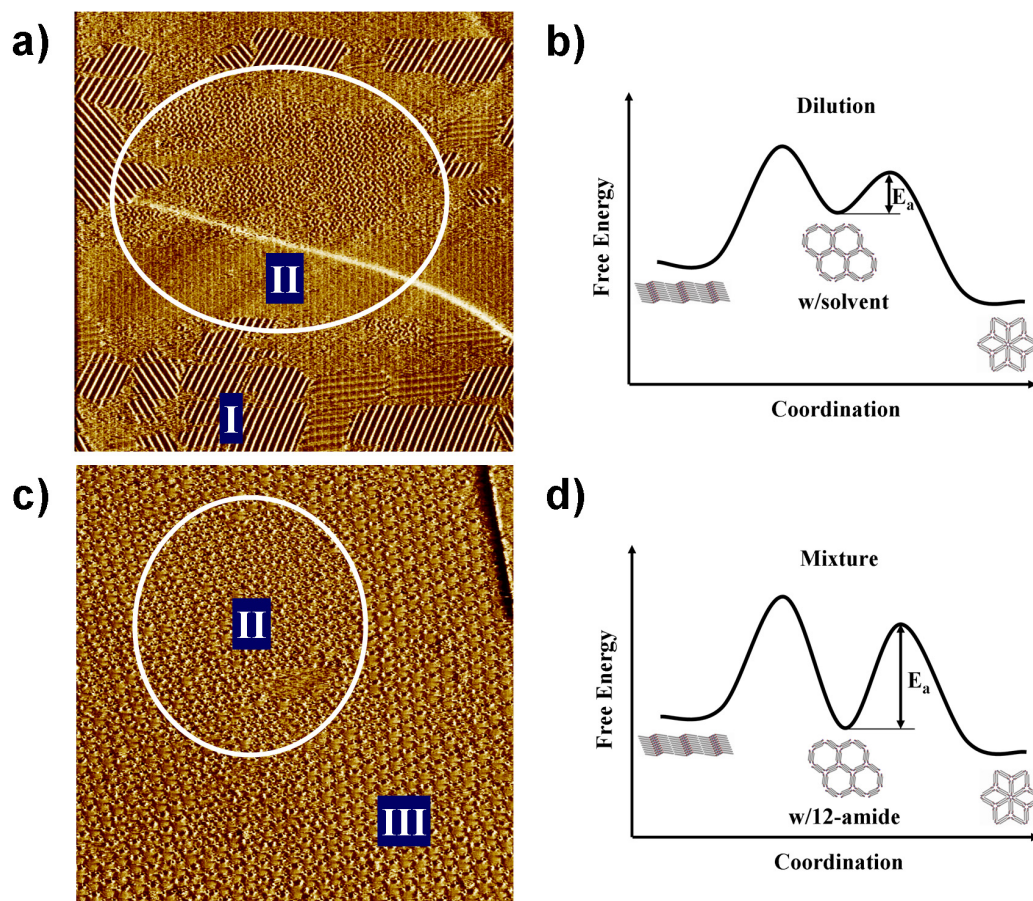
Figure 4.6. STM images ((a) 400 × 400 nm², (c) 200 × 200 nm²) and reaction coordination diagram of the phase transformation from (a), (b) the homogeneous solution of 25 µM and (c), (d) the mixture of 1:3 (**18-amide**:**12-amide**) with 25 µM of **18-amide**. From the mixture solution, phase I is completely transformed to phase III and phase III is slowly transformed to phase II while phase III is an intermediate form during the phase transformation from phase I to II.
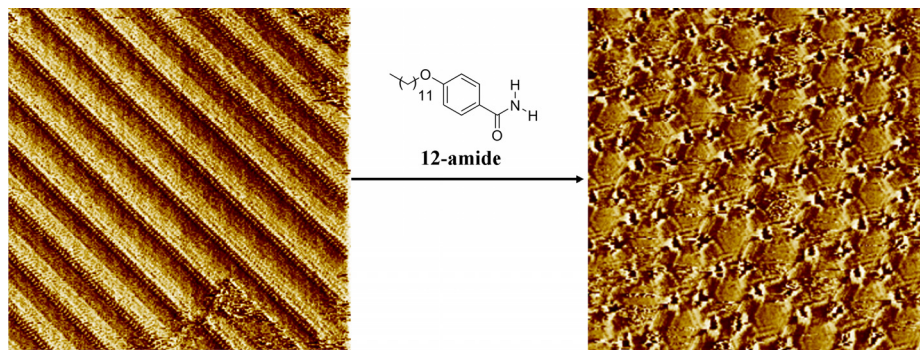
Figure 4.7. STM images (50×50 nm^2) showing the phase transformation from phase I to III by adding **12-amide** solution. After the confirmation of the formation of phase I by **18-amide**, **12-amide** solution was added to make a solution with the molar ratio 1:3 (**18-amide:12-amide**). After then, phase I was transferred to phase III.
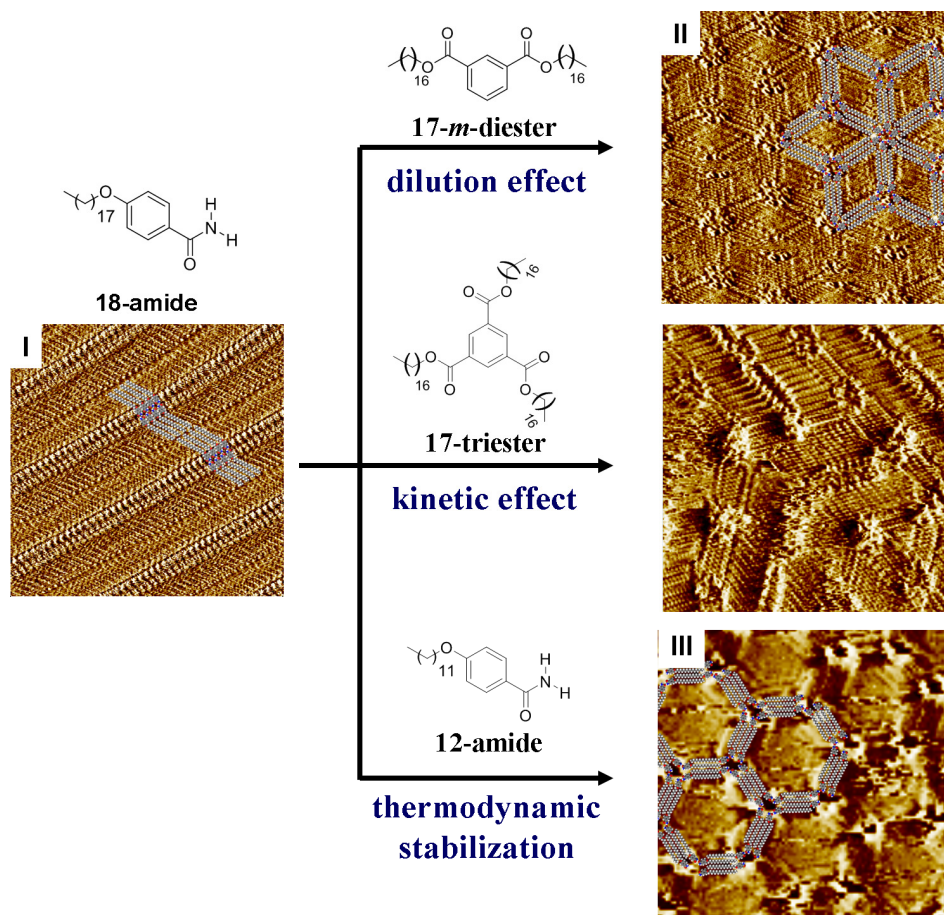
Figure 4.8. Overview of the competition study with an additive. The molar ratio, concentration effect, and an additive structure play a critical role in determining the assembly of **18-amide**.

a)

I	II	II		
18-amide I	18-amide II	coadsorption	1D-cocrystal	17-*m*-diester
1:0	1:3	1:11	1:12	0:1

b)

I	IV		
18-amide I	18-amide IV	coadsorption	17-triester
1:0	2:1	1:1	0:1

c)

I	III	II	
18-amide I	18-amide III	18-amide II	12-amide
1:0	1:3	1:7	1:9 ~ 0:1
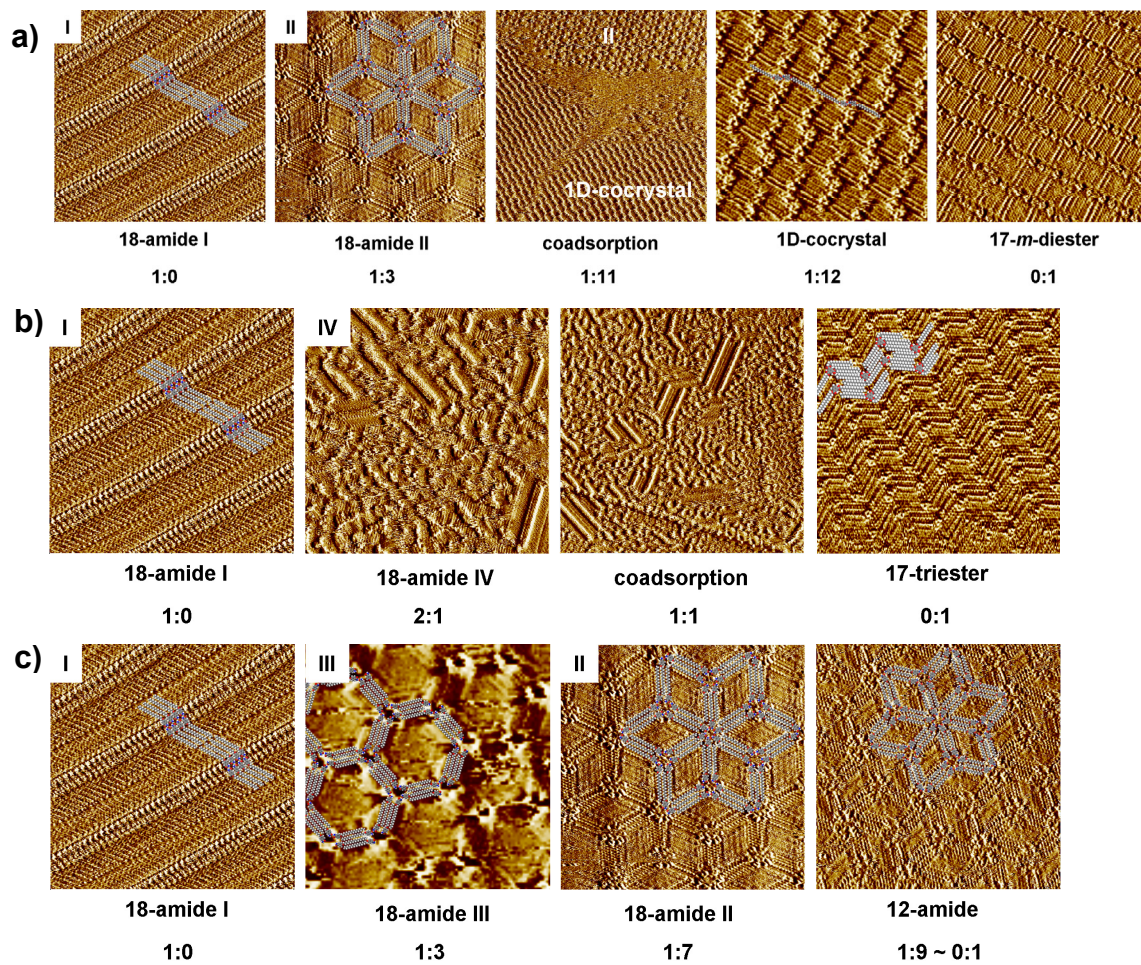
Figure 4.9. The phase change from the mixture of (a) **18-amide** and **17-*m*-diester**, (b) **18-amide** and **17-triester**, and (c) **18-amide** and **12-amide**.

CHAPTER 5

Anatomy of One-Dimensional Cocrystals: Randomness into Order

5.1 Introduction

Most crystallizations conducted in contexts from the laboratory to industrial production involve multicomponent solutions yielding one or more phases. Because of the importance of such processes in purification and solid form engineering, the outcomes of these crystallizations have been studied in great detail with classification schemes describing three general outcomes: 1) segregated single component phases, 2) a homogeneous phase of stoichiometric composition (cocrystallization), and 3) a solid solution. In two-dimensional (2D) crystallizations these same issues arise and the outcome is particularly important for understanding the composition and structure of adsorbed molecules at liquid/solid interfaces. Searching the Two-Dimensional Structural Database (2DSD),[1] a catalog of packing patterns for molecules adsorbed at the liquid/solid interface, reveals that, with some notable exceptions related to the emergence of chirality, the similarities between crystallization in two and three dimensions are quite striking with phase separation, random mixing, and cocrystallization observed commonly in the 2DSD. An advantage of studying this reduced dimensionality system when endeavoring to understand crystallization from multicomponent solutions is that phases which are not fully periodic, and therefore not well suited to study by diffraction

techniques, can readily be imaged in a time dependent fashion using scanning tunneling microscopy (STM) offering structural and mechanistic insights.[2-5]

A multicomponent solution in contact with highly oriented pyrolytic graphite (HOPG) can lead to coadsorption. This may manifest as phase segregation[6], random mixing[7,8] or cocrystallization.[9-15] In general, phase segregation occurs when each component adopts a structure that is identical to that obtained from pure solution. For example, n-tetracontane ($C_{40}H_{82}$) and 4'-octyl-4-biphenylcarbonitrile (8CB) grow crystals in distinct domains due to the different size of the molecules and incompatibility between functional groups.[6] Random mixing occurs when one component is incorporated into the structure of another in a nonperiodic fashion. For example, hexadecyl sulfide (($CH_3(CH_2)_{15})_2S$) inserts randomly into the self-assembled monolayer of tritriacontane ($C_{33}H_{68}$) without disruption of the original monolayer structure because these molecules are of similar dimensions.[7] This phenomenon is observed when two species have sufficiently similar size and functionality to be compatible. Cocrystallization commonly occurs in two situations: (1) strong intermolecular interaction of two different molecules to form an ordered periodic structure such as adenine-thymine (A-T)[11] and guanine-uracil (G-U)[12] base pairs by hydrogen bonding, (2) filling empty space in an open lattice, such as incorporation of coronene into the open structure formed by a star-shaped stilbenoid compound,[14] (host-guest behavior) or in cases where close packing is not well satisfied in a single component structure.[16]

During studies of the competitive adsorption of two components at the liquid/solid interface, a new type of cocrystal, distinguished from the three general outcomes described above was observed. This supramolecular assembly has characteristics of both random mixing and traditional cocrystals. Because this cocrystal shows not only periodicity along one axis, but also nonperiodicity along the other axis it is described as a one-dimensional (1D) cocrystal. This novel packing pattern was characterized by high resolution STM imaging complemented by computed models, and

the formation process was examined through temporally resolved imaging of reversible monolayer reorganization induced by perturbing the STM bias voltage; such composition changes hold potential for applications in high density data storage based on a information coding with molecular-scale features.[17-20] Finally, in order to define this novel cocystallization behavior, the types of 2D crystallization obtained from the multicomponent systems were analyzed in the 2DSD.

5.2 Results and Discussion

Chemical structures of the compounds employed in 2D crystallization are shown in Figure 5.1. The competitive adsorption of 4-octadecyloxybenzamide (**18-amide**) and diheptadecyl isophthalate (**17-*m*-diester**) at the 1-phenyloctane/graphite interface was monitored by STM under ambient conditions. The size and shape of molecules and the compatibility of their functional groups play a key role in determining crystallization behaviors such as phase segregation and random mixing; from these criteria phase segregation of **18-amide** and **17-*m*-diester** was expected due to the dissimilar size/shape and lack of complementary functionality. Although dimerization of the **18-amide** is likely to occur in phenyloctane solution, this unit is still sufficiently different in size and shape from **17-*m*-diester** that random mixing would not be predicted. Against these expectations, the observed behavior, that in several aspects more closely resembles random mixing, is intriguing and derives from a subtle compatibility between the conformation of the self-assembled **17-*m*-diester** and the dimer structure of **18-amide**. This mechanism is discussed below in the context of the formation process of a 1D-cocrystal.

Characteristics of 1D-cocrystal. The phases of pure **17-*m*-diester** have been reported previously.[21] In the lowest energy packing, the column of benzene rings of **17-*m*-diester** is aligned perpendicular to the alkyl chains and these alkyl chains are

73

interdigitated to give a close-packed structure in the plane group *cm* (Figure 5.2a). The phase of pure **18-amide** in phenyloctane is characterized by non-interdigitaed alkyl chains with amides participating in a hydrogen bonding network (Figure 2.4a).[22] When a mixture of **17-*m*-diester** and **18-amide** is present in solution, however, insertion of **18-amide** into the **17-*m*-diester** monolayer occurs as evidenced by the appearance of bright elongated spots corresponding to the aromatic part of the inserted dimer (Figure 5.2b). These coadsorbed dimers of **18-amide** are arranged in lines that extend infinitely; the spacing between these lines is not regular and this non-periodic lattice direction is designated as the non-periodic axis (NPA). A second axis, where molecular composition repeats at defined intervals with a characteristic length scale, is termed the periodic axis (designated PA). The arrangement of the two components results in an unusual unit cell which is represented as white lines in Figure 5.2b. The width of the unit cell, *a*, is 6.10 nm which corresponds closely to the computed dimer length of 6.05 nm. The other parameter of the unit cell is infinite due to the non-periodicity. Because this infinite unit cell is only repeated along the PA, this type of 2D crystal is best termed a 1D-cocrystal.

The 1D-cocrystal is characterized by an alignment shift of **17-*m*-diester** columns through inserting **18-amide** molecules, and as the mole fraction of **18-amide** in solution increases the alignment shift happens with increased frequency due to more prevalent random mixing of **18-amide** (Figure 5.2c). Upon increasing the proportion of **18-amide** from 20:1 to 12:1 (**17-*m*-diester**:**18-amide**), there is a dramatic change from nonperiodicity to pseudoperiodicity along the NPA where the pure phase of either **18-amide** or **17-*m*-diester** has not been observed at this molar ratio range. Pseudoperiodicity describes this phenomenon because the spacing in the second dimension is almost regular; for example, one area of the 1D-cocrystal monolayer shows a periodic pattern indicated by a blue square in Figure 5.2c. Inspection of an expanded region of the 12:1 mixture offers detailed structural information (Figure 5.2d). In order to complement STM images, the computed model of the 2D crystal in this region was constructed based on

high resolution images and energy minimized to obtain the optimized packing structure (Figure 5.3). The orientation of **17-*m*-diester** in the north and south of the **18-amide** row can be determined by the contrast difference where the opposite orientation of C=O groups results in the slight variation of the contrast of the aromatic rings.[21,23] No contrast difference observed in the present case supports that the orientation of **17-*m*-diester** may be same in the north and south of the **18-amide** row. The symbol ΔC in Figure 3 represents the column length of contiguous **17-*m*-diester** molecules in each column. The experimental value for ΔC corresponding to three inserted molecules is 3.12 nm and this value matches well with the ΔC of 3.00 nm from the computed model.

Further increasing the proportion of **18-amide** from the 12:1 mixture does not lead to more insertion of **18-amide** into the 1D-cocrystal. To explore the origin of this saturation effect, lattice energies were computed for several observed and hypothetical packing patterns normalized to a per unit cell area basis.[24] These energies were obtained by constructing fully periodic 1D-cocrystals with various ΔC (Figure 5.4a).[25,26] The change in lattice energy is small as ΔC decreases from 10 to 3. However, when the column length is shorter than 3, the lattice energy of the 2D crystals dramatically increases due primarily to a significant reduction in van der Waals interactions. The contribution to the lattice energy from the electrostatic term is uniformly small because the **17-*m*-diester** phase is primarily stabilized through alkyl chain interdigitation (Table 5.1 and 5.2). Experimentally, the average ΔC changes from 10.86 nm to 3.61 nm as the proportion of **18-amide** increases from 20:1 to 12:1 (**17-*m*-diester**:**18-amide**) and the fact that substantially smaller ΔC values are not obtained agrees well with the computations and leads to the observed saturation behavior. These results reveal that surface composition can be controlled by variation of the ratio of adsorbates in solution so that nanoscale features arise from the alignment shift, offering a facile approach to 2D patterning. Notably, this pseudoperiodicity or pattern change is controlled perpendicular

to the long molecular axis: the most difficult direction to control nanoperiodicity in these types of physisorbed monolayers.[27,28]

Formation Process. The formation of the 1D-cocrystal is proposed to arise through a mechanism having characteristics of both random mixing and cocrystallization. During the adsorption of **17-*m*-diester**, the dimer of **18-amide** may interrupt this process; although the amide can not substitute directly in the lattice of the diester due to the size difference, the compatibility of shape and functionality between the **18-amide** dimer and the monolayer structure of **17-*m*-diester** (Figure 5.5a) allows insertion at the propagating front. The shape of the domain edge of **17-*m*-diester** is compatible with that of the dimer of **18-amide** (blue line in Figure 5.5a) and furthermore there is an attractive interaction between **17-*m*-diester** and **18-amide** mediated by hydrogen bonding (Figure 5.5c). The computed N-H···O distances of 1.81 and 1.77 Å between two **18-amide** molecules are well within the typical values of hydrogen bonding distances (1.6~2.0 Å). The computed N-H···O distance of 2.77 Å and angle of 141.7° between **17-*m*-diester** and **18-amide** indicates weak hydrogen bonding stabilizing the coadsorbed dimer of **18-amide**. Therefore, the combination of the compatibility of shape and functionality between the dimer of **18-amide** and the monolayer structure of **17-*m*-diester** result in random mixing along the NPA. After this random mixing, a new propagation of **17-*m*-diester** may start from the inserted dimer of **18-amide** and this causes the alignment shift of **17-*m*-diester** (Figure 5.5b). This shift is driven by close packing, which is the tendency for 2D crystals,[1] where there is no significant interaction such as hydrogen bonding between the dimer and the newly propagated **17-*m*-diester** molecules. This driving force makes it possible to shift the alignment of **17-*m*-diester**. This re-alignment of **17-*m*-diester** creates some space as shown in Figure 5.4b. At this point, one hypothesis is needed in order to explain 1D periodicity. The hypothesis is that filling this space with the dimer is thermodynamically more favorable than filling with **17-*m*-diester** because the dimer more effectively reduces void space. Based on this hypothesis, dimers of **18-amide** can

be periodically aligned along the PA by satisfying close packing. Experimental verification of this hypothesis was obtained through reversible monolayer reorganization.

Reversible monolayer reorganization. In an STM experiment, changing current or bias voltage can cause perturbation of an adsorbed phase, which can result in transformation to another, typically thermodynamically unstable, phase upon intial monolayer disruption.[29,30] The outcome of this experiment for a two component monolayer, such as the 1D-cocrystal presented here, is not well precedented. In the present case, one part of the 1D-cocrystal changed to the phase of pure **17-*m*-diester** upon perturbation followed by a reversion to the 1D-cocrystal phase. Sequential STM images of this transformation from the **17-*m*-diester** phase to the 1D-cocrystal phase directly demonstrates the thermodynamic stability relationship. In an attempt to perturb the 1D-cocrystal (Figure 5.6a), the applied voltage was changed from 800 mV to 2000 mV when scanning the monolayer for 50 sec. After this perturbation, the time set as 0 sec and the applied voltage was returned to 800 mV to get STM images in Figure 5.6. One area of the 1D-cocrystal was transformed to the phase of **17-*m*-diester** (Figure 5.6b, 5.7). After 100 sec, the 1D-cocrystal phase is still changing to form the phase of **17-*m*-diester** (Figure 5.6c, white oval). This phase change results in the creation of a boundary area between **17-*m*-diester** and 1D-cocrystal phases. The molecularly resolved boundary area is indicated with a blue square and additional boundary areas appear unresolved due to high mobility of molecules.[29] Because close packing is not satisfied in this area due to the mismatch of the two different phases (Figure 5.8), exchange of molecules occurs at the boundary area to build the thermodynamically more stable structure. If the hypothesis that filling the space near the adsorbed dimer with other dimers is thermodynamically more favorable than with a **17-*m*-diester** is correct, the boundary area should be transformed to a 1D-cocrystal phase by periodically inserting dimers of **18-amide**. This behavior was observed after 200 sec through sequential STM images as evidenced by the **17-*m*-diester** starting to transform to the 1D-cocrystal phase by inserting dimers at the

77

boundary area (Figure 5.6d). The disrupted 1D-cocrystal phase is recovering by periodically inserting dimers thus maintaining 1D periodicity (white oval circles in Figure 5.6d). This phenomenon proves that close packing is better satisfied by inserting the dimer of **18-amide** rather than **17-*m*-diester**. After 950 sec, the **17-*m*-diester** phase is completely transformed to the initial 1D-cocrystal phase (Figure 5.6e, f). This result shows not only the formation process of the 1D-cocrystal but also demonstrates the potential of molecular switching using the physisorbed 1D-cocrystal on HOPG under ambient conditions.

2DSD Analysis. To put these results in the broader context of existing monolayers, a search of the Two-Dimensional Structural Database (2DSD) was conducted.[31] The 2DSD construction and general molecular packing and symmetry of 2D crystals formed at the liquid/solid interface were previously reported.[1] This analysis revealed, for example, the close packing theory of 2D crystals is well supported by experimental data as evidenced by the frequency of certain plane groups. However, the types and frequency of the outcomes for crystallization from solutions containing two adsorbing species have not been reported in detail. These trends are analyzed here using the 2DSD and the present 1D-cocrystal is classified based on this analysis. Of the 876 entries in the 2DSD, 145 of these are formed from multicomponent solutions. Most frequently these are random mixtures (30.3%), but phase segregation (26.9%) and cocrystals (24.8%) are common and are distinct from the present 1D-cocrystal. Six cases of replacement (4.1%), which is the phase change from the pure phase of one component to the pure phase of the other component, and nine cases of metal complexes (6.2%) are observed. Ten cases (6.9%) are not assigned because the paper reported the experiment but not the results or the image quality led to ambiguities in assignment. One case relating to the present 1D-cocrystal was found.[32] An oligothiophene derivative containing side chain urea functionality inserted into the mono-urea derivative phase by forming hydrogen bonds between urea groups at one position in the bulk monolayer of the mono

urea. Inserted oligothiophenes were oriented along one axis and an alignment shift of the mono-urea derivative phase to form another hydrogen bonding pattern was observed. However, there are two things different from the present case: (1) a uniform monolayer was not formed because inserted oligothiophene molecules sometimes formed clusters of a few molecules and (2) an alignment shift occurred only once and an additional shift was not reported. By contrast, the average frequency of the alignment shift can be controlled through changing the molar ratio of components in the present case and complete coverage by a single phase is observed. The case of the oligothiophene derivative is consistent defect appearance at a domain boundary rather than a new type of periodic behavior. Therefore, the present 1D-cocrystal is regarded as a new type of 2D crystallization behavior to be considered as distinct from the commonly accepted outcomes of phase segregation, random mixing, and cocrystallization.

5.3 Conclusions

X-ray diffraction, the most common method for studying structure of bulk crystalline materials, is poorly suited for studying materials with imperfect periodicity. The findings presented here demonstrate that the approach of using 2D crystallization monitored by STM as a model system for three dimensional crystals offers mechanistic and structural insights not available using tools suited for studying three dimensional crystals. During a competitive adsorption study, a novel type of coadsorption, 1D-cocrystal, distinguished from preceding outcomes from multicomponent solutions was observed. This assembly mode has characteristics of both random mixing and traditional stoichiometric cocrystallization and results in an alignment shift of the dominant phase. In addition, the frequency of the alignment shift can be controlled by variation of the ratio of adsorbates. This result demonstrates that the surface composition and patterns are variable through controlling the molar ratio of components and structural modulation is

controlled perpendicular to the long molecular axis: the most difficult direction to control nanoperiodicity in these types of physisorbed monolayers. Identification of a new mode of assembly from multicomponent solutions is important due to the prevalence of crystallization processes in purification and solid form engineering. Furthermore, because the observations were made on graphite, the findings are likely directly relevant to purification of materials by adsorption to carbonaceous sorbents containing graphitic domains.

5.4 Experimental section

General experimental procedures for imaging and computation are described in Chapter 1.4

5.5 References

(1)   Plass, K. E.; Grzesiak, A. L.; Matzger, A. J. *Acc. Chem. Res.* **2007**, *40*, 287-293.

(2)   Li, S. S.; Yan, H. J.; Wan, L. J.; Yang, H. B.; Northrop, B. H.; Stang, P. J. *J. Am. Chem. Soc.* **2007**, *129*, 9268-9269.

(3)   Lei, S.; Tahara, K.; Feng, X.; Furukawa, S.; De Schryver, F. C.; Müllen, K.; Tobe, Y.; De Feyter, S. *J. Am. Chem. Soc.* **2008**, *130*, 7119-7129.

(4)   Scherer, L. J.; Merz, L.; Constable, E. C.; Housecroft, C. E.; Neuburger, M.; Hermann, B. A. *J. Am. Chem. Soc.* **2005**, *127*, 4033-4041.

(5)   Fang, H.; Giancarlo, L. C.; Flynn, G. W. *J. Phys. Chem. B* **1999**, *103*, 5712-5715.

(6)   Baker, R. T.; Mougous, J. D.; Brackley, A.; Patrick, D. L. *Langmuir* **1999**, *15*, 4884-4891.

(7)   Padowitz, D. F.; Messmore, B. W. *J. Phys. Chem. B* **2000**, *104*, 9943-9946.

(8)   Xie, Z. X.; Xu, X.; Mao, B. W.; Tanaka, K. *Langmuir* **2002**, *18*, 3113-3116.

(9)   Tao, F.; Bernasek, S. L. *J. Am. Chem. Soc.* **2005**, *127*, 12750-12751.

(10)   Yang, X.; Mu, Z.; Wang, Z.; Zhang, X.; Wang, J.; Wang, Y. *Langmuir* **2005**, *21*, 7225-7229.

(11)   Mamdouh, W.; Dong, M.; Xu, S.; Rauls, E.; Besenbacher, F. *J. Am. Chem. Soc.* **2006**, *128*, 13305-13311.

(12)   Mamdouh, W.; Kelly, R. E. A.; Dong, M.; Kantorovich, L. N.; Besenbacher, F. *J. Am. Chem. Soc.* **2008**, *130*, 695-702.

(13)   Kampschulte, L.; Werblowsky, T. L.; Kishore, R. S. K.; Schmittel, M.; Heckl, W. M.; Lackinger, M. *J. Am. Chem. Soc.* **2008**, *130*, 8502-8507.

(14)   Schull, G.; Douillard, L.; Fiorini-Debuisschert, C.; Charra, F.; Mathevet, F.; Kreher, D.; Attias, A.-J. *Nano Lett.* **2006**, *6*, 1360-1363.

(15)   Furukawa, S.; Tahara, K.; De Schryver, F. C.; Auweraer, M. V.; Tobe, Y.; De Feyter, S. *Angew. Chem., Int. Ed.* **2007**, 46, 2831-2834.

(16)   For discussion of this phenomenon in three dimensional crystals structures, see Price, C. P.; Glick, G. D.; Matzger, A. J. *Angew. Chem., Int. Ed*. **2006**, *45*, 2062-2066.

(17)   Cavallini, M.; Biscarini, F.; Leon, S.; Zerbetto, F.; Bottari, G.; Leigh, D. A. *Science* **2003**, *299*, 531.

(18)   Feng, M.; Gao, L.; Deng, Z.; Ji, W.; Guo, X.; Du, S.; Shi, D.; Zhang, D.; Zhu, D.; Gao, H. *J. Am. Chem. Soc.* **2007**, *129*, 2204-2205.

(19)   Sato, A.; Tsukamoto, Y. *Adv. Mater.* **1994**, *6*, 79-80.

(20)   Shang, Y.; Wen, Y.; Li, S.; Du, S.; He, X.; Cai, L.; Li, Y.; Yang, L.; Gao, H.; Song, Y. *J. Am. Chem. Soc.* **2007**, *129*, 11674-11675.

(21)   Plass, K. E.; Kim, K.; Matzger, A. J. *J. Am. Chem. Soc.* **2004**, *126*, 9042-9053.

(22)   Ahn, S.; Morrison, C. N.; Matzger, A. J. *J. Am. Chem. Soc.* **2009**, *131*, 7946-7947.

(23)   De feyter, S.; Grim, P. C. M.; van Esch, J.; Kellogg, R. M.; Feringa, B. L.; De Schryver, F. C. *J. Phys. Chem. B* **1998**, *102*, 8981-8987.

(24)   The stabilization energies on a per unit cell area basis have been discussed to compare the stability of 2D crystals (see Kim, K.; Plass, K. E.; Matzger, A. J. *J. Am. Chem. Soc.* **2005**, *127*, 4879-4887) as a per molecule basis could not be applied due to the composition change upon the column length the column length change with compositions.

(25)   After energy minimization of each fully periodic 1D-cocrystal model, the energies of isolated molecules of **17-m-diester** and the dimer of **18-amide** are subtracted to get the stabilization energies per a unit cell. These values are divided by the area of each unit cell to get the stabilization energies on a per unit area.

(26)   The unit cells in Figure 4a contain 2n+1 molecules, where n is the **17-*m*-diester** column length and the **18-amide** dimer is treated as a single unit. The number of defects (**18-amide** dimers) in these unit cells varies as 1/(2n+1). The plot in Figure 4 is well fit by Lattice energy = 6.71 kcal/nm^2 x (1/(2n+1)) − 8.94 kcal/nm^2. The density of defects is determined by a 6.71 kcal/nm^2 energy increase.

(27)   Wei, Y.; Tong, W.; Zimmt, M. B. *J. Am. Chem. Soc.* **2008**, *130*, 3399-3405.

(28)   Plass, K. E.; Engle, K. M.; Cychosz, K. A.; Matzger, A. J. *Nano Lett.* **2006**, *6*, 1178-1183.

(29)   Plass, K. E.; Matzger, A. J. *Chem. Commun.* **2006**, 3486-3488.

(30)   Lu, X.; Polanyi, J. C.; Yang, J. *Nano Lett.* **2006**, *6*, 809-814.

(31)   The 2DSD is now publicly available at http://2dsd.lsa.umich.edu.

(32)   De Feyter, S.; Larsson, M.; Gesquiere, A.; Verheyen, H.; Louwet, F.; Groenendaal, B.; Esch, J.; Feringa, B. L.; De Schryver, F. *ChemPhysChem* **2002**, *11*, 966-969.
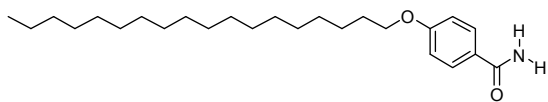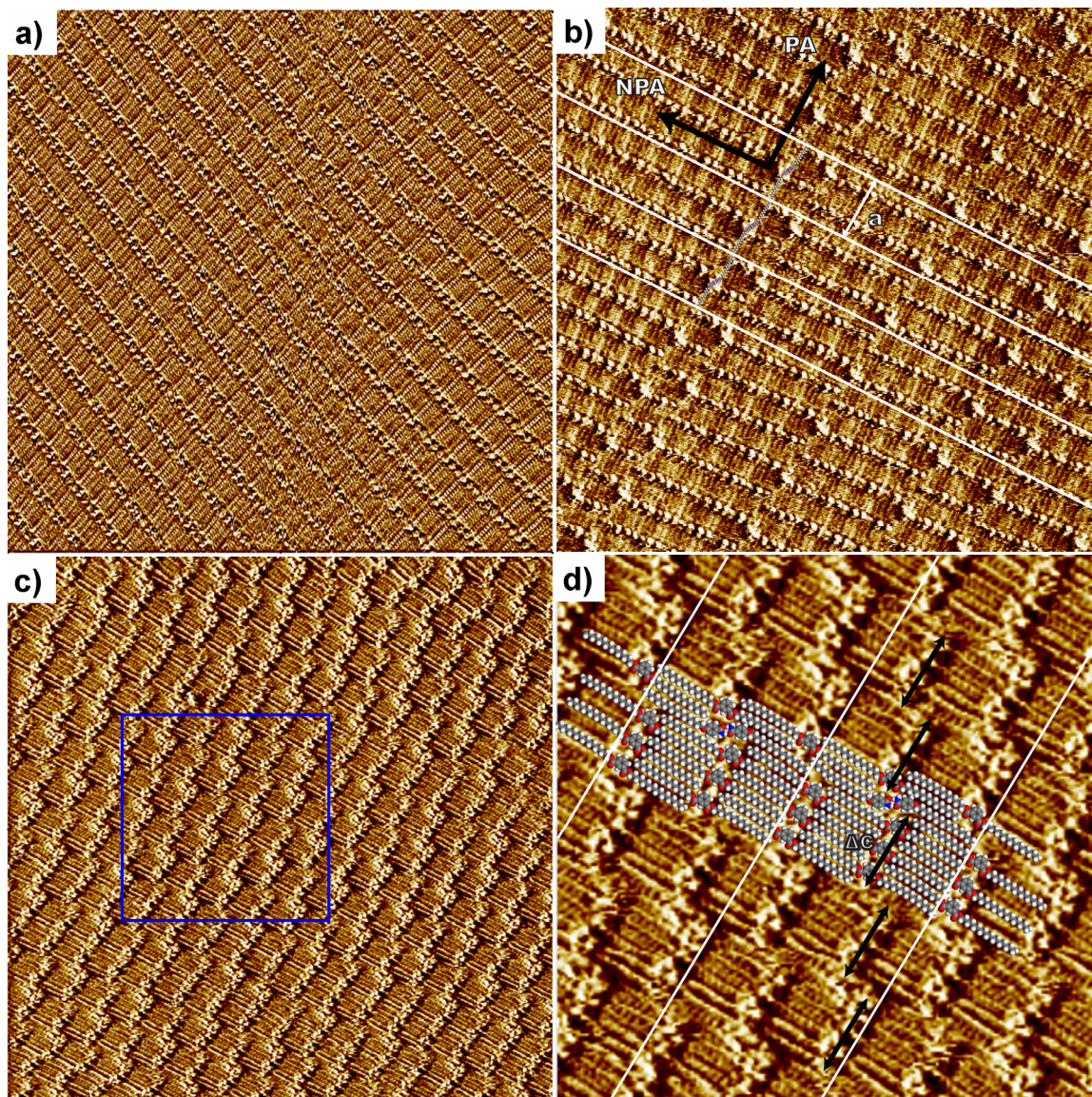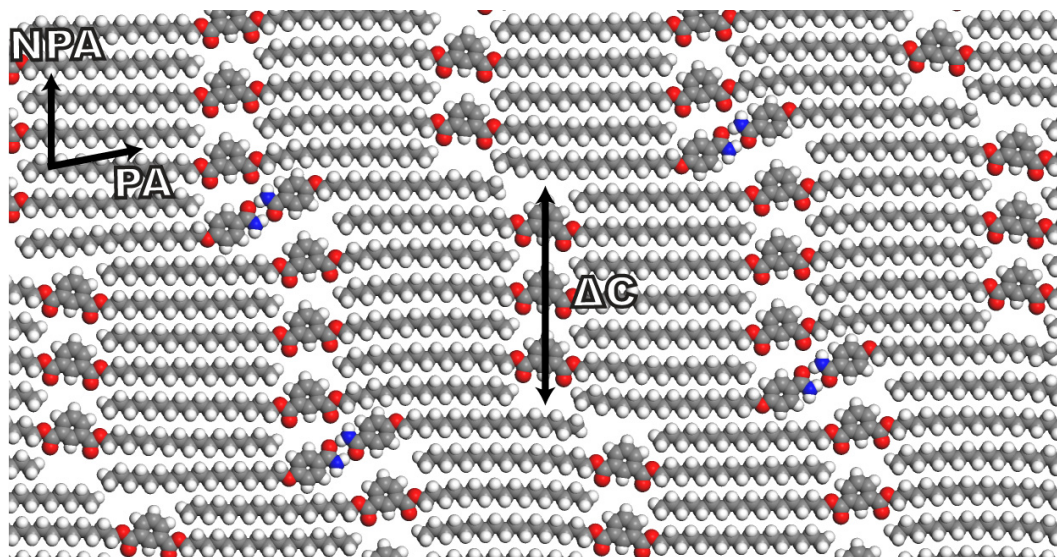
18-amide
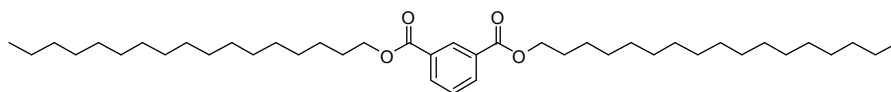
17-*m*-diester
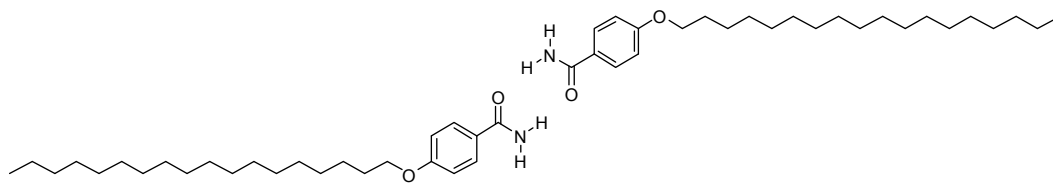

dimer of 18-amide

Figure 5.1. Chemical structures of molecules imaged by STM.

Figure 5.2. STM Images of (a) **17-*m*-diester** and (b) 1D-cocrystal formed by inserting dimers of **18-amide** into **17-*m*-diester** columns from a 20:1 mixture (**17-*m*-diester**:**18-amide**) in phenyloctane on HOPG (50 × 50 nm^2, 10.2 Hz, 800 mV, 300 pA). Black arrows indicate the periodic axis (PA) and the non-periodic axis (NPA). (c) STM image of 1D-cocrystal from a 12:1 mixture (**17-*m*-diester**:**18-amide**) on HOPG (50 × 50 nm^2, 10.2 Hz, 800 mV, 300 pA). The blue square in (c) indicates a region where there is a saturation effect on column length. (d) Magnified STM image (20 × 20 nm^2) of the blue square area indicated in (c). An arrow represents a column length (ΔC) of contiguous **17-*m*-diester** molecules in each column. An optimized molecular model is overlaid to aid visualization of the molecular conformation and white lines represent unit cells of 1D cocrystal (b,d).

Figure 5.3. The computed packing pattern of 1D-cocrystal showing a repeat distance along the NPA at a 12:1 molar ratio (**17-*m*-diester**:**18-amide**). An arrow represents a column length (ΔC) of 3.00 nm of contiguous **17-*m*-diester** molecules in each column.
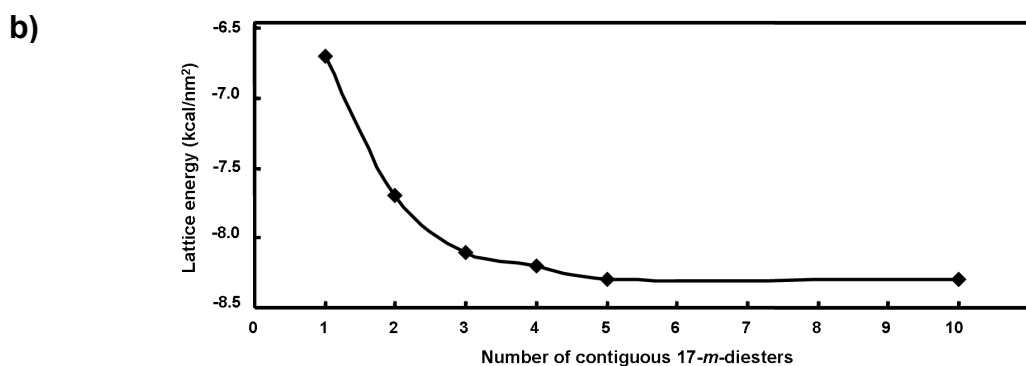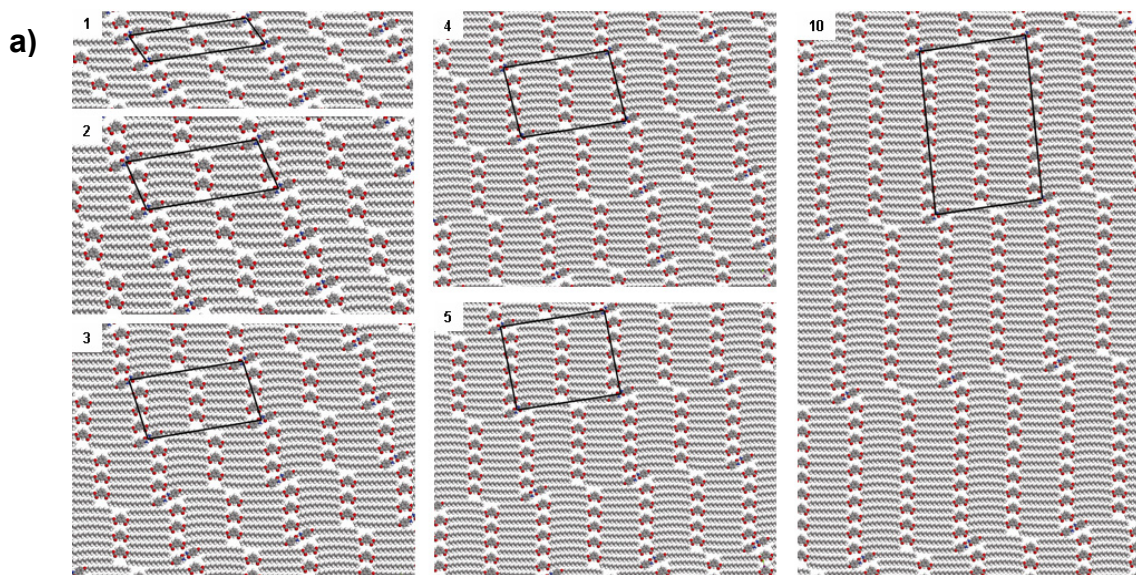
Figure 5.4. (a) Periodic models of 1D-cocrystals depending on the column length of contiguous **17-*m*-diester** molecules in each column. The inset value indicates the numbers of these contiguous **17-*m*-diester** molecules. (b) The lattice energies computed by the COMPASS force field (kcal/nm^2) based on the periodic 1D-cocrystal models. The values represent the energy obtained by the formation of the periodic assembly from isolated **17-*m*-diester** and the dimer of **18-amide**.

Table 5.1. The Unit Cell Parameters of Each Computed Model and Estimated Area of Each Unit Cell.

contiguous 17-m-diesters	1	2	3	4	5	10
a (nm)	6.13	6.11	6.08	6.08	6.07	6.10
b (nm)	1.68	2.43	3.26	4.12	4.99	9.45
α (°)	117.2	104.4	98.0	94.9	92.5	86.8
area (nm^2)	9.17	14.41	19.66	24.96	30.27	57.50

Table 5.2. Computed Lattice Energies (kcal/nm^2) of the 1D-Cocrystals.

contiguous 17-m-diesters	1	2	3	4	5	10
lattice energy	-6.7	-7.7	-8.1	-8.2	-8.3	-8.3
van der Waals term	-6.7	-7.6	-8.0	-8.1	-8.2	-8.1
electrostatic term	0.0	-0.1	-0.1	-0.1	-0.1	-0.2
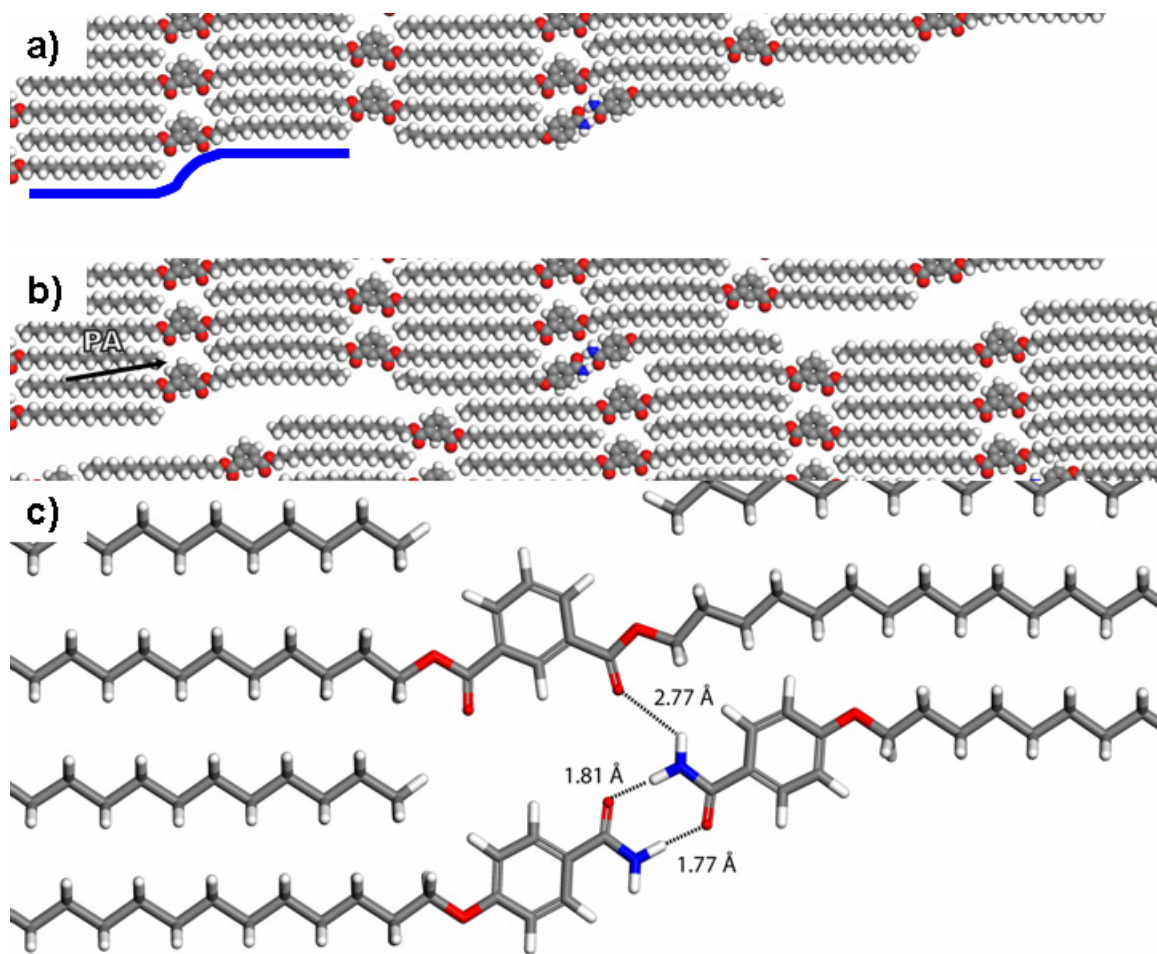
Figure 5.5. Suggested models for the 1D cocrystallization process. (a) the initial coadsorption model showing geometric and functional compatibility. A blue line shows the geometry of the domain edge of **17-*m*-diester** matches well with the shape of the dimer of **18-amide**. (b) Model with two dimers abstracted from the 1D cocrystal to illustrate the void space shape, and (c) the computed hydrogen bond distances of (a) showing compatibility of functionality.
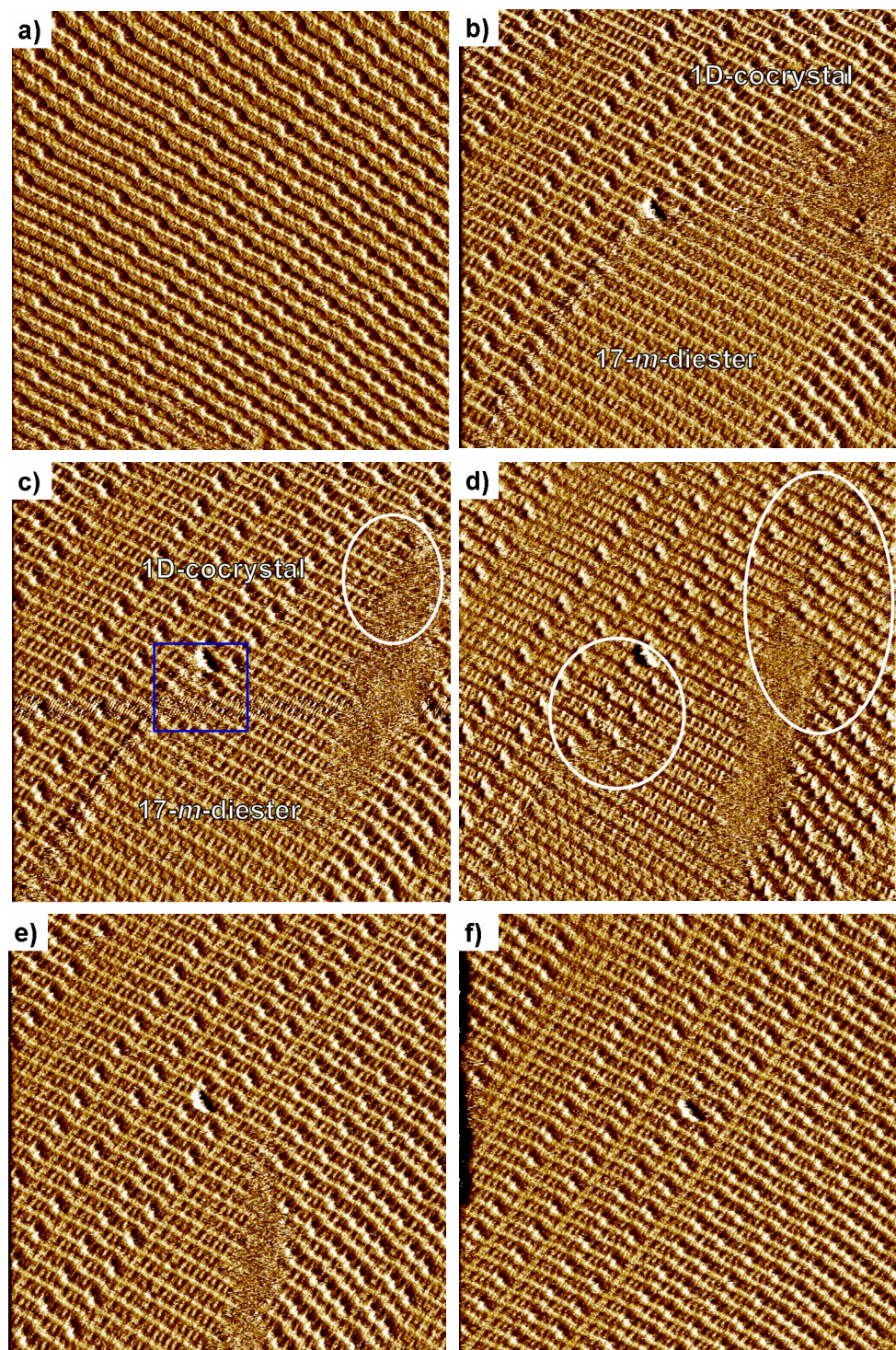
Figure 5.6. Sequential STM images from a 14:1 mixture (**17-*m*-diester**:**18-amide**) on HOPG (80 × 80 nm², 10.2 Hz, 800 mV, 300 pA). (a) 1D-cocrystal (b) after applying 2000 mV for 50 sec (t = 0) (c) 100 sec (d) 200 sec (e) 400 sec (f) 950 sec. A white oval indicates areas of significant change from the previous image and a blue square indicates the boundary area between **17-*m*-diester** and 1D-cocrystal phases.
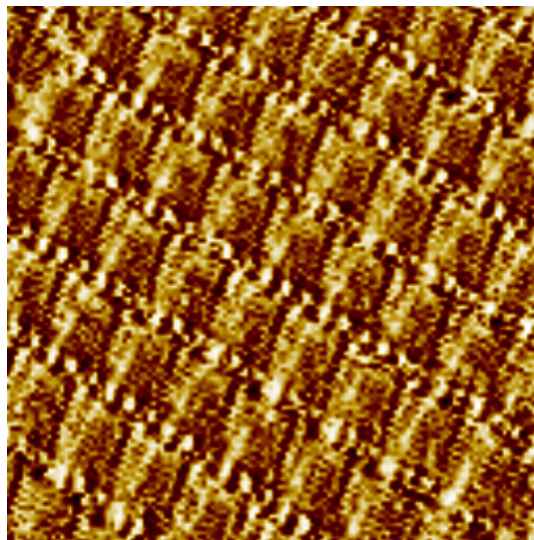
Figure 5.7. STM image (20×20 nm^2) of **17-*m*-diester** phase newly formed after the perturbation of 1D-cocrystal monolayer.
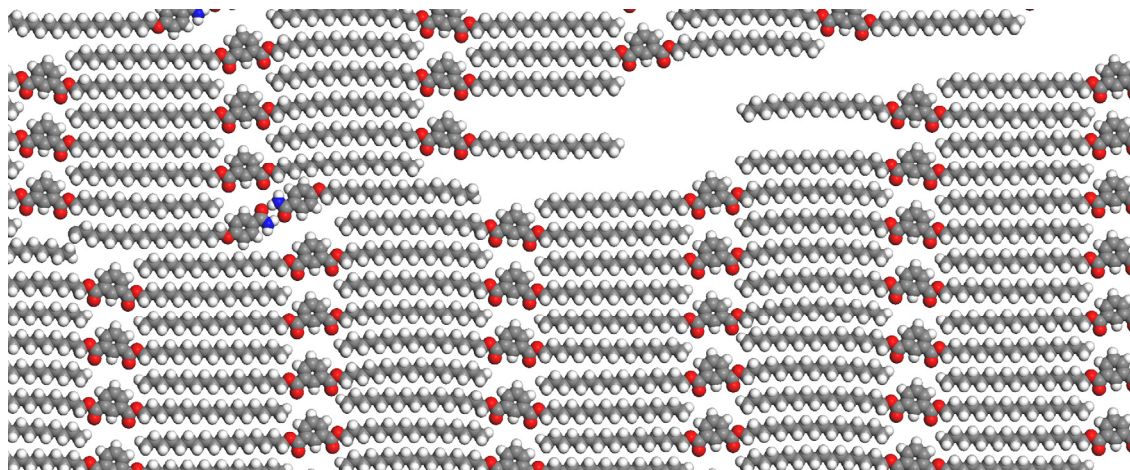
Figure 5.8. Model of the boundary area between **17-*m*-diester** and 1D-cocrystal phases.

CHAPTER 6

Conclusion and Future Directions

6.1 Introduction

This chapter addresses the connections among the previous chapters and the key results in each chapter. Based on these results, the future directions of this research are also addressed. In order to understand crystallization behavior from multicomponent solutions, a compound that has ability to exist in multiple crystalline phases in 2D was found and its structural diversity was demonstrated in Chapters 2 and 3. Using this amide amphiphile and other additives, crystallization behaviors from multicomponent solutions, which have been poorly understood inform a kinetic and thermodynamic standpoint, were studied at the molecular level with the aid of STM in Chapter 4 and 5.

6.2 Two-dimensional crystallization of an amide amphiphile

It was demonstrated in Chapter 2 that aromatic primary amides bearing *para* substituents with long alkyl chains forms a highly symmetric pattern. Although the molecular symmetry of amide amphiphiles is C_s, the high symmetry pattern is in the plane group of *p*6 and contains rhombic voids. The symmetry barrier can be overcome by forming an aggregate. The aggregate of three molecules serves as a second building block simultaneously generating 3- and 6-fold rotation axes by hydrogen bonding. This result demonstrates that a high symmetry pattern is achievable without correlation with molecular symmetry through the proper combination of noncovalent interactions of simple amphiphilic molecules.

Upon the hypothesis that amphiphile molecules can give rise to various aggregation modes potentially leading to different organizations on the surface, 2D crystallization of an amide amphiphile containing a C_{18} alkyl-chain was conducted at the liquid/graphite interface (Chapter 3). This amide amphiphile showed the ability to exist in at least six different forms from various solvents and at different concentrations. Several of these phases display regularly arranged nanoscopic voids. Structural analysis of each phase reveals that highly symmetric and/or complex patterns arise through adopting various aggregates via non-covalent interactions, several of which are mediated by the unique hydrogen bonding properties of the primary amide. The formation of each phase is interpreted in the context of the kinetic and thermodynamic behaviors with some phases showing concentration dependent stabilities while others are purely kinetic in origin. This investigation contributes to understanding the factors that give rise to solid form diversity in 2D and 3D crystallization.

6.3 Two-dimensional crystallization of an amide amphiphile in the presence of an additive.

In the Chapter 2 and 3, it was demonstrated that an amide amphiphile has ability to exist in multiple phases. In Chapter 4, this pseudo-polymorphic amide amphiphile was used to understand the phenomenon recently observed in 3D crystallization that metastable polymorphs could be obtained during attempts to grow cocrystals with additives. The same phenomenon was observed in 2D crystallization from binary solutions while attempting to induce coadsorption. It has been revealed that the competition with an additive affects kinetics of 2D crystallization of **18-amide** and an additive can play a critical role in stabilizing a metastable form, resulting in inhibiting the phase transformation to a more stable phase. These observations provide mechanistic insights regarding pathways for the isolation of metastable forms.

During the competition study between the amide amphiphile and diheptadecyl phthalate in Chapter 4, a 2D cocrystal that displays random mixing along one axis and periodic ordering along the other axis was discovered. The characteristics and formation process of this "1D-cocrystal" were examined with atomic detail by STM at the liquid/solid interface and through computed models. This type of cocrystallization causes an alignment shift in order to satisfy close packing. The frequency of the alignment shift can be controlled by variation of the ratio of adsorbates in solution. Furthermore, a reversible monolayer reorganization induced through perturbing the STM bias voltage provides not only mechanistic insights into the formation process of the 1D-cocrystal but also the potential for applications as a molecular switch. The control over surface composition and periodicity by controlling the molar ratio of components offers an unexploited approach to nanoscale patterning.

6.4 Two-dimensional crystal engineering

As shown in Chapter 2, the hydrogen bonding network enabled by the amide groups contains a 6-fold rotation axis that plays a critical role in forming a monolayer with $p6$ symmetry. For comparison, an acid amphiphile does not form the rhombic network. Because this result showed the dependence of functional groups for generating the monolayer in the $p6$ symmetry, additional scrutiny of amphiphiles containing other functional groups is desirable to determine if they are able to generate high symmetry monolayers. Therefore, amphiphiles containing other functional groups (Figure 6.1) are needed to examine their two-dimensional crystal structures. A common theme in these targets is the potential for hydrogen bond donation and acceptance. Modeling of potential aggregation modes on graphite will be conducted to predict the energetic outcome of various arrangements and will be applied in a predictive fashion to narrow the number of molecules to be examined. Ultimately this approach may allow a general solution to

yielding highly symmetric, and potentially porous, monolayers from readily available molecules thus facilitating their study in the future.

The physisorbed molecular networks with void spaces are now termed as "2D porous networks".[1-4] They are analogues of mesoporous materials such as zeolites, and metal-organic frameworks (MOFs), which are holding potential for applications such as separation, catalysis and gas storage.[5,6] These 2D porous networks are also useful for host-guest chemistry in 2D crystallization. For example, trimesic acid forms the honeycomb network with hexagonal voids and these voids can be filled with hexagonal shaped coronene as a guest molecule.[7] Because **18-amide** can form 2D porous networks with hexagonal or rhombic voids and the void size is tunable by controlling alkyl chain length as shown in Chapter 2 and 3, the examination of host-guest chemistry for this system will be attractive using various guest molecules with different sizes and shapes (Figure 6.2).

It has been demonstrated in Chapter 4 that an additive can play a critical role in isolating metastable forms and can kinetically and thermodynamically influence 2D crystallization. To fully understand this phenomenon, further studies using various additives are required. The slight modification based on the present additive structures may provide insights into a general role of additives in this phenomenon (Figure 6.3). For example, the competition study with **18-amide** and **17-*m*-diester** failed to prove the kinetic effects by an additive due to a dilution effect. This effect can be minimized if an additive has similar free energy associated with a monolayer formation as **18-amide**. This can be achieved by the slight modification of **17-*m*-diester** through either increasing alkyl chain length or adding functional group as shown in Figure 6.3.

6.5 References

(1)   Tao, F.; Bernasek, S. L. *J. Am. Chem. Soc.* **2005**, *127*, 12750-12751.

(2)   Furukawa, S.; Uji-i, H.; Tahara, K.; Ichikawa, T.; Sonoda, M.; De Schryver, F. C.; Tobe, Y.; De Feyter, S. *J. Am. Chem. Soc.* **2006**, *128*, 3502-3503.

(3)   Mu, Z.; Shu, L.; Fuchs, H.; Mayor, M.; Chi, L. *J. Am. Chem. Soc.* **2008**, *130*, 10840-10841.

(4)   Zhou, H.; Dang, H.; Yi, J. H.; Nanci, A.; Rochefort, A.; Wuest, J. D. *J. Am. Chem. Soc.* **2007**, *129*, 13774-13775.

(5)   Maes, M., Alaerts, L., Vermoortele, F., Ameloot, R., Couck, S., Finsy, V., Denayer, J., and De Vos, D. *J. Am. Chem. Soc.* **2010**, 132, 2284-2292.

(6)   Chae, H. K., Siberio-Pérez, D. Y., Kim, J., Go, Y.-B., Eddaoudi, M., Matzger, A. J., O'Keeffe, M., Yaghi, O. M. *Nature* **2004**, *427*, 523– 527.

(7)   Griessl, S. J. H.; Lackinger, M.; Jamitzky, F.; Markert, T., Hietschold, M.; Heckl, W. M. *Langmuir* **2004**, *20,* 9403-9407.
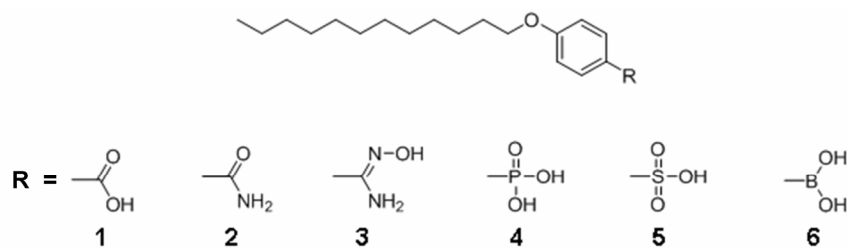
Figure 6.1. Functional groups potentially able to generate 6-fold rotation axes by hydrogen bonding.
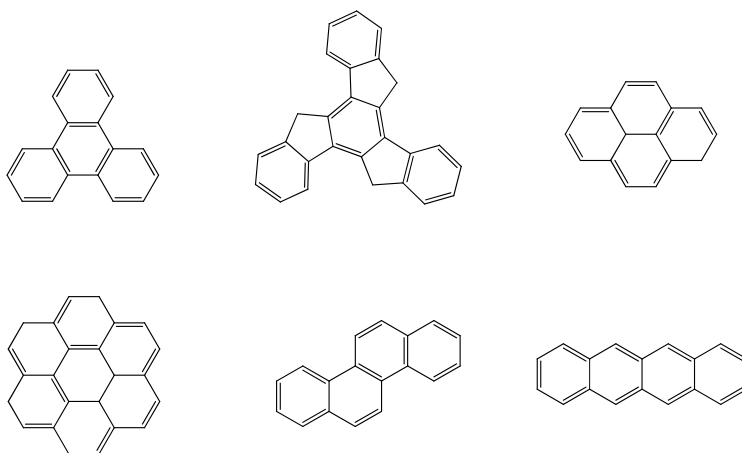
Figure 6.2. Structures of guest molecules to fit into various voids formed by amide amphiphiles.
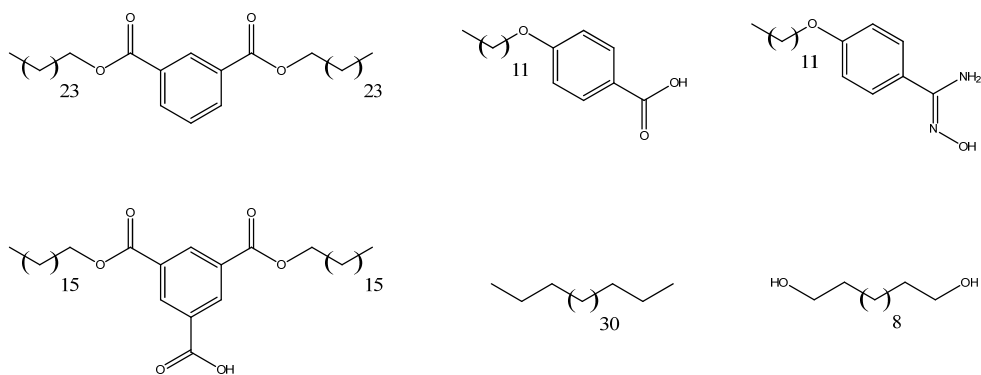
Figure 6.3. Additive structures to study 2D crystallization of **18-amide**.